SERCA-Phospholamban Structural Dynamics Studied by Electron Paramagnetic Resonance

A DISSERTATION
SUBMITTED TO THE FACULTY OF THE GRADUATE SCHOOL
OF THE UNIVERSITY OF MINNESOTA
BY

Zachary Matthew James

IN PARTIAL FULFILLMENT OF THE REQUIREMENTS
FOR THE DEGREE OF
DOCTOR OF PHILOSOPHY

David D. Thomas, Advisor

July, 2013

Acknowledgements

It's hard to thank everyone properly in a lab as large and integrated as DDT's, but I'll start with the obvious one. **Dave**, thank you for recruiting me to your lab and giving me (mostly) free reign over all the toys and EPR spectroscopist could hope for. Thank you for the guidance, the opportunities most grad students never have, and the many, many bottle of wine, though I can't say I learned as much about them as you would've liked.

Of course I have to thank **Jesse McCaffrey**, the perfect foil to my engrained cynicism, a good scientist and a great friend. If Veglia is right and we're like Laurel and Hardy, I guess that makes me the fat one.

To **Drs. Ji Li** and **Christine Karim**, fellow veterans of the Thomas Lab and good friends as well, thank you for the exciting collaborations and time spent discussing life outside of science. I feel lucky to work alongside you. Thanks to **Xiaoqiong Dong** for fighting alongside me in the battles of PLB expression, and to **Dr. Mike Autry** for inspiring conversations, and for lending your encyclopedic knowledge of biochemistry. Many thanks to lab managers **Sarah Blakely** and **Octavian Cornea** for your vital assistance over the years. Surely the lab would collapse without you.

To former lab members, **Drs. Elizabeth Lockamy** and **Kurt Torgersen**, thank you for befriending and training me in the early days when I was clueless, and to muscle people past and present, **Drs. Yun Lin, Becca Moen**, **and Ryan Mello,** thank you for the support and friendship. Special thanks to former DDT Lab member **Dr. Roman Agafonov**, a great drinking companion and brutal critic (in the best sense) of my work. Roman taught me that no lab is complete without at least one Russian.

Dedication

To my family, Betty, William, Cindy, and Amanda
To my extended family, Richard and Carolyn

And to Tiana.
For getting me this far

Abstract

Cardiac muscle function is regulated by calcium, with the sarcoplasmic reticulum (SR) serving as a Ca^{2+} reservoir that releases its contents into the cytoplasm to initiate contraction. Relaxation requires that Ca^{2+} be removed from the cytoplasm, which is accomplished primarily by the SR Ca^{2+}-ATPase (SERCA), a transmembrane pump protein that consumes ATP to transport Ca^{2+} to the SR interior, priming the muscle cell for another round of contraction. Cardiac SERCA is regulated by a second transmembrane SR protein, phospholamban (PLB), which binds and inhibits the ATPase unless phosphorylated at Ser16 by protein kinase A (PKA). The mechanism of SERCA inhibition by PLB, and the manner in which Ser16 phosphorylation reverses this inhibition remain poorly understood. The generally accepted model holds that Ca^{2+} and PLB binding to SERCA are mutually exclusive, and that phosphorylation dissociates PLB to restore SERCA's calcium sensitivity. However, a number of spectroscopic studies have called this dissociation model into question, and instead suggest an alternative mechanism where PLB behaves as a subunit of SERCA, and changes its interactions with the ATPase upon phosphorylation to relieve inhibition.

The work presented in this thesis tests several aspects of this alternative regulatory model, the Subunit Model, using spin-labeling and electron paramagnetic resonance (EPR) spectroscopy. In the first study, we used EPR to determine whether the inhibitory domain of PLB, its lone transmembrane helix, remains associated with SERCA following Ser16 phosphorylation. We found that the transmembrane helix of phosphorylated PLB remains bound to SERCA, in support of the Subunit Model, with our results hinting at a

subtle structural change induced by phosphorylation. In the second study, we investigated the role of PLB's dynamic cytoplasmic helix in SERCA regulation, which equilibrates between an ordered T state and a dynamically disordered R state. Using charged lipids, we perturbed the electrostatic interactions between PLB's positively-charged cytoplasmic helix and the lipid bilayer, and then used EPR to resolve the T and R populations. We found that perturbation of the T/R equilibrium by charged lipids directly correlated with the functional state of SERCA, indicating that T and R correspond to inhibitory and non-inhibitory PLB conformations within the SERCA-PLB complex. In our final and ongoing study, we returned to PLB's transmembrane domain and used EPR accessibility measurements to detect conformational changes of this helix induced by Ser16 phosphorylation. Our results suggest that phosphorylation induces a subtle change in the tilt and/or rotation of PLB's transmembrane helix relative to SERCA, which may break inhibitory interactions and restore SERCA Ca^{2+} sensitivity without dissociating the regulatory complex.

Table of Contents

List of Figures

List of Equations

List of Tables

Chapter 1 – Calcium Signaling in Muscle

1.1 The Role of Calcium in Excitation-Contraction Coupling

Muscle contraction is governed by excitation-contraction (EC) coupling; a Ca^{2+}-dependent process that transforms contractile signals into force generation. Cardiac EC coupling begins with an action potential generated by pacemaker cells, leading eventually to Ca^{2+} release from the sarcoplasmic reticulum (SR), a Ca^{2+} storage organelle surrounding the bundles of thick (myosin) and thin (actin) filaments ultimately responsible for generating force (Fig. 1) [1]. To prompt SR Ca^{2+} release, the action potential travels across the muscle cell membrane (the sarcolemma) and into deep invaginations (t-tubules) that bring the sarcolemma close to the SR membrane. L-type calcium channels localized to the t-tubules detect the action potential and permit a small Ca^{2+} influx into the cytoplasm. Nearby ryanodine receptor (RyR) proteins embedded in the SR membrane sense the small Ca^{2+} influx and open to release a flood of Ca^{2+} from the SR lumen. The released Ca^{2+} diffuses into the bundles of interlacing thick and thin filaments (the myofilaments), and binds the regulatory troponin/tropomyosin complex decorating actin (red lines, Fig. 1). Ca^{2+} binding triggers a conformational change that shifts the position of troponin/tropomyosin on the actin filaments (green lines, Fig. 1) to expose myosin binding sites. Myosin catalytic domains can then interact with actin, forming 'cross-bridges' between the thick and thin filaments. Cycles of cross-bridge formation and dissociation, coupled with myosin conformational changes fueled by adenosine triphosphate (ATP) hydrolysis, further interlace the thick and thin filaments by sliding them relative to one another, shortening the myofibril to produce contraction.
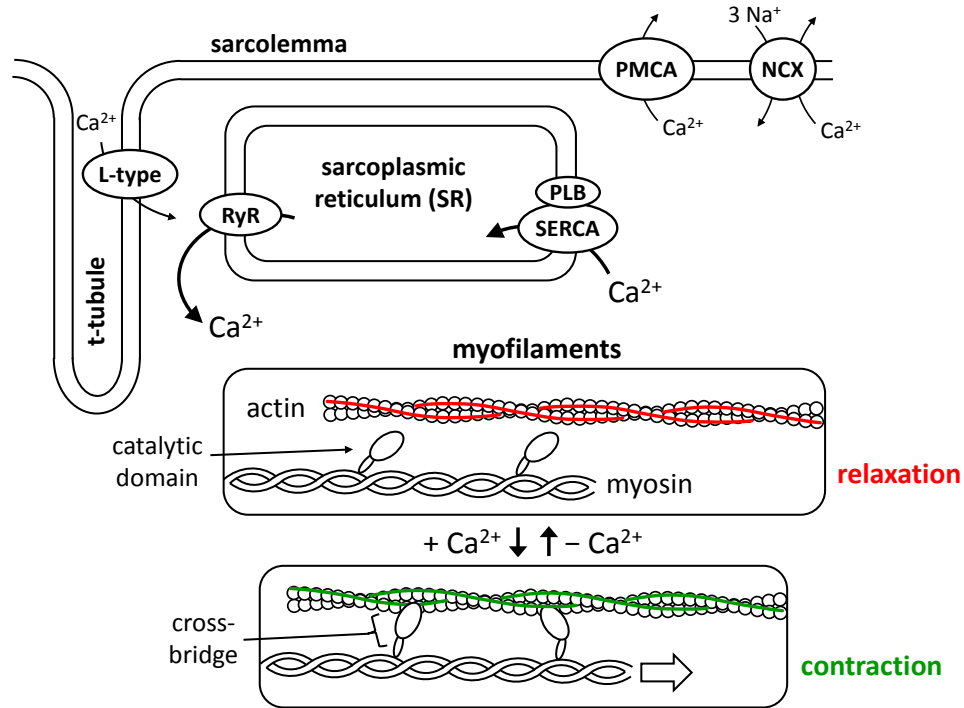
Fig. 1. Calcium flux in cardiac excitation-contration coupling. Ca^{2+} influx through L-type channels activates RyR channels embedded in SR membrane to release luminal Ca^{2+}. Regulatory proteins decorating actin (red lines) bind Ca^{2+} and change their conformation (green lines) to permit cross-bridge formation. Ca^{2+} removal from the cytoplasm induces relaxation, and is accomplished largely by the SR Ca^{2+}-ATPase (SERCA), followed by the Na^+/Ca^{2+} exchanger (NCX) and sarcolemmal Ca^{2+}-ATPase (PMCA). SERCA function is regulated by phospholamban (PLB).

Muscle relaxation requires that Ca^{2+} be removed from the cytoplasm. Ca^{2+} clearance is accomplished primarily by the SR Ca^{2+}-ATPase (SERCA), a pump protein embedded in the SR membrane that restores Ca^{2+} to the SR lumen by hydrolyzing ATP. Other proteins assist in Ca^{2+} removal, including sarcolemmal Na^+/Ca^{2+} exchangers (NCX) and Ca^{2+}-ATPases (PMCA) that both expel calcium from the cell, though SERCA accounts for at least 70% of Ca^{2+} clearance in the heart [2]. Cardiac SERCA is found alongside phospholamban (PLB) [3, 4], a small but crucial transmembrane protein that binds and reversibly inhibits the ATPase. Inhibition manifests as an increase in K_{Ca}: the calcium concentration where SERCA activity is half-maximal. Phosphorylation of PLB reverses SERCA inhibition (i.e., restores Ca^{2+} affinity) and also couples SERCA function

2

to the β-adrenergic pathway. PLB contains phosphorylatable residues serine 16 (Ser16) and threonine 17 (Thr17), targeted by protein kinase A (PKA) and calmodulin/Ca^{2+}-dependent protein kinase II (CaMKII), respectively [5]. β-adrenergic stimulation activates both kinases, resulting in phosphorylation at one or both sites. The consequent increase in cardiac SERCA function permits a more forceful contraction-relaxation cycle in accordance with the inotropic effects of β-agonists like adrenaline.

1.2   The SR Ca^{2+}-ATPase

SERCA is a member of the ubiquitous P-type ATPase family, named for the auto-phosphorylated intermediate found in the enzymatic cycles of all member proteins. Most P-type ATPases transport metal ions, including the Na^{+}/K^{+}-ATPase, H^{+}/K^{+}-ATPase, and various heavy-metal (e.g., Cd^{2+}, Cu^{+}) transporters, though several function as lipid flippases that help maintain the asymmetry of bilayer leaflets [6]. SERCA in particular has been the focus of many functional and structural studies due to its role in excitation-contraction coupling. SERCA is the product of three genes (ATP2A1, ATP2A2, and ATP2A3) expressed differently throughout the body, with each gene subject to alternative splicing that further differentiates expression according to tissue type or stage of organism development (i.e., fetal versus adult isoforms) [7]. The best characterized isoform is SERCA1a, expressed from ATP2A1, which is abundant in adult fast-twitch skeletal SR and can be obtained in large quantities at relatively high purity. The predominant cardiac isoform is SERCA2a (expressed from ATP2A2), which shares 84% sequence identity with SERCA1a and behaves similarly with respect to specific activity

3

and Ca^{2+} affinity [7]. Based on these similarities, and given the ease of SERCA1a purification from skeletal muscle, SERCA1a is often substituted for SERCA2a for *in vitro* studies of SERCA-PLB regulation. This substitution is conservative, with regulation of SERCA1a by PLB being comparable to that of SERCA2a [8], though PLB shows moderately higher affinity for the 1a isoform [9]. The interchangeability of 1a and 2a isoforms was also demonstrated *in vivo* using transgenic mouse models expressing SERCA1a alongside SERCA2a in the heart [10, 11], which revealed similar kinetic properties and PLB regulation for the co-expressed isoforms relative to those of SERCA2a alone.

SERCA1a consists of a single polypeptide chain (~1000 residues) folded into a
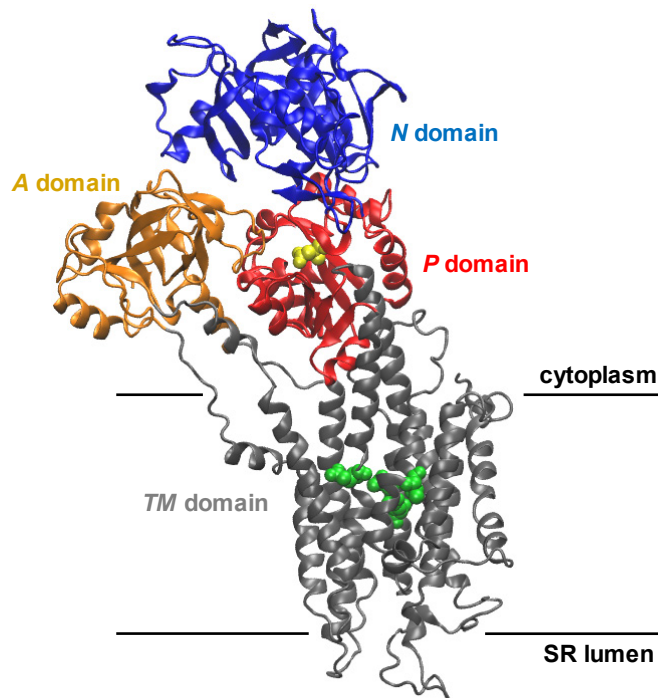
Fig. 2. E2 SERCA structure. The cytoplasmic actuator (*A*, orange), nucleotide-binding (*N*, blue), and phosphorylation (*P*, red) domains form SERCA's headpiece, with the autophosphorylation site (Asp351, space-filling yellow) found in the *P* domain. Ca^{2+} binding occurs at two sites (space-filling green) in the *TM* domain (grey). Structure determined by Toyoshima et al. [12] (PDB code 1IWO) and modeled using VMD [13].

Ca^{2+}-binding transmembrane (*TM*) domain and a cytosolic 'headpiece' containing the phosphorylation (*P*), nucleotide-binding (*N*), and actuator (*A*) domains (Fig. 2) [14]. Each domain serves a specific purpose in the context of the E1/E2 model, which describes SERCA function in terms of high-Ca^{2+}-affinity (E1) and low-Ca^{2+}-affinity (E2) enzymatic states (Fig. 3) [15]. Beginning in the Ca^{2+}-free E2 state, SERCA exchanges bound protons for two cytoplasmic Ca^{2+} ions (gated by the *A* domain) and transitions to E1. ATP binding in the *N* domain ($Ca_2E1 \cdot ATP$), followed by rearrangement of the headpiece, brings the ATP γ-phosphate into position for attack by a highly-conserved aspartate residue in the *P* domain (Asp351 in SERCA1a). Simultaneously, the *TM* domain closes cytoplasmic access to the Ca^{2+} binding sites. The resulting Ca^{2+}-loaded phosphoenzyme (Ca_2E1P) releases adenosine diphosphate (ADP) and transitions to the low-affinity Ca_2E2P intermediate. In this state, the binding sites become exposed to the SR lumen and bound Ca^{2+} ions are swapped for protons. Finally, dephosphorylation of Ca^{2+}-unloaded E2P (catalyzed by a conserved motif in the *A* domain) and the release of inorganic phosphate (P_i) returns SERCA to E2 and poises it for another enzymatic cycle.
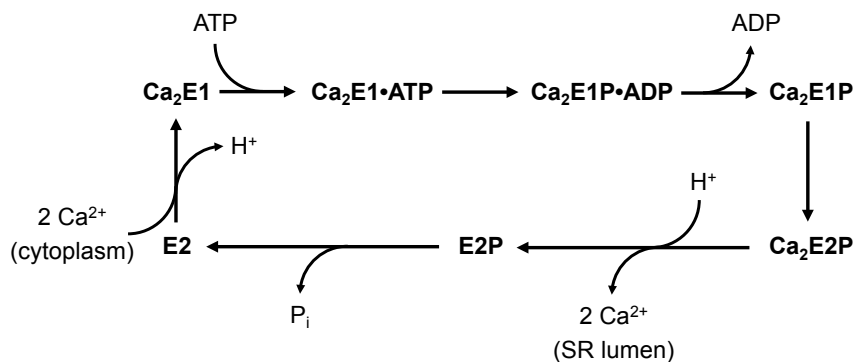
Fig. 3. SERCA enzymatic cycle. To pump calcium, SERCA alternates between high-affinity (E1) and low-affinity (E2) enzymatic states, passing through auto-phosphorylated intermediates (E1P and E2P) produced by the hydrolysis of ATP.

A number SERCA1a structures have been resolved by X-ray crystallography and assigned as different intermediates in the enzymatic cycle (thoroughly reviewed by Møller et al., [15]) . The first high-resolution structure was obtained with Ca^{2+} in the *TM* binding sites (Ca_2E1) [16], while subsequent structures trapped SERCA in the absence of Ca^{2+} (E2) [12] or complexed with Ca^{2+} and various nucleotide analogs. Together the crystal structures indicate that during E2-E1 transition, there is significant repositioning of several transmembrane helices, along with a controversial change [17] in the relative positions and orientations of the *N* and *A* domains. In particular, the more outspread positions of transmembrane helices M2, M4, M6 and M9 in the E2 state (Fig. 4) has relevance for the SERCA-PLB complex, as will be described in section 1.4.
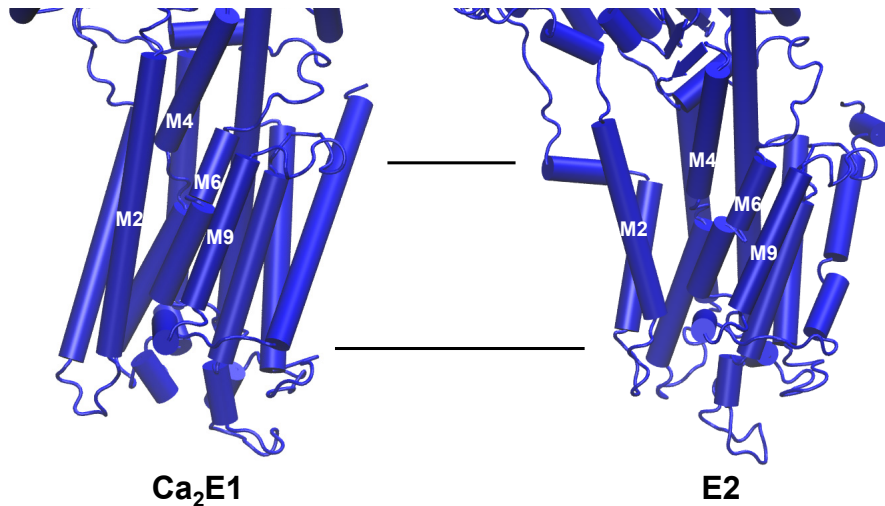
Fig. 4. Rearrangement of TM Helices between E1 and E2 SERCA. Crystal structures of Ca^{2+}-bound (E1) and Ca^{2+}-free (E2) SERCA indicate a repositioning of several transmembrane helices. Structures originally reported in [16] (PDB code 1SU4) and [12] (PDB code 1IWO).

1.3   Phospholamban

In comparison to SERCA, phospholamban is a significantly smaller protein containing only 52 residues divided into three structural domains (Fig. 5). A dynamic cytoplasmic

helix comprises residues 1 – 16 (domain Ia), and is connected to a single transmembrane helix (residues 23 – 52) by a short, flexible loop (residues 17 – 22). The transmembrane helix further divides into a more flexible N-terminal region (domain Ib, residues 23 – 30) and a highly-stable C-terminal region (domain II, residues 31 – 52) [18] that resists unfolding by most denaturants.
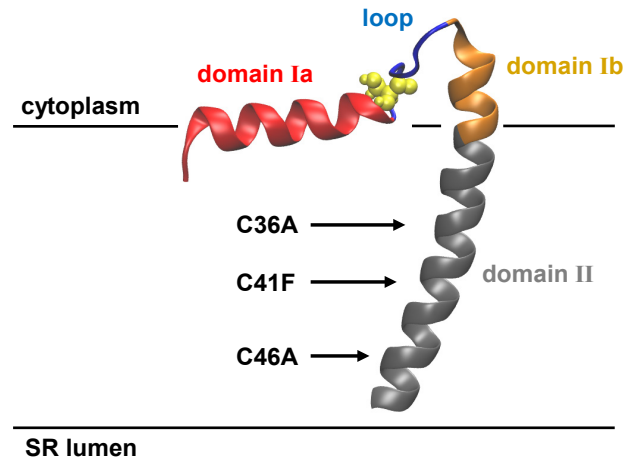
Fig. 5. Structure of monomeric PLB in the *T* state. PLB inserts into the SR membrane with a single transmembrane helix composed of domains Ib (orange) and II (grey). The TM helix connects via a short loop (blue) to an amphipathic, cytoplasmic helix (domain Ia, red) containing the phosphorylation site (Ser16, space-filling yellow). Indicated mutations C36A, C41F, and C46A disrupt pentamerization and render PLB entirely monomeric. Structure resolved by Traaseth et al. [19] using a combination of solution and solid-state NMR restraints (PDB code 2KB7).

Early gel electrophoresis studies revealed that wildtype PLB equilibrates between monomers (~20%) and homopentamers (~80%) [20], with the latter stabilized by an extensive leucine/isoleucine zipper accounting for ~30% of domain II [21, 22]. The pentamer is quite stable, dissociating only at high temperatures (> 45 °C) in the presence of sodium dodecyl sulfate (SDS) [23], though mutations to the zipper destabilize the pentamer [22, 24], as do bulky mutations (e.g., C41F) at the interfaces of the protomers. Mutagenesis studies also found a strong correlation between pentamer-destabilizing mutations and PLB inhibitory potency, indicating that the monomer regulates SERCA

function [25]. Currently the pentamer is believed to act as a reservoir that buffers PLB availability, though cryo-electron microscopy studies by the Young group [26] suggest that it may interact directly with SERCA in a manner distinct from the monomer. To simplify *in vitro* studies of SERCA-PLB regulation, the Cys-null PLB variant C36A/C41F/C46A (AFA-PLB) is often used to render the protein entirely monomeric [27]. These mutations disrupt pentamerization without compromising PLB inhibitory potency, and facilitate site-directed labeling (which usually targets engineered Cys residues) by removing the endogenous cysteines [28].

Spectroscopic studies of AFA-PLB revealed that domains Ia and Ib both transition between several dynamic conformations, including a structured, rigid *T* state and an extended, flexible *R* state (Fig. 6) [28-30]. In the *T* state, domain Ia forms an amphipathic helix that buries its hydrophobic face (including residues V4, L7, I12, and I18) into the acyl region of the lipid bilayer, while domain Ib forms an extension of the stable domain II helix [19]. The *R* state is considerably more dynamic, with both domains Ia and Ib undergoing ps − ns motions, as observed by EPR using synthetic PLB constructs containing the TOAC spin label at positions 11 (Ia) or 24 (Ib) [29].
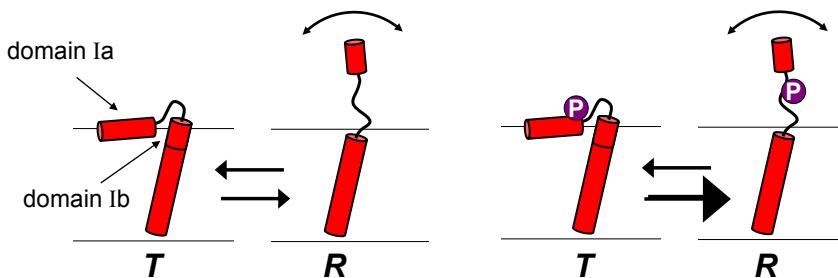
Fig. 6. Model of PLB's *T* and *R* states. EPR and NMR spectroscopies detect a dynamic equilibrium of PLB's cytoplasmic domains (Ia and Ib) between an ordered, membrane-absorbed *T* state and a dynamically disordered, membrane-dissociated *R* state. PLB phosphorylation at Ser16 (purple circle) favors the *R* state and induces a *T*-to-*R* (order-to-disorder) transition.

Furthermore, NMR accessibility measurements [31] found that in the **R** state, hydrophobic residues V4, L7, and I12 are significantly more exposed to the aqueous phase, indicating that domain Ia can dissociate from the bilayer surface. Another NMR study [30] detected additional substates where domain Ia is unfolded but remains bound the membrane (**R′**), or is membrane-dissociated but still structured (**T′**), underscoring the complex nature of PLB structural dynamics.

An important finding from both EPR and NMR experiments is that the **T**/**R** equilibrium depends on PLB's phosphorylation state, with Ser16 phosphorylation inducing a **T**-to-**R** (order-to-disorder) transition as it restores SERCA Ca^{2+} sensitivity (Fig. 6, right). Elimination of the **R** state by attachment of an N-terminal lipid anchor was found to uncouple Ser16 phosphorylation from inhibition relief [32], while mutations destabilizing the **T** state (e.g., P21G and phosphomimetic S16E) reduced SERCA inhibition [33], pointing to a relationship between the **T**/**R** equilibrium and PLB's inhibitory potency.

1.4 SERCA-PLB Interactions and Regulatory Models

To date, no high-resolution structures of SERCA-PLB have been determined, though the collective results from numerous mutagenesis, immunoprecipitation, and crosslinking experiments have yielded a working model of the regulatory complex (Fig. 7) [34]. In this model, PLB associates with E2 (low-Ca^{2+}-affinity) SERCA through multiple interactions, including those between domain Ia and residues $397 - 401$ in the *N* domain, between domain Ib and *TM* helix M4, and finally between domain II and a shallow

groove formed by *TM* helixes M2, M4, M6, and M9. Simultaneous interaction with the *N* and *TM* domains requires that PLB adopt an extended conformation where domain Ib is unfolded, in qualitative agreement with its dynamic nature as observed by NMR and EPR. Notably, the crosslinking and immunoprecipitation results used to build this model found a disruption of SERCA-PLB interactions at elevated Ca^{2+}. In addition, the putative *TM* binding groove in the E2 SERCA structure is absent in the E1 (Ca^{2+}-bound) structure (Fig. 4), suggesting that Ca^{2+} and PLB binding are mutually exclusive. More recent crosslinking studies varying both $[Ca^{2+}]$ and PLB's phosphorylation state [35] suggest that Ser16-phosphorylated PLB has lower affinity for SERCA, supporting a model (the Dissociation Model, Fig. 8, left) where PLB traps SERCA in the E2 conformation that requires dissociation (induced by phosphorylation) for SERCA to bind Ca^{2+} and proceed through the enzymatic cycle.
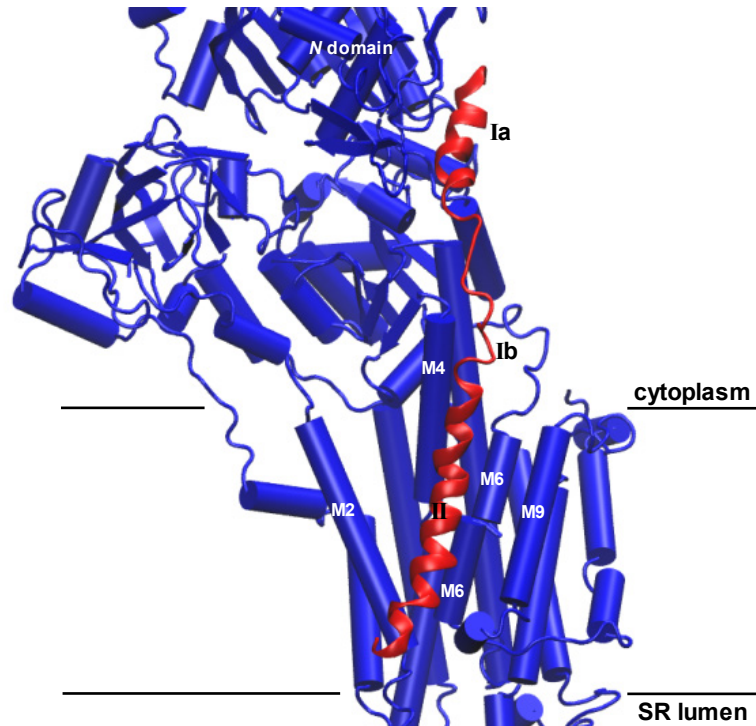
Fig. 7. Model of the SERCA-PLB regulatory complex. Based on crosslinking, mutagenesis, and immunoprecipitation studies, PLB (red) associates with SERCA (blue) through all three domains (Ia, Ib, and II) and adopts an extended conformation. In this model, SERCA must be in the E2 (Ca^{2+}-free) state to accommodate PLB domain II in a groove formed by M2, M4, M6, and M9. Model published by Toyoshima et al. [34].

Recent spectroscopic studies have contradicted the Dissociation Model of SERCA-PLB regulation. Fluorescence resonance energy transfer (FRET) measurements between reconstituted SERCA and PLB, each labeled with a fluorescent probe, found that elevated Ca^{2+} does not significantly alter the measured inter-probe distance, indicating the PLB can remain bound to SERCA throughout its enzymatic cycle [36]. Other fluorescence measurements by the Squier/Bigelow group found a similar retention of SERCA-PLB interactions with Ser16 phosphorylation [37], while suggesting that phosphorylation relieves inhibition by changing PLB's conformation within the regulatory complex [38], and possibly altering the interactions between oligomerized SERCA protomers [39]. These findings spurred development of the Subunit Model of

SERCA-PLB regulation (Fig. 8, right), where PLB remains bound to SERCA throughout its catalytic cycle, but adopts distinct inhibitory and non-inhibitory conformations whose equilibrium is shifted toward the latter following Ser16 phosphorylation. These conformations may correspond to the *T* and *R* states observed for PLB, with Ser16 phosphorylation inducing a *T*-to-*R,* and thus inhibitory-to-non-inhibitory, transition. Such a model would explain the observations mentioned in section 1.3, where perturbation of the *T*/*R* equilibrium via mutations, or attachment of lipid anchor to domain Ia, affects PLB's inhibitory potency.
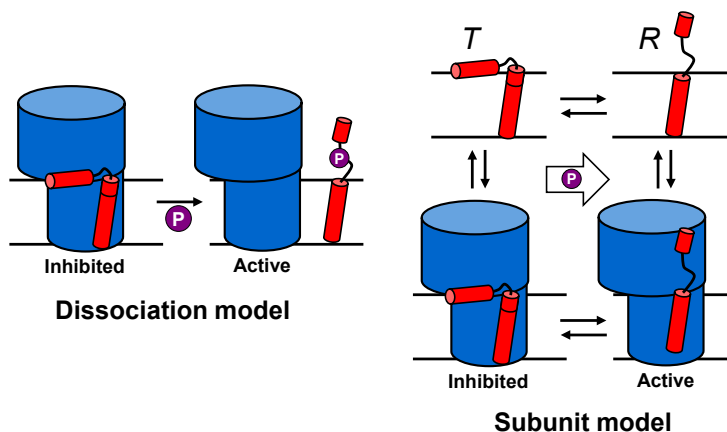
Fig. 8. Competing models of SERCA-PLB regulation. Crosslinking studies support a Dissocation Model, where Ser16 phosphorylation (purple circle) induces PLB (red) to dissociate from SERCA (blue). Spectroscopic measurements support an alternative Subunit Model, where PLB remains bound to SERCA, but transitions from an inhibitory *T* state to a non-inhibitory *R* state upon phosphorylation.

Validating and investigating the Subunit Model. A notable omission from previous spectroscopic studies supporting the Subunit Model is the absence of measurements from domain II, PLB's transmembrane helix, which is known to mediate SERCA inhibition [8]. In Chapter 3, we used EPR to demonstrate that domain II also remains bound to SERCA following phosphorylation. In Chapter 4, we used EPR in combination with time-resolved fluorescence resonance energy transfer (TR-FRET) to show that PLB's *T*

and R states, when perturbed by electrostatic interactions between domain Ia and the lipid bilayer, correlate directly with the degree of SERCA inhibition. Finally, Chapter 5 describes an ongoing project using accessibility EPR to elucidate conformational changes in domain II induced by Ser16 phosphorylation, which may break its inhibitory interactions with SERCA to mediate inhibition relief.

Chapter 2 – Spin Labeling and Electron Paramagnetic Resonance

2.1   Site-directed spin labeling

Electron paramagnetic resonance (EPR) spectroscopy is a powerful method for studying the structure, dynamics, and local environment of proteins. EPR exploits the interaction of electromagnetic radiation with unpaired electrons, and with few exceptions, biological systems lack the stable radicals necessary for EPR measurements. However, they can be readily introduced using nitroxide spin labels [40]. These probes consist of heterocyclic rings containing a nitroxide group that harbors an unpaired electron. Methyl groups flank and stabilize the nitroxide, while reactive maleimide, iodoacetamide, or methanethiosulfonate groups permit attachment to the protein by targeting the labile thiols of cysteine residues (Fig. 9). Early protein EPR studies relied on the fortuitous labeling of endogenous cysteines, or occasionally the non-covalent binding of labels to
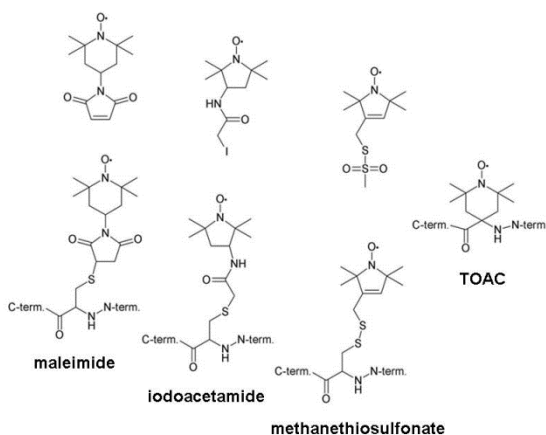
Fig. 9. Common nitroxide spin labels. Nitroxides harbor an unpaired electron and are stabilized by methyl groups surrounding the N–O bond. Maleimide, iodoacetamide, and methanethiosulfonate reactive groups mediate nitroxide attachment to endogenous and engineered cysteines, while the rigid TOAC spin label can installed into small proteins by solid-phase peptide synthesis.

proteins, limiting the utility of the technique. However, the combination of spin labeling with recombinant protein expression and site-directed mutagenesis, pioneered by the Hubbell lab [41], greatly expanded the role of EPR in protein structural dynamics studies.

More recently, solid-phase peptide synthesis has become a popular method for spin labeling smaller proteins of up to 50 residues. Peptide synthesis permits the incorporation of TOAC (2,2,6,6-tetramethylpiperidine-1-oxyl-4-amino-4-carboxylic acid), a spin-labeled amino acid with the nitroxide group and α-carbon incorporated into the same six-membered ring [42] (Fig. 9, right). TOAC offers an elegant solution to the inherent flexibility of conventional spin labels, arising from their many rotatable bonds connecting the nitroxide to the cysteine α-carbon (compare, for example, the TOAC and iodoacetamide spin labels in Fig. 9). Spin label flexibility can mask the dynamics of the peptide backbone, often the desired result of conventional EPR measurements, by adding fast (ps − ns) probe motions atop the backbone motions. By rigidly coupling the EPR-active center (the nitroxide) to the α-carbon, TOAC allows one to faithfully measure backbone dynamics [29].

2.2   Electron Spin and the Zeeman Effect

The fundamental basis for EPR spectroscopy is *spin* angular momentum; an intrinsic property of electrons (and some nuclei) responsible for generating a magnetic moment that interacts with magnetic fields [43]. Spin is a quantum mechanical parameter that adopts discrete values, meaning the particle's magnetic moment (μ) is also quantized. The number of possible values (i.e., spin states) is determined by the spin quantum

number s, which allows for $2s + 1$ states (denoted by m_s) ranging from $-s$ to $+s$ in steps of one. Electrons are $s = \frac{1}{2}$ particles with two available spin states, $m_s = -\frac{1}{2}$ and $+\frac{1}{2}$.

An important consequence of spin quantization is that both the magnitude *and direction* of μ are quantized. In isolation μ has no preferred orientation, but the application of a magnetic field (H_0) compels it to align parallel to H_0, similar to the alignment of a bar magnet in an applied field. Quantization, however, restricts μ to specific orientations (relatives to H_0) corresponding to the available spin states. The magnetic moment is prevented from aligning precisely with H_0 due to the Uncertainty Principle, which limits the determination of μ to its magnitude ($|\mu|$) and only one of its vector components; μ_x, μ_y, or μ_z (where precise alignment between μ and H_0 would lift the uncertainty of all vector components). It is customary to assign H_0 as the z-axis and to designate μ_z as the determinable component, which can be calculated using Eq. 1:

$$\mu_z = g\beta m_s \qquad \text{Eq. 1}$$

where β is the Bohr magneton ($9.274 \cdot 10^{-24}$ J $\cdot$ T^{-1}) and g is a unitless scaling factor (~ 2) accounting for local field effects and deviation of the electron from classical behavior. The energy associated with each orientation of μ is given by Eq. 2:

$$E_s = \mu_z H_0 = g\beta m_s H_0 \qquad \text{Eq. 2}$$

For electrons, the spin state energies are $-\frac{1}{2}g\beta H_0$ and $+\frac{1}{2}g\beta H_0$, corresponding to μ_z aligned parallel ($m_s = -\frac{1}{2}$) or antiparallel ($m_s = +\frac{1}{2}$) with the magnetic field (note that for electrons, μ is antiparallel to the spin vector). Clearly the spin states are separated by the magnetic field, with the extent of splitting ($\Delta E_s = E_{s(+\frac{1}{2})} - E_{s(-\frac{1}{2})} = g\beta H_0$) proportional to

the field strength. This lifting of spin-state degeneracy in the presence of a magnetic field

is known as the *Zeeman Effect* (Fig. 10a).
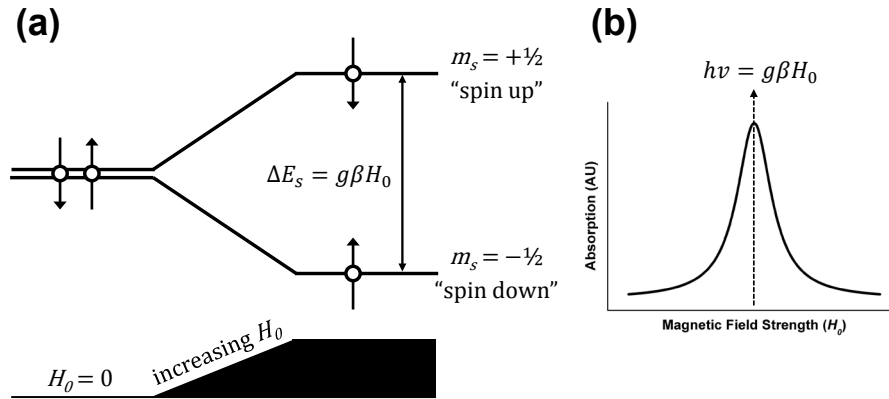
Fig. 10. The Zeeman Effect. (a) Electron spin states are degenerate in the absence of an external magnetic field (H_0 = 0), but separate in the presence of a magnetic field, with z-component of the electron magnetic moment (μ_z) aligning parallel or antiparallel with the field (H_0). (b) Absorption occurs when the resonance condition is satisfied, which in conventional EPR is accomplished by varying the magnetic field strength (see section 2.4).

In a magnetic field, the energy difference between the two spin states leads

electrons to slightly favor the parallel orientation ($m_s = -\frac{1}{2}$) over the antiparallel one (m_s

$= +\frac{1}{2}$), with the population ratio obeying a Boltzmann distribution. The parallel

orientation serves as a ground state that can be excited to the antiparallel orientation (a

'spin-flip') by absorbing a photon of appropriate energy. A photon's energy is the

product of its frequency (v) and Plank's constant (h), and absorption occurs when the

following equivalency is satisfied (Eq. 3):

$$\Delta E_S = hv = g\beta H_0 \qquad\qquad \text{Eq. 3}$$

Eq. 3 specifies the *resonance condition*, where photons are absorbed only when their

energy matches the spin state separation established by the magnetic field. Eq. 3 implies

that a collection of identical electron spins (a 'spin packet') will all possess the same

resonance condition, but the splitting between the two spin states (ΔE_s) is also subject to

the Uncertainty Principle. This results in a distribution of resonance conditions,

17

manifesting in the EPR spectrum as a Lorentzian lineshape (Fig. 10b) with a width inversely proportional to the rate of spin relaxation (i.e., proportional to the excited spin lifetime). Spin relaxation is generally divided into two processes: spin-lattice (T_1) and spin-spin (T_2) relaxation. T_1 includes 'true' relaxation processes that result in the donation of spin energy to the system (i.e., the spin-lattice), returning excited spins to the ground state and restoring the equilibrium Boltzmann distribution. In contrast, T_2 are 'effective' relaxation processes that redistribute energy between spins without restoring the Boltzmann equilibrium. Regardless, T_2 processes decrease the lifetime of a given excited spin and thus contribute significantly to the linewidth. In conventional EPR measurements of spin-labeled proteins, T_2 processes outpace T_1 by several orders of magnitude, meaning the Lorentzian broadening (Fig. 10b) of these EPR spectra is often dominated by T_2 effects.

2.3   Hyperfine Interactions

Like electrons, nuclei can also possess an intrinsic spin angular momentum with an associated magnetic moment that adopts discrete orientations relative to a magnetic field. The predominant ^{14}N isotope carries a nuclear spin (I) of 1 and thus can assume three spin states, $m_I = -1$, 0, or +1, each with a distinct orientation of μ_z relative to the applied magnetic field. Nitroxides harbor their unpaired electron in a 2p orbital shared across an N–O bond, and thus the nitrogen spin magnetic moment contributes to the effective magnetic field experienced by the electron. This *hyperfine* interaction further divides the electron's energy levels, resulting in three transitions depending on the

18

orientation (m_I) of the nitrogen magnetic moment (Fig. 11a). The separation between these transitions is called the hyperfine splitting, and is denoted by T (Fig. 11b). With hyperfine interactions, electron transitions between the ground and excited states are governed by selection rules requiring that only the electron spin changes during a transition (i.e., $\Delta m_s = \pm 1$, $\Delta m_I = 0$), and thus only three transitions are observed in the typical nitroxide EPR spectrum (Fig. 11b).
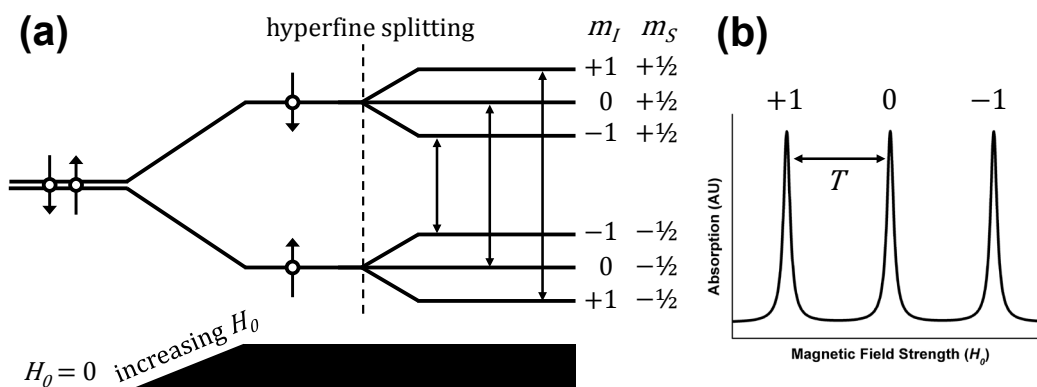
Fig. 11. Hyperfine splitting of the nitroxide EPR spectrum. (a) Interaction between the magnetic moments of the electron and the nitroxide's nitrogen nucleus further divides the electron's spin-state energy levels, giving rise to three transitions. (b) Three peaks are observed in the nitroxide EPR spectrum, separated by splitting T, corresponding to the available spin states of the nitrogen nucleus (m_I).

2.4   The EPR Spectrometer

Conventional EPR spectra are acquired in continuous wave (CW) mode, with the incident microwave frequency (usually ~9.5 GHz) held constant and the magnetic field strength gradually increased (swept) to achieve resonance [44]. In a typical CW EPR spectrometer (Fig. 12), microwaves are generated by a Gunn diode and directed into a cavity situated between the poles of an electromagnet. The cavity houses the sample, and is designed to resonate with incoming microwaves to produce a standing wave that amplifies the microwave intensity experienced by the sample. Sweeping the magnetic field brings

19

electron spins into resonance and results in microwave absorption, which alters the resonant properties of the cavity and causes microwave reflection (proportional to the extent of absorption) from the cavity to a detector diode, yielding the absorption signal.
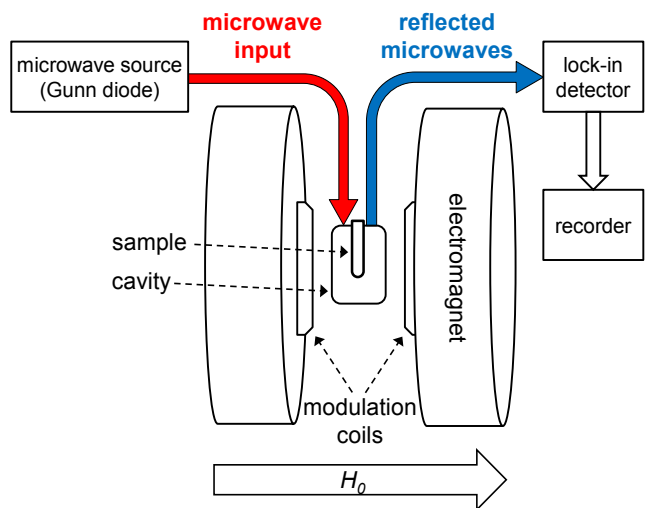
Fig. 12. Simplified schematic of a CW EPR spectrometer. Microwaves from a Gunn diode enter and resonate inside the cavity, which contains the sample. The electromagnet sweeps the magnetic field H_0 to achieve resonance (Eq. 3), resulting in microwave reflection, while the modulation coils supply the field modulation used for lock-in detection.

To improve the signal-to-noise ratio of the EPR spectrum, field modulation and lock-in detection are used to encode the raw absorption signal and separate it from random microwave noise (Fig. 13a). First, a sinusoidal field modulation with high frequency (ω_m, ~100 kHz) and small amplitude (H_m, ~1 G) is superimposed on the slow (~1 min) linear field sweep. When the field reaches, for example, a rising portion of the absorption spectrum, field modulation rapidly passes the resonance condition between positions slightly above and below the current field strength, where absorbance is slightly higher and lower, respectively. This results in modulation of the reflected microwave intensity at the same frequency and phase as the field modulation, with a magnitude M proportional to the slope of the absorption spectrum at the current field strength (i.e., the instantaneous slope). The intensity-modulated signal is then isolated from noise using a

20

lock-in detector set to the same frequency and phase as the field modulation, with the resultant output being equivalent to M. The proportionality between detector output M and the instantaneous slope means the field-modulated absorption spectrum (i.e., the conventional EPR spectrum) is essentially recorded as its first derivative, denoted by V_1. (Fig. 13b).
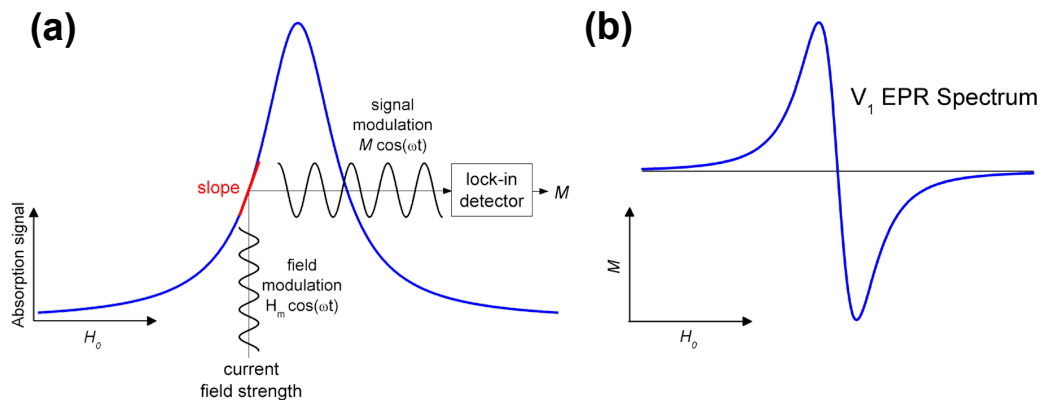
Fig. 13. The Field-Modulated EPR Spectrum. (a) Rapid modulation [$H_m\cos(\omega t)$] about the current field strength yields a modulated absorption signal [$M\cos(\omega t)$] with magnitude M proportional to the slope (red) of the absorption spectrum. A lock-in detector decodes the modulated signal to give an output equivalent to M. (b) The proportionality between output M and the instantaneous slope means the field-modulated EPR spectrum is recorded as the first derivative of the absorption spectrum.

2.5   Anisotropy and Motional Averaging in Conventional EPR

As mentioned in section 2.2, the resonance condition ($hv = g\beta H_0$) depends on a unitless scaling factor – the g factor – that accounts for local field effects and the electron's deviation from classical behavior. For nitroxides (and most molecules harboring unpaired electrons), the g factor is *anisotropic* and depends on the orientation of the molecule relative to the magnetic field. Furthermore, the asymmetry of the 2p orbital housing the unpaired electron, shared across the N–O bond, leads to anisotropy of the hyperfine interaction. Thus both the center position of the nitroxide EPR spectrum (dependent on g)

and the hyperfine splitting (*T*) are orientation-dependent. To account for anisotropy, the values of *g* and *T* can be expressed in terms of angles θ and Φ relating H_0 to the nitroxide principal axes (Fig. 14a, Eq. 4), with a corresponding *g* and *T* component for each Cartesian axis:

$$g(\theta,\phi) = g_x sin^2\theta cos^2\phi + g_y sin^2\theta sin^2\phi + g_z cos^2\theta$$

$$T(\theta,\phi) = (T_x{}^2 sin^2\theta cos^2\phi + T_y{}^2 sin^2\theta sin^2\phi + T_z{}^2 cos^2\theta)^{1/2}$$

Eq. 4

Fig. 14b shows the dependence of the nitroxide EPR spectrum on *g* and *T* anisotropy, with the most dramatic effects occurring when H_0 is aligned along the z axis of the probe (parallel to the 2p orbital of the nitroxide). In practice, however, the ensemble of nitroxides in a spin-labeled sample are usually oriented randomly relative to one another and the magnetic field, leading (in the absence of fast rotational motion) to a 'powder' EPR spectrum representing a superposition of all spin label orientations (Fig. 14c).
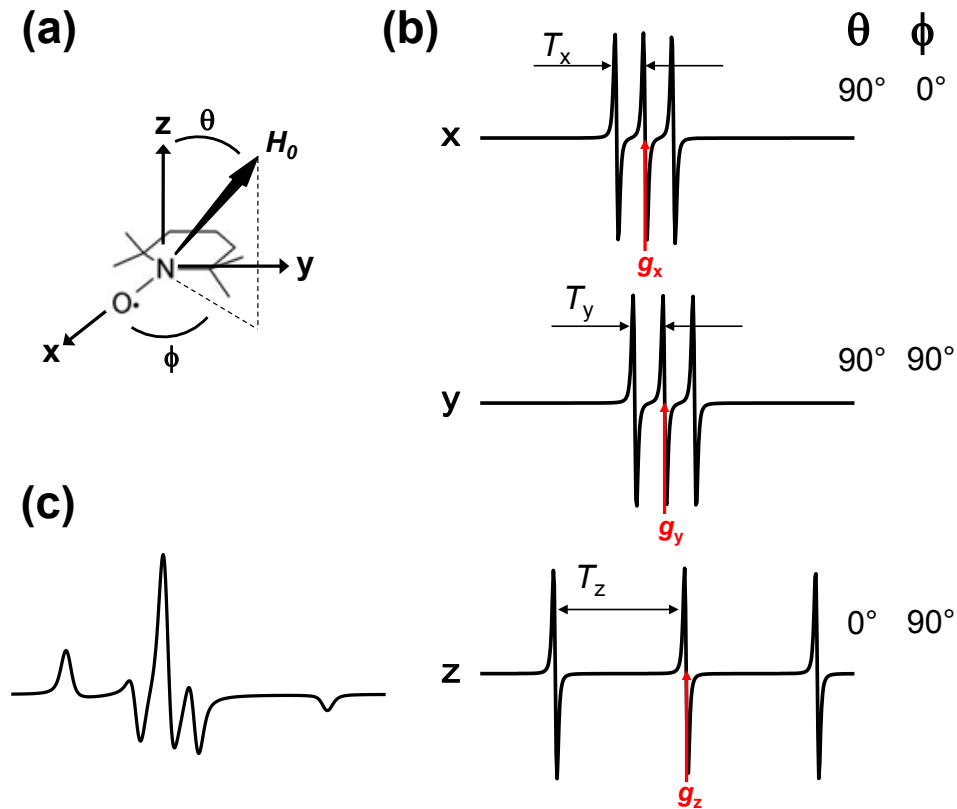
Fig. 14. Orientation dependence of the nitroxide conventional (V₁) EPR spectrum. (a) Coordinate system relating the nitroxide principle axes to the magnetic field vector (H_0). (b) Simulated EPR spectra with H_0 aligned along each of the nitroxide principle axes, with changes to hyperfine splitting (T) and spectral center (g, red) indicated. (c) Simulated EPR spectrum of randomly-oriented nitroxide sample undergoing no rotational motion.

The orientational dependence of nitroxide EPR spectra also render them sensitive to rotational motion, which can change the orientation of the probe relative to H_0 and potentially average both the g and T anisotropies. Molecular rotational motions are described in terms of the rotational correlation time, τ_R, which represents the average time needed for a molecule to diffuse one radian. In conventional EPR, rotational motions with a correlation time comparable to the excited state lifetime (i.e., $\tau_R \sim T_2$) will partially or completely average spectral anisotropy (Fig. 15). At τ_R values $\geq 10^{-6}$ s, rotational motion is too slow relative to T_2 to influence the spectrum, while somewhat faster motions ($\tau_R \sim 10^{-7}$ s) broaden the spectrum by carrying excited spins on and off
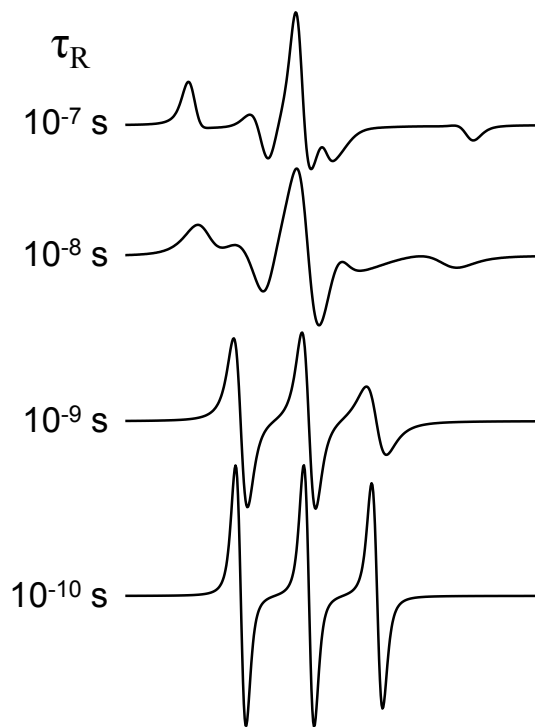
Fig. 15. Effects of rotational motion on randomly-oriented nitroxide V$_1$ spectra. Rotational motion averages the anisotropies of both the *g* factor and the hyperfine splitting (*T*) when τ_R is comparable to T_2. At long correlation times ($\tau_R \geq 10^{-6}$), rotational motion is too slow to significantly influence the spectrum, while faster motions gradually average the *g* and *T* anisotropies until the fast (isotropic) limit is reached ($\tau_R \leq 10^{-10}$).

resonance, thereby changing their resonance condition and effectively decreasing their lifetime. As the rate of rotational motion increases further (τ_R decreases further), the *g* and *T* anisotropies are more effectively averaged until the 'isotropic limit' is reached, where rotational motion completely averages spectral anisotropy.

2.6   Saturation EPR Techniques

Conventional (V$_1$) EPR spectra are generally acquired under non-saturating conditions (low microwave power) that only marginally perturb the Boltzmann distribution of spins. However, measuring the behavior of saturated spin systems can expand the utility of CW EPR beyond measuring ps – ns rotation. This section introduces two CW EPR techniques

that exploit saturation to study the μs – ms rotational motions and local environment of spin-labeled proteins.

Saturation-transfer EPR. As described in Section 2.4, conventional EPR spectra are acquired by gradually increasing the magnetic field while applying a high-frequency, low-amplitude field modulation. This in turn modulates the net microwave absorption, allowing it to be isolated from random microwave noise using a lock-in detector set to the same frequency and phase as the field modulation. If low-power microwaves are used, the Boltzmann distribution of spins remains largely unperturbed with each modulation pass, and microwave absorption stays in phase with the sinusoidal field modulation. If however the applied microwave power is sufficient to deplete the ground state, the modulated field will generate non-equilibrium (saturated) spin packets with each pass and reencounter them in subsequent passes. These saturated spins absorb fewer microwaves, and consequently net absorption will no longer oscillate solely in phase with the field modulation, but instead contain both in-phase (V) and out-of-phase (V′) components. Normally V′ is rejected by the lock-in detector, but one can specifically select for it by setting the detector 90° out of phase with the field modulation. The intensity of V′ is dictated by the extent of spin saturation, which depends on the incident microwave power (i.e. how far the spins are perturbed from equilibrium), the spin-lattice relaxation time T_1 (typically $\sim 10^{-5}$ s), and other phenomena that effectively relieve saturation. By specifically detecting the out-of-phase component, one can study those phenomena that compete with T_1 to relieve saturation.

Recall from Section 2.5 that the resonance condition for a nitroxide spin depends in part on its orientation relative to the magnetic field. For a saturated spin packet, rotation

25

of its constituent spins to new resonance positions (and rotation of unsaturated spins into the saturated resonance position) can relieve saturation by *transferring* it to other portions of the spectrum. Thus rotational motion can change the intensity of V′ by effectively replacing saturated spins with unsaturated ones, so long as the rotational correlation time τ_R is comparable to (or shorter than) T_1. This makes the out-of-phase absorption spectrum acquired under saturating conditions – the *saturation-transfer* spectrum – sensitive to correlation times on the order of $10^{-7} - 10^{-3}$ s [45]. For increased lineshape sensitivity to this timescale, saturation transfer EPR (STEPR) spectra are often acquired as the second harmonic of the out-of-phase absorption signal, abbreviated as $V_2′$.

Fig. 16a depicts STEPR ($V_2′$) spectra as a function of τ_R. At very long correlation times ($\tau_R \geq 10^{-3}$ s), rotational motion is too slow to compete with T_1 for saturation relief, resulting in a significant out-of-phase component and an intense $V_2′$ spectrum. As τ_R decreases, rotational motion begins to compete with T_1 and accordingly the intensity of $V_2′$ decreases until the 'fast limit' is reached ($\tau_R \leq 10^{-7}$ s), where rotation redistributes saturated spins much faster than T_1 can relax them. A calibration plot of the $V_2′$ integrated intensity (I_{ST}) versus τ_R, generated from spin-labeled hemoglobin samples with well-defined rotational correlation times (Fig. 16b) [45], allows one to calculate effective τ_R values from the I_{ST} of experimental STEPR spectra.
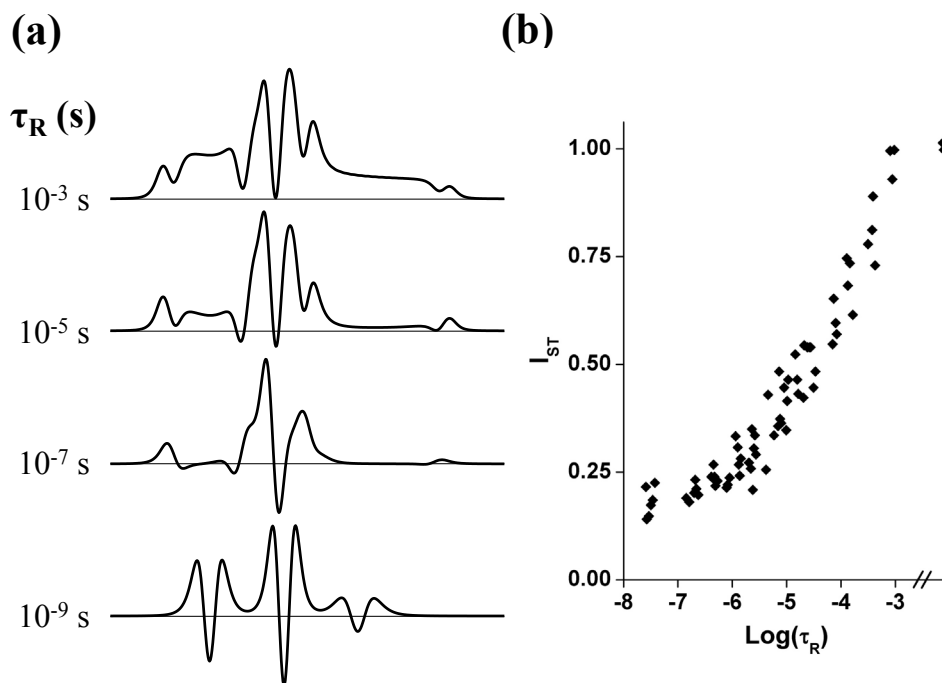
Fig. 16. Dependence of STEPR spectra and I_{ST} on the rotational correlation time. (a) Simulated STEPR spectra as a function of τ_R. (b) Calibration plot of the STEPR spectrum integrated intensity (I_{ST}) versus τ_R, reproduced from [45]

In order for STEPR to detect protein rotation on the μs – ms timescale, the attached spin label must not undergo fast (ps – ns) fluctuations that efficiently transfer saturation and mask the underlying protein motions. On occasion, nitroxides will naturally immobilize on proteins, as is the case with 4-maleimido-TEMPO (MSL) attachment to SERCA, though more often the residual fast motion of spin labels makes STEPR unfeasible. For small proteins amenable to solid-phase peptide synthesis, incorporation of the spin-labeled amino acid TOAC (Fig. 9) offers a truly rigid probe with the nitroxide group coupled directly to the peptide backbone. In Chapter 3, both fortuitous (MSL-SERCA) and designed (TOAC-PLB) spin-label immobilization are used to study μs – ms rotational motions of the SERCA-PLB complex by STEPR.

Accessibility EPR. The effects of saturation on conventional (V_1) EPR spectra can also provide valuable information about the local spin label environment. Besides relaxing

27

directly through T_1 processes, nitroxides may swap their excited states with other paramagnetic centers via Heisenberg exchange, which requires that the exchanging molecule collide with the nitroxide. Exchanging molecules possessing a very short relaxation time will rapidly discard the received energy, and thus Heisenberg exchange can provide spin labels with a new relaxation pathway working alongside T_1 to restore Boltzmann equilibrium. The extent to which nitroxides exploit this new pathway depends on their *accessibility* to these fast-relaxing paramagnetic centers – called paramagnetic relaxation agents (PRAs) – with nitroxides attached to the protein surface exchanging more readily than those buried in the protein interior. For spin-labeled membrane proteins, accessibility is also influenced by the hydrophobicity of the relaxation agent. For example, molecular oxygen (O_2) acts as a lipophilic PRA that forms a gradient across membranes, with spin labels near the bilayer center showing greater O_2 accessibility than those at the membrane surface or in the aqueous phase. In contrast, the hydrophilic relaxation agent nickel(II)ethylenediamine-N,N′-diacetic acid (NiEDDA) forms an opposing gradient (relative to O_2) and is much more accessible to aqueous spin labels than their membrane-embedded counterparts (Fig. 17). Measuring accessibility to both NiEDDA and O_2 provides a metric for determining a spin-label's position relative to the bilayer, and can resolve protein structural changes that carry the probe to different regions of each PRA gradient [46].
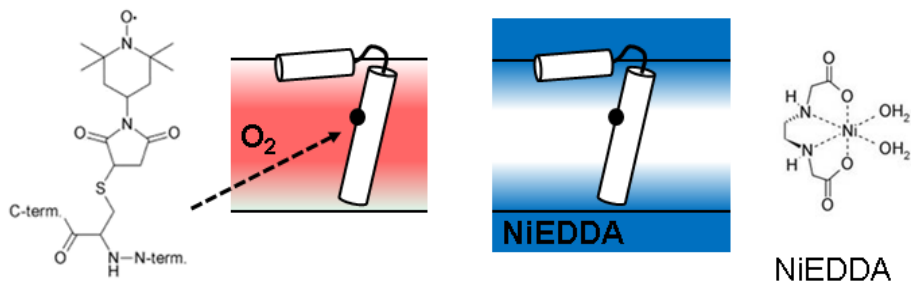
maleimide spin label

Fig. 17. Spin label immersion depth determined by accessibility to hydrophobic and hydrophilic relaxation agents. Intramembrane spin labels (e.g., maleimide spin label attached to PLB domain II) will show differing accessibilities to molecular oxygen (O_2, red) and NiEDDA (blue) that form opposing gradients across the bilayer.

Spin label accessibility to PRAs is quantified through progressive saturation experiments (Fig. 18), where the EPR spectral amplitude is measured while gradually increasing the incident microwave power (MP). At low powers, the amplitude increases linearly with $\sqrt{MP}$, but deviates at higher powers as the spin system begins to saturate. The point where spectral amplitude is half that predicted in the absence of saturation is denoted by $P_{1/2}$, with Heisenberg exchange relieving spin saturation and consequently shifting $P_{1/2}$ to higher powers (Fig. 18A). Progressive saturation data can be fit to Eq. 5 to extract $P_{1/2}$ values:

$$A = I \left[1 + (2^{1/\varepsilon} - 1) \frac{P}{P_{1/2}} \right]^{-\varepsilon} \qquad \text{Eq. 5}$$

where A is the spectral amplitude, I is a scaling factor, and ε measures the homogeneity of the saturation curve [47]. The difference in $P_{1/2}$ measured in the presence and absence of relaxation agents ($P_{1/2,+\text{PRA}} - P_{1/2,-\text{PRA}}$) is proportional to PRA accessibility, denoted by $\Delta P_{1/2}$, and is used to calculate the accessibility parameter φ (Eq. 6):

$$\varphi = ln \frac{\Delta P_{1/2}(O_2)}{\Delta P_{1/2}(NiEDDA)} \qquad \text{Eq. 6}$$

29
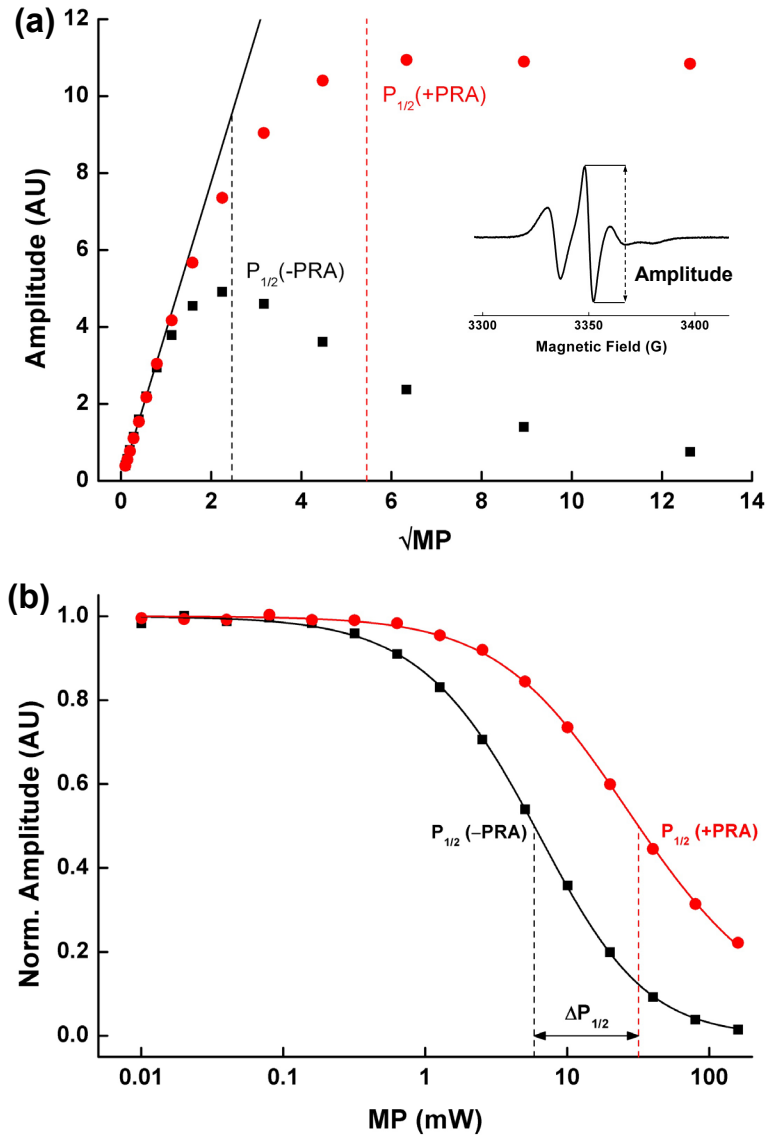
Fig. 18. Progressive saturation EPR in the presence and absence of relaxation agents. (a) Progressive saturation EPR is performed by measuring the spectral amplitude (inset) while increasing the applied microwave power (MP). Amplitude increases linearly with $\sqrt{MP}$ at low powers but eventually saturates. Addition of a relaxation agent (red data) relieves saturation and pushes $P_{1/2}$ to higher powers. (b) Normalized progressive saturation data plotted on a logarithmic scale to emphase $\Delta P_{1/2}$.

When graphing progressive saturation data, it is common to normalize the measured spectral amplitudes to those predicted in the absence of saturation, and to plot the results on a logarithmic scale to emphasize $\Delta P_{1/2}$ (Fig. 18b).

Chapter 3 – Protein-Protein Interactions in Calcium Transport Regulation Probed by Saturation Transfer Electron Paramagnetic Resonance

Zachary M. James[‡], Jesse E. McCaffrey[‡], Kurt D. Torgersen, Christine B. Karim, and David D. Thomas

Department of Biochemistry, Molecular Biology, and Biophysics, University of Minnesota

[‡]Z.M. James and J.E. McCaffrey jointly prepared all EPR and functional samples, and acquired and analyzed all data

3.1 Chapter Overview

We have used electron paramagnetic resonance (EPR) to probe the homo- and hetero-oligomeric interactions of reconstituted sarcoplasmic reticulum Ca-ATPase (SERCA) and its regulator phospholamban (PLB). SERCA is responsible for restoring calcium to the sarcoplasmic reticulum to allow muscle relaxation, while PLB inhibits cardiac SERCA unless phosphorylated at Ser16. To determine whether changes in protein association play essential roles in regulation, we detected the microsecond rotational diffusion of both proteins using saturation transfer EPR (STEPR). Peptide synthesis was used to create a fully functional and monomeric PLB mutant with a spin label rigidly coupled to the backbone of the transmembrane helix, while SERCA was reacted with a Cys-specific spin label. STEPR revealed that sufficiently high lipid/protein ratios minimized self-association for both proteins. Under these dilute conditions, labeled PLB was substantially immobilized following co-reconstitution with unlabeled SERCA, reflecting their association to form the regulatory complex. Ser16 phosphorylation slightly increased this immobilization. Complementary measurements with labeled SERCA showed no change in mobility following co-reconstitution with unlabeled PLB, regardless of its phosphorylation state. We conclude that phosphorylating monomeric PLB can relieve SERCA inhibition without changes in the oligomeric states of these proteins, indicating a structural rearrangement within the heterodimeric regulatory complex.

3.2   Introduction

Muscle relaxation is induced by the active transport of Ca^{2+} from the cytoplasm into the sarcoplasmic reticulum (SR). The SR Ca^{2+}-ATPase (SERCA) is a 994-residue enzyme that transports two Ca^{2+} into the SR lumen per ATP hydrolyzed (Fig. 19, left) [15], resulting in muscle relaxation. In cardiac and slow-twitch muscle, SERCA activity is allosterically regulated by phospholamban (PLB) [49], a 52-residue membrane protein consisting of a 30-residue transmembrane helix and a 16-residue cytosolic helix
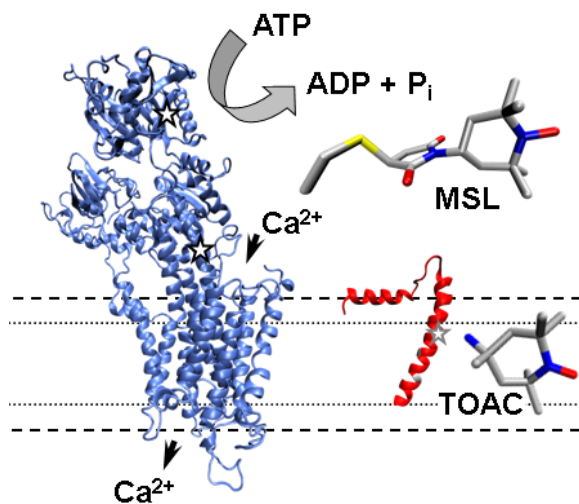
Fig. 19. **SERCA and PLB structures**. Structural models of SERCA (left, crystal structure 1IWO [12]) and monomeric PLB (right, hybrid NMR structure 2KB7 [19]). All experiments in this study were conducted with the monomeric form of PLB. The amino acid TOAC (bottom right), containing a nitroxide spin label rigidly coupled to the α-carbon, is incorporated at position 36 (gray star) on PLB; PLB residues 41 and 46 (gray) are mutated to Phe and Ala. For unlabeled PLB, position 36 is Ala. For spin-labeled SERCA, MSL (top right) is attached at Cys 344/Cys 364 (black star) [48].

connected by a short, flexible loop [50] (Fig. 19, right). PLB inhibits SERCA by decreasing its apparent Ca^{2+} affinity (increasing K_{Ca}) [51]. SERCA inhibition is relieved physiologically either by micromolar $[Ca^{2+}]$ or through PLB phosphorylation at Ser16 by protein kinase A [52], and can also be relieved by PLB point mutations [4, 33, 53].

The regulatory mechanism of the SERCA-PLB complex has considerable therapeutic relevance, since inadequate calcium transport has been strongly linked to heart failure

[54]. Emerging treatments aim to improve cardiac performance by increasing SERCA activity through increased SERCA expression [55], allosteric activation of SERCA by small molecules [56], or reduced PLB inhibitory potency [57, 58]. Elucidating this mechanism would provide a roadmap for the rational design of PLB mutants and drugs designed to activate SERCA.

However, this regulatory mechanism remains controversial. Cross-linking [35] and immunoprecipitation [34] studies suggest that dissociation of the SERCA-PLB complex is required (Fig. 20, Dissociation Model), while spectroscopic studies suggest that PLB remains bound to SERCA following activation by Ser16 phosphorylation [32, 37, 59], Ca^{2+} addition [36], or PLB loss-of-function mutations [58, 59], indicating that a structural rearrangement within the complex can relieve inhibition (Fig. 20, Subunit Model). Furthermore, recent studies have identified multiple PLB conformations within the regulatory complex that correlate with different inhibitory states [32, 60] (see also Chapter 4).

Oligomeric interactions. Distinguishing these regulatory mechanisms is made more
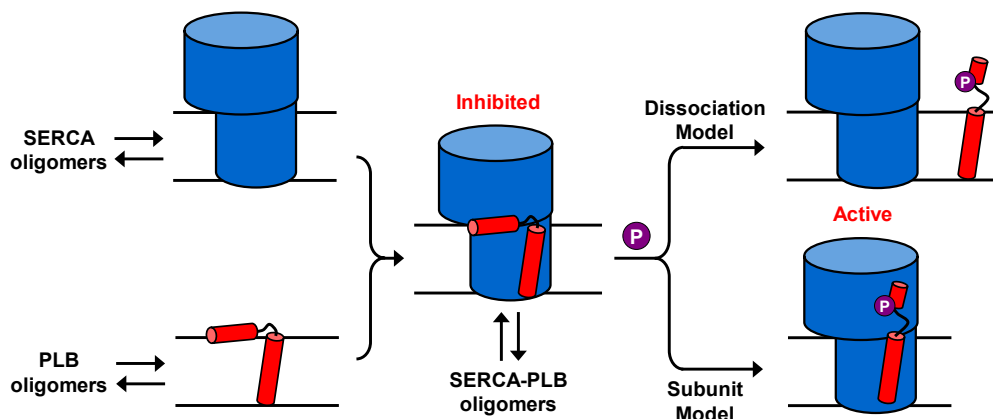
Fig. 20. Oligomeric interactions of SERCA and PLB. Both proteins have homo-oligomeric interactions (left), and bind to form an inhibited SERCA-PLB complex (center). Phosphorylation of PLB relieves inhibition (right), which may occur through dissociation of the complex (Dissociation Model), or a structural rearrangement within the complex (Subunit Model).

difficult by the variety of protein-protein interactions in this system. While the fundamental inhibitory complex is proposed to be a SERCA-PLB heterodimer [49, 61, 62] (Fig. 20, center), both proteins form homo-oligomers that can affect SERCA function (Fig. 20). SERCA may form functioning dimer and trimer states [63, 64], while larger aggregates lead to inhibition [65, 66]. Numerous studies have examined the oligomeric state of SERCA in native [67-69] and reconstituted [65] membranes, and several have investigated the role of the lipid/protein molar ratio (L/P) in modulating SERCA aggregation [66, 70, 71], all based on the proportionality between oligomeric size and rotational correlation time [72]. In cardiac SR, SERCA inhibition and aggregation are both relieved by micromolar Ca^{2+} or PLB phosphorylation [73]. Native PLB equilibrates between monomers and homopentamers, and the latter can be destabilized by mutation (typically leading to increased SERCA inhibition) or stabilized by phosphorylation (leading to decreased SERCA inhibition). Thus inhibition depends, at least in part, on the concentration of PLB monomer [61]. To simplify analysis and focus on SERCA-PLB interactions, we have used (a) a monomeric PLB mutant (AFA-PLB, referred to below as PLB) [74] in which oligomerization is eliminated by replacing Cys residues 36, 41, and 46 with Ala, Phe, and Ala, respectively, and (b) sufficiently high lipid:protein molar ratios (L/P) to minimize self-association of both SERCA and PLB. Thus we are able to focus solely on the heterodimeric interactions between these two proteins.

In the present study, we have characterized the hetero-oligomerization of PLB and SERCA using electron paramagnetic resonance (EPR), while minimizing the homo-oligomerization of both proteins. Rotational motions detected by EPR can be sensitive to oligomeric interactions, since the rotational correlation time (τ_R) of the spin-labeled

protein is proportional to the protein's transmembrane volume [72]. However, conventional EPR is sensitive only to correlation times in the nanosecond range, which is appropriate for rotation of aqueous proteins, but not membrane-embedded proteins, where the viscosity (and thus τ_R) is orders of magnitude greater. Even in fluid lipid bilayers, τ_R values for most integral membrane proteins are in the microsecond range. These slow rotational motions are best measured by saturation transfer EPR (STEPR) [75, 76], which requires the use of spin probes that are immobilized on the labeled protein. In the present study, PLB rotational motion was detected by incorporating the spin label TOAC (2,2,6,6-tetramethylpiperidine-1-oxyl-4-amino-4-carboxylic acid) into the peptide backbone at position 36 in the transmembrane helix (Fig. 19), while SERCA rotational dynamics was detected after covalent reaction with a maleimide spin label (MSL). Both labels have been shown to be rigidly attached to their respective proteins, making them sensitive to rigid-body rotational diffusion that directly reflects the size of the oligomeric complex [29, 67]. We used STEPR to first find conditions where homo-oligomerization was minimized, and then to detect the formation of SERCA-PLB hetero-oligomers so as to discriminate between the Dissociation and Subunit models (Fig. 20).

3.3   Methods

Peptide synthesis. C36TOAC, C41F, C46A, PLB (36-TOAC-AFA-PLB) and C36A, C41F, C46A PLB (AFA-PLB) were synthesized as described previously [29, 77, 78]. Fmoc-TOAC was purchased from Toronto Research Chemicals (North York, Ontario) and Fmoc-protected amino acids were purchased from EMD Chemicals (Philadelphia,

PA). Peptides were purified by reverse-phase HPLC on a preparative C8 column (Grace Vydac, Hesperia CA) using H_2O + 0.1% trifluoroacetic acid and isopropanol as mobile phases. Peptides were characterized by mass spectrometry and SDS-PAGE. Protein concentrations were quantified using a bicinchoninic acid (BCA) assay (Thermo Fisher Scientific, Rockford IL).

SERCA purification and spin labeling. SR vesicles were prepared from rabbit fast-twitch muscle [79], then resuspended to 25 mg/mL total protein in SR buffer (30 mM MOPS, 0.3 M sucrose, pH 7.0). SERCA was purified by reactive red chromatography [80], omitting reducing agents. For spin labeling, SERCA was diluted to 10 mg/mL with SR buffer, to which 300 μM MSL was added from a 50 mM stock in dimethylformamide. After stirring 1 hr at 25 °C, labeled vesicles were diluted tenfold in SR buffer and centrifuged 45 min at 30,000*g* (4 °C) to remove unreacted MSL. The resulting pellet was resuspended in SR buffer and purified as above. Protein concentrations were quantified using a BCA assay.

Reconstitution of SERCA and PLB. Functional reconstitution of SERCA and PLB was carried out as described previously, using 4:1 DOPC/DOPE (mol/mol) to yield unilamellar vesicles that are optimal for reproducing physiological SERCA-PLB regulatory function [81, 82]. These vesicles have an average diameter of 100 nm [82] and thus rotate too slowly to affect our saturation transfer EPR spectra [83, 84]. Final buffer composition of EPR samples was 50 mM MOPS, 50 mM KCl, 5 mM $MgCl_2$, 0.5 mM EGTA, 210 μM $CaCl_2$, pH 7.0, resulting in pCa 6.5 to give optimal regulation of SERCA by PLB [36]. Identical buffer conditions were used in functional assays, except that $CaCl_2$ was varied in order to vary pCa ($-\log_{10}[Ca^{2+}]$). An enzyme-coupled ATPase assay

was used to measure the Ca-dependence of SERCA activity as described previously [58, 81]. As in previous publications from our laboratory, EPR experiments were performed at 4 °C to maintain protein stability during lengthy STEPR experiments, while functional measurements were performed at 25 °C to enhance SERCA activity and permit comparison to published work. PLB inhibitory potency is only weakly dependent on temperature [85]. For phosphorylation, the PLB/lipid/detergent mixture (containing 20 μM PLB, before SERCA addition) was incubated 2 hr at 25 °C with 200 IU/mL bovine protein kinase A catalytic subunit (Sigma, St. Louis MO) and 1 mM MgATP. Complete PLB phosphorylation (> 92%) was confirmed by quantitative Western blotting [86] using 10–20% tris-tricine gels (Bio-Rad, Hercules CA).

EPR spectroscopy and data analysis. Before EPR experiments, samples were centrifuged 1 hr at 200,000g (4 °C) and the pellets resuspended in minimal buffer. 40 μL samples were loaded into 22-gauge Teflon tubing (Amazon Supply, Miami Lakes FL) threaded through a glass capillary (Wiretrol, Drummond Scientific Company, Broomall PA) flame-sealed at one end. The Teflon tubing extended 1 cm from the end of the capillary and was plugged with Critoseal (Krackeler Scientific, Albany NY). Spectra were acquired at X-band (9.5 GHz) with a Bruker EleXsys E500 spectrometer equipped with the ER 4122 SHQ cavity. Temperature was maintained at 4 ± 0.2 °C with a quartz dewar insert and a nitrogen gas flow temperature controller. Spectra were acquired after sample deoxygenation under nitrogen gas (~1 hr) to eliminate the dependence of spectra on oxygen accessibility [45]. Microwave field amplitude H_1 (G) was calibrated with a solution of 0.9 mM PADS, 50 mM K_2CO_3 [45].

Spectral acquisition parameters were set according to Squier et al. [45]. Conventional (V_1, first harmonic, in-phase) EPR spectra were acquired with $H_1 = 0.14$ G microwave field amplitude, 100 kHz modulation frequency, 2 G modulation amplitude, and 120 G sweep width. V_1 spectra used for normalization were acquired as above except that H_1 was set to 0.032 G. STEPR (V_2', second harmonic, out-of-phase) spectra were acquired with 50 kHz modulation frequency, 5 G modulation amplitude, and 120 G sweep-width. After null phase determination by minimizing the signal at non-saturating microwave intensity ($H_1 = 0.032$ G), H_1 was increased to 0.25 G and the V_2' spectrum recorded. All EPR spectra were baseline-corrected and then normalized, either to $\iint V_1$ (conventional EPR) or to $\iint V_1 / H_1$ for $H_1 = 0.032$ G (STEPR). V_1 EPR spectra near the slow-motion limit were analyzed by evaluating lineshape features Δ_L' (the outer half-width of the low-field line, which increases with spin-spin interaction and rotational motion) and $2T_\parallel'$ (the splitting between outer extrema, which decreases with rotational motion but not with spin-spin interaction) [87, 88].

For V_2' spectra, effective rotational correlation times were calculated from an integrated intensity parameter (I_{ST}), using a correlation plot created from MSL-hemoglobin samples in glycerol [45]. I_{ST} reports an effective rotational correlation time that is minimally sensitive to modulation phase errors and thus provides greater precision than provided by lineshape parameters [45].

Data plots were produced with Origin 8.1. Error bars are SEM (n = 3-5). When no error bar is visible, this indicates that SEM is smaller than the plotted symbol.

3.4 Results

Functional Assays. To confirm that 36-TOAC-PLB retained regulatory function, we reconstituted it with SERCA into 4:1 (mol/mol) DOPC/DOPE (1,2-dioleoyl-*sn*-glycero-3-phosphocholine, 1,2-dioleoyl-sn-glycero-3-phosphoethanolamine) vesicles at 700 lipids/SERCA (mol/mol) and measured Ca-dependent ATPase activity using a coupled-enzyme assay [81]. Results were fit by the Hill equation (Eq. 7):

$$V = \frac{V_{max}}{1 + 10^{-n(pK_{Ca} - p_{Ca})}} \qquad \text{Eq. 7}$$

where V is the ATPase rate, V_{max} is the ATPase rate at saturating $[Ca^{2+}]$, n is the Hill coefficient, and pK_{Ca} is the pCa (-log[Ca]) where activity is half-maximal. PLB inhibitory potency, defined as the decrease in pK_{Ca}, was indistinguishable between our spin-labeled construct and unlabeled PLB controls. At 10 PLB/SERCA, where inhibition is maximal, pK_{Ca} shifted from 6.48 ± 0.01 to 6.00 ± 0.01 (inhibitory potency = 0.48 ± 0.02). When PLB was completely phosphorylated (> 92%), inhibition was partially reversed,
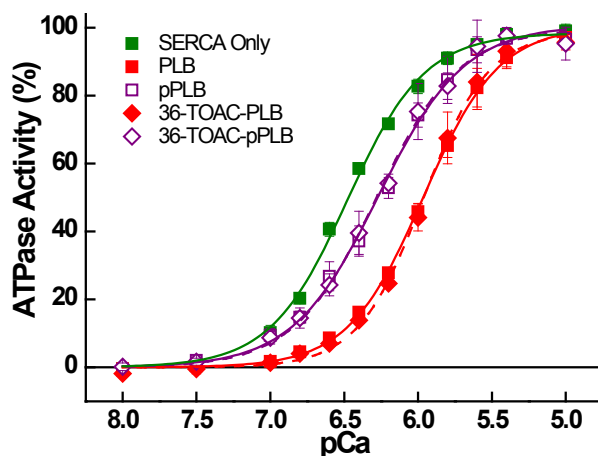
Fig. 21. Ca-dependence of ATPase activity. Samples were reconstituted at 700 lipids/SERCA and 10 PLB/SERCA (mol/mol). ATP turnover was measured at 25 °C, fit by Eq. 7, and normalized to V_{max}. SERCA-only controls (circles) were compared to samples containing PLB (closed squares), 36-TOAC-PLB (closed diamonds), and their pSer16 counterparts (open squares and diamonds). pK_{Ca} values obtained from the fits were used to quantify SERCA inhibition, and are summarized in Table S1.

40

increasing pK_{Ca} to 6.30 ± 0.01 (inhibitory potency = 0.18 ± 0.02) and restoring SERCA Ca sensitivity to the same extent as phosphorylating unlabeled PLB (Fig. 21). At 0.5 PLB/SERCA, matching the conditions of some experiments below, the inhibitory potency of 36-TOAC-PLB was 0.28 ± 0.03 (unphosphorylated) and 0.12 ± 0.04 (phosphorylated). These results, including the partial reversal of inhibition by phosphorylation, are similar to those reported previously for other PLB derivatives [29, 32] and demonstrate that 36-TOAC-PLB regulates SERCA normally. We also used functional assays to determine whether reacting SERCA with MSL affected its interaction with PLB. While MSL decreased V_{max} by ~30% as reported previously [69], pK_{Ca} regulation by PLB was unaltered, indicating that the label does not perturb regulatory interactions between the two proteins.

Monomeric mutant AFA-PLB does not aggregate. Our goal was to find conditions in which self-association is minimized for both PLB and SERCA. We used conventional and saturation transfer EPR to examine spin-labeled PLB or SERCA reconstituted at several L/P. Conventional EPR of 36-TOAC-PLB detected only a marginal decrease in outer splitting ($2T_{\parallel}'$, Fig. 22) with increasing L/P, indicating little or no change in nanosecond rotational dynamics. However, lipid dilution did lead to a substantial decrease in the linewidth (Δ_L') (Fig. 22b), which could arise from decreased nanosecond rotational mobility [87, 88], but this is inconsistent with the lack of increased splitting
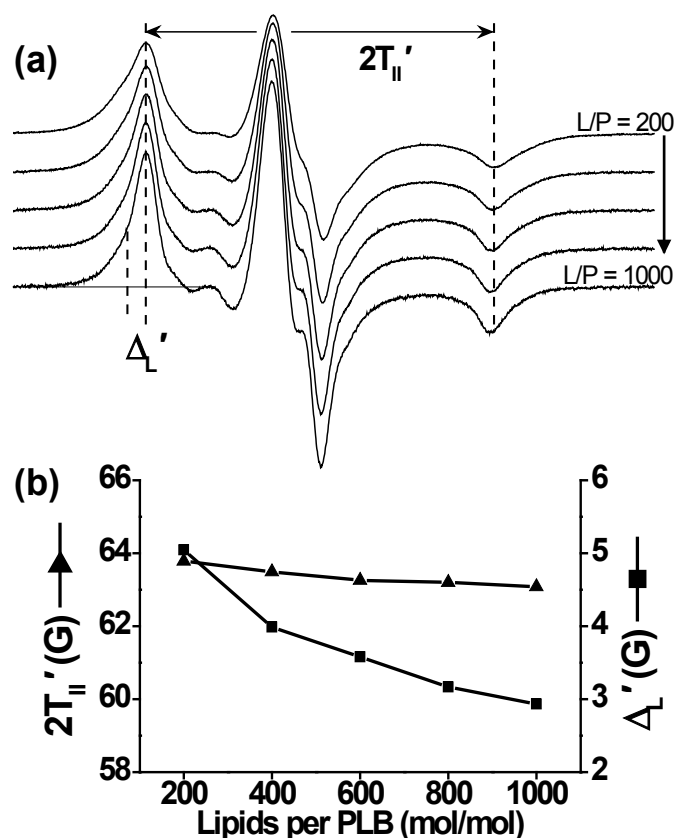
Fig. 22: **Dependence of conventional EPR spectra of 36-TOAC-PLB on lipid/protein ratio.** (a) Spectra of 36-TOAC-PLB reconstituted at 200–1000 L/P (b) Outer splitting ($2T_{\parallel}'$, squares) and low-field outer linewidth (Δ_L', triangles) as a function of L/P. The vertical scales were set so that a change in rotational motion would yield changes in Δ_L' and $2T_{\parallel}'$ of similar magnitude (but opposite sign) [87, 88]. STEPR spectra are given in Fig. S28.

(Fig. 22b). Thus the linewidth decrease is due to decreased dipolar broadening from spin-spin interactions, but the observed broadening is precisely that expected for a random two-dimensional arrangement of monomers in the membrane [89], and would be much greater if PLB oligomers were present, as demonstrated by Fig. S26 and Fig. S27. STEPR spectra support this interpretation (Fig. S28). Thus this PLB construct remains predominantly monomeric at all L/P tested here.

SERCA does not aggregate above 600 L/P. We conducted similar lipid-dilution experiments with MSL-SERCA. Conventional EPR spectra (Fig. S29) have no significant
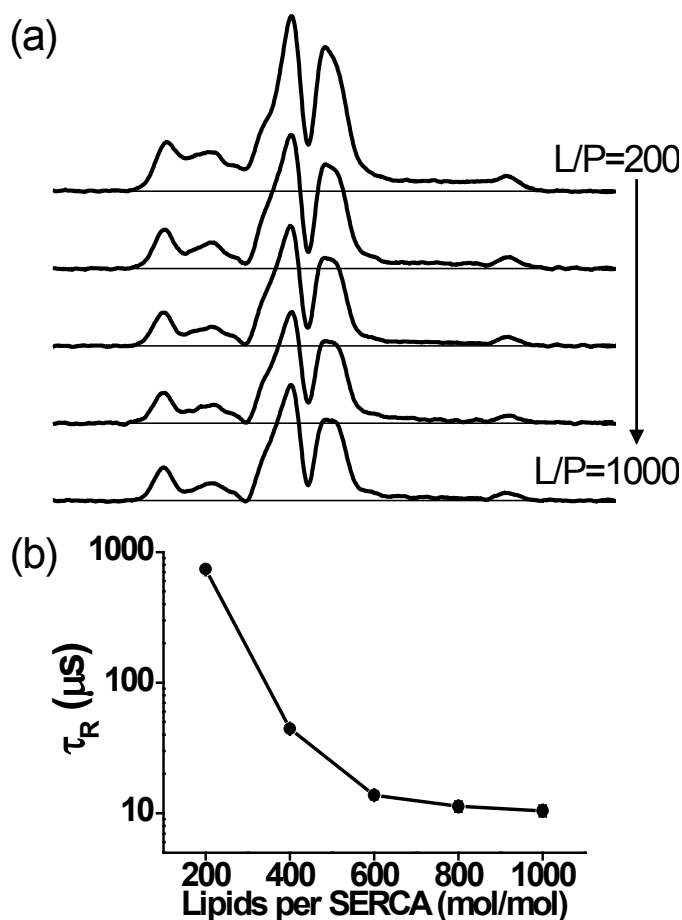
Fig. 23. STEPR of MSL-SERCA as a function of lipid/protein molar ratio (L/P). (a) Representative STEPR (V_2') spectra of reconstituted MSL-SERCA. (b) Effective rotational correlation times (τ_R). Conventional EPR (V_1) spectra are given in Fig. S29.

dependence on L/P, confirming the previous finding that this spin label binds rigidly to SERCA and undergoes no nanosecond rotational dynamics [67]. Thus any changes in STEPR spectra (Fig. 23a) are due to changes in microsecond rotational motion of SERCA about an axis perpendicular to the membrane [67]. These STEPR spectra show that the effective rotational correlation time τ_R decreases substantially from L/P = 200 to 600, to a limiting value of ~12 μs for L/P > 600. This τ_R is consistent with the rotational diffusion of monomeric or dimeric SERCA [68] based on the Saffman-Delbrück equation [72], which predicts that τ_R is proportional to protein transmembrane volume and lipid viscosity. Assuming a membrane height of 4 nm [90] and membrane viscosity of $2-5$ P [91], the Saffman-Delbrück model yields correlation times of $2-4$ μs and $8-19$ μs for SERCA monomers and dimers, respectively. We conclude that SERCA undergoes concentration-dependent self-association, but that this dependence is negligible for L/P > 600, suggesting the presence of stable SERCA monomers or small oligomers. Therefore, further experiments were performed at 700 lipids per SERCA to eliminate the formation of homo-oligomers, allowing us to focus on the SERCA-PLB interaction.

Effects of phosphorylation and SERCA binding on rotational dynamics of spin-labeled PLB. We co-reconstituted 36-TOAC-PLB with SERCA to investigate PLB rotational dynamics within the regulatory complex, using 700 lipids/SERCA and 2 SERCA/PLB to minimize both homo-oligomers and unbound PLB. Conventional EPR spectra of co-reconstituted samples (PLB + SERCA, pPLB + SERCA) and their PLB-only controls (PLB, pPLB) are all near the rigid limit and are virtually identical (Fig.
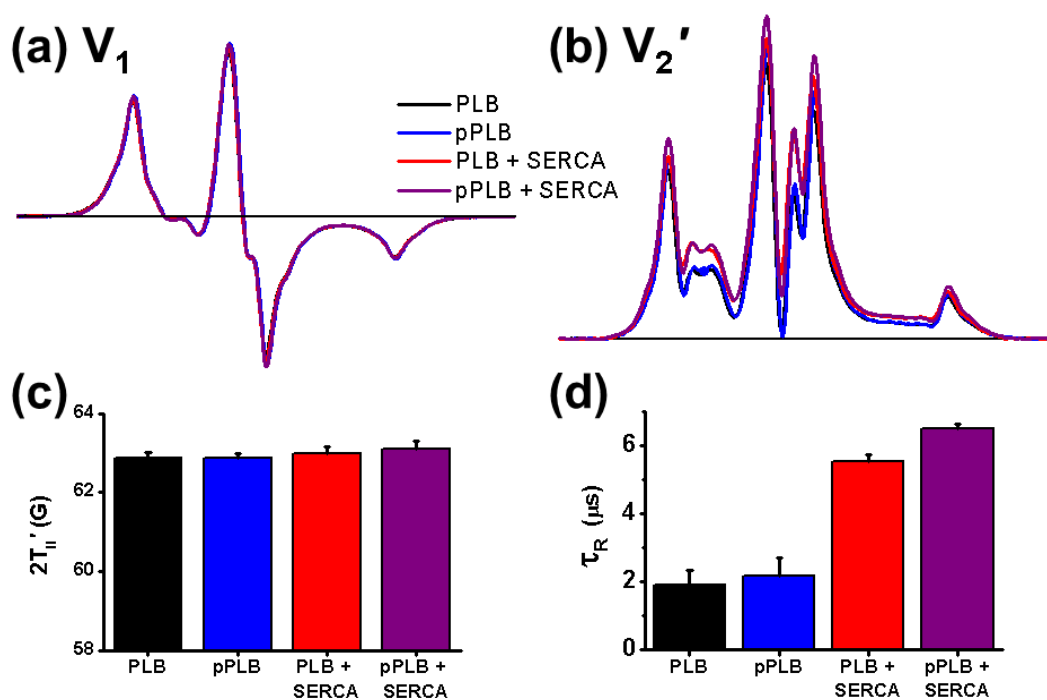
Fig. 24. Effects of Ser16 phosphorylation and SERCA on EPR of 36-TOAC-PLB. (a) Conventional (V_1) EPR spectra and (b) STEPR (V_2') spectra of 36-TOAC-PLB as affected by phosphorylation (pPLB) and/or SERCA (2 SERCA/PLB). (c) Outer splitting $2T_{\parallel}'$ measured from conventional EPR spectra in (a). (d) Effective rotational correlation times from STEPR spectra in (b). Typical normalized spectra are shown in (a) and (b). Bar graphs in (c) and (d) show mean values and SEM for n = 3-5 trials.

24a,c), indicating no change in nanosecond dynamics or self-association of PLB upon phosphorylation and/or SERCA binding. The V_1 EPR spectra in Fig. 24a contain subtle 'shoulders' on the low- and high-field peaks. These could arise from spin-spin interactions (Fig. 22, Fig. S26) or the presence of slow restricted-amplitude rotation [92].

However, the V_1 spectra are not affected by phosphorylation and/or SERCA addition, so the effects on V_2' spectra (Fig. 24b) must arise from changes in microsecond rotational dynamics.

In contrast to the invariant conventional (V_1) spectra (Fig. 24a,c), STEPR (V_2') revealed significant changes in microsecond dynamics (Fig. 24b,d). SERCA decreased PLB mobility substantially, with τ_R increasing from 1.9 ± 0.4 μs (PLB) to 5.6 ± 0.2 μs (PLB + SERCA), consistent with the large increase in SERCA binding. Ser16 phosphorylation had no significant effect on PLB dynamics in the absence of SERCA (Fig. 24b,d), but increased τ_R slightly in the presence of SERCA, from 5.6 ± 0.2 μs to 6.5 ± 0.1 μs (Fig. 24d). This larger τ_R is probably not due to increased binding to SERCA (since that would increase inhibition) or to increased PLB aggregation (since that is inconsistent with the V_1 spectra in Fig. 24a), so it must be due to some structural change of the SERCA-PLB complex that alters either the tilt of the PLB TM domain or the frictional interaction of the SERCA-PLB complex with lipid [93-95]. In any case, it is clear that PLB does not dissociate from SERCA following phosphorylation, since this would cause a substantial *decrease* in the rotational correlation time, making the blue (pPLB) and purple (pPLB + SERCA) spectra identical (Fig. 24b,d). Indeed, a slight *increase* in τ_R was observed due to phosphorylation (Fig. 24d), and the blue and purple spectra are quite different (Fig. 24b), so Fig. 24 clearly contradicts the Dissociation Model and strongly supports the Subunit Model (Fig. 20).

Rotational dynamics of spin-labeled SERCA reconstituted with PLB. To determine whether the results of Fig. 24 were affected by changes in SERCA aggregation, we
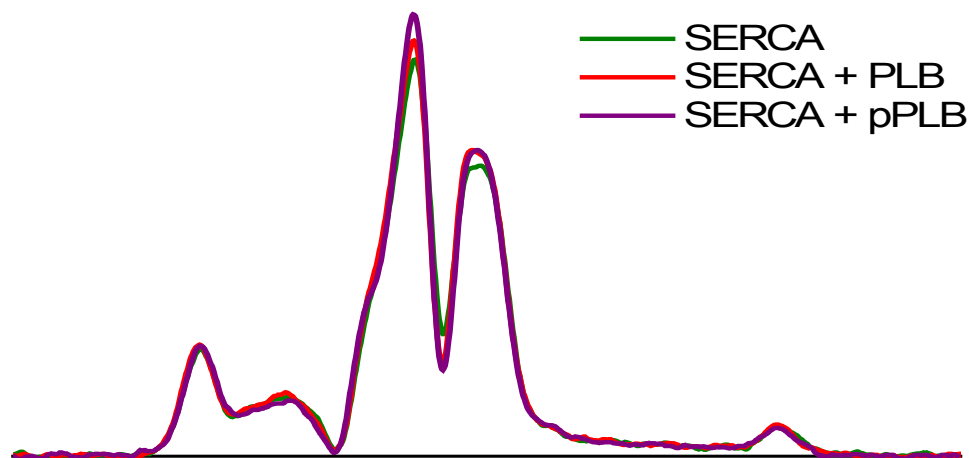
Fig. 25. STEPR (V_2') spectra of MSL-SERCA. Experimental conditions are as in Fig. 24, using MSL-SERCA and unlabeled PLB. Rotational correlation times did not vary significantly among these samples and were consistent with the data in Fig. 23 at 700 lipids/SERCA (13 ± 4 µs). Conventional EPR spectra also showed no significant changes (Fig. S30).

performed identical experiments except using MSL-SERCA and unlabeled PLB. Both V_1 (Fig. S30) and V_2' (Fig. 25) detect no change in SERCA rotational dynamics due to PLB or pPLB. The addition of 0.5 PLB per SERCA should increase the transmembrane volume (and thus the rotational correlation time) by only ~5% [72], within the experimental error of our measurements (~10%, Fig. 24d). This indicates that the aggregation state of SERCA is not significantly perturbed by PLB binding or phosphorylation under these dilute conditions (700 lipids/SERCA and 2 SERCA/PLB), despite substantial functional effects. These findings indicate that regulatory effects of PLB do not arise solely from modulating SERCA aggregation, although such phosphorylation-dependent aggregation does contribute to functional regulation in cardiac SR [73].

Rotational correlation times determined from STEPR spectra are effective, and depend on several parameters that are not easily controlled or evaluated, such as probe orientation relative to the diffusion axis [96] and spin label environment [45]. In addition,

47

it is likely that the TM domain of PLB has residual small-amplitude rotational flexibility relative to SERCA. These factors probably contribute to the significant differences between the V_1 spectra of the SERCA-PLB complex with labeled PLB (Fig. 24a) or labeled SERCA (Fig. S30), and to the shorter τ_R values determined from V_2' spectra of the complex with labeled PLB (Fig. 24b), compared to labeled SERCA (Fig. 25). Therefore, our key conclusions come from comparing the V_2' spectra of a particular spin-labeled protein (36-TOAC-PLB or MSL-SERCA), as perturbed by factors (protein-protein interactions, protein concentration, and phosphorylation) that do not affect the V_1 spectra.

3.5 Discussion

We have used EPR to investigate the tendencies of SERCA and the monomeric AFA-PLB to form homo- and hetero-oligomers in reconstituted membranes. By systematically varying the lipid/protein molar ratio (L/P), we found that SERCA self-association occurs at low L/P but is eliminated for L/P > 600 (Fig. 23), even in the presence of 0.5 PLB/SERCA (Fig. 25). We also showed that TOAC-labeled PLB does not self-associate under the conditions of this study (Fig. 22). Thus the data in Fig. 24 reflect directly the rotational dynamics of PLB alone or in complex with SERCA. Since phosphorylation and SERCA binding caused no significant effects on PLB nanosecond dynamics as detected by conventional EPR (Fig. 24, left), the changes in STEPR (Fig. 24, right) are due to microsecond rigid-body dynamics of PLB. Thus SERCA does immobilize PLB by

48

binding it, but phosphorylation does not dissociate PLB from SERCA, supporting the Subunit Model (Fig. 20, bottom right).

AFA-PLB is monomeric in lipid bilayers at high L/P, even after phosphorylation. While the null-Cys PLB mutant AAA-PLB, similar to AFA-PLB, was found previously to be monomeric by SDS-PAGE [77, 97], solid-state NMR studies suggested that AAA-PLB is substantially aggregated in reconstituted membranes at the extremely low L/P value of 20 [98]. 36-TOAC-AFA-PLB shows substantial broadening of the V_1 spectrum at 20 L/P, consistent with aggregation (Fig. S26), along with dramatic effects on the V_2' spectrum (Fig. S27), showing that PLB aggregation is detectable if present. In contrast, our EPR experiments performed between 200 and 1000 L/P did not reveal significant PLB aggregation (Fig. 22). This is the most direct demonstration to date that AFA-PLB behaves as a monomer in reconstituted bilayers, whether phosphorylated or not. In previous studies, it was shown that the pentameric propensity of wild-type PLB increases with phosphorylation [61], and that SERCA preferentially binds to the PLB monomer [99]. Thus it remains likely that the decrease in PLB monomer concentration due to phosphorylation plays a significant role in relieving SERCA inhibition [61, 100]. However, the present results show that some relief of inhibition by phosphorylation occurs even under conditions where PLB oligomers do not form.

SERCA self-association occurs only at low L/P and is not induced by PLB at high L/P. The oligomeric state of SERCA for optimal function has been postulated to range from monomeric to tetrameric [64, 68, 101-103], while larger aggregates have been shown to decrease SERCA activity, whether induced by crosslinking [104], cationic peptides [105, 106], cationic local anesthetics [107], mismatch in lipid bilayer thickness

[108], small-molecule SERCA inhibitors [63, 109], or PLB [73, 110]. Most importantly, inhibition relief in cardiac SR by either Ca^{2+} or phosphorylation correlates with decreased SERCA aggregation [73]. The present study does not contradict these findings; SERCA aggregation probably plays a significant physiological role in both skeletal and cardiac SR. However, our results show that at low protein concentrations in the membrane (at high L/P), significant changes in SERCA inhibition by PLB occur without significant changes in SERCA aggregation (Fig. 25).

Binding of TOAC-spin-labeled PLB to SERCA is clearly detected by STEPR. STEPR shows that reconstitution with SERCA decreases the microsecond mobility of 36-TOAC-AFA-PLB substantially, consistent with binding (Fig. 24b,d), while conventional EPR detects no change in nanosecond motion or PLB aggregation. This complex formation is consistent with FRET from SERCA to PLB in a similar reconstituted system [60].

Phosphorylation causes a structural change in the SERCA-PLB complex, not dissociation. Phosphorylation of SERCA-bound PLB at Ser16 does not increase its rotational mobility, and thus does not dissociate it from SERCA under conditions of our study (Fig. 24). In fact, an increase in the effective rotational correlation time is observed, indicating a structural change in the SERCA-PLB complex that decreases mobility or changes the tilt of the PLB TM domain. This result supports the Subunit Model (Fig. 20, bottom right), though future studies are needed to characterize the structural change. Since the concentrations of SERCA and PLB, as well as the PLB/SERCA ratio, are much higher in cardiac SR than in the samples considered here, it is unlikely that phosphorylation of PLB causes significant dissociation under physiological conditions.

While previous studies have found that PLB is in dynamic equilibrium between free and SERCA-bound states [58, 111], our data indicates that PLB phosphorylation does not perturb this binding equilibrium significantly.

The present study used the SERCA1a isoform from skeletal SR. There is no known difference between the functional or physical interaction of PLB with SERCA1a and SERCA2a [100, 112, 113], but future studies with the SERCA2a isoform will be needed to rule this out. Previous studies using spin or fluorescent probes of phosphorylated PLB interacting with SERCA are consistent with the conclusions of the present study [32, 37, 59]. However, this is the first study of the SERCA-PLB interaction using a probe rigidly coupled to the transmembrane domain of PLB, thus reporting reliably the rotational mobility of PLB and showing that Ser16 phosphorylation does not dissociate the inhibitory transmembrane domain [77] of PLB from SERCA.

3.6   Conclusions

We have used STEPR to detect the microsecond rotational mobilities of SERCA and AFA-PLB in reconstituted membranes, providing direct insight into their oligomeric interactions, as perturbed by phosphorylation. At L/P $\geq$ 600 and PLB/SERCA = 0.5, SERCA does not change its state of self association due to PLB or pPLB, both of which are strongly immobilized by SERCA binding. Under these conditions, relief of SERCA inhibition must be due to a structural change within the SERCA-PLB complex, not to dissociation of the complex.

3.7   Supplementary Information

Sample	pK_{Ca}
SERCA Only	6.48 ± 0.02
PLB	5.96 ± 0.01
pPLB	6.26 ± 0.02
36-TOAC-PLB	5.97 ± 0.01
36-TOAC-pPLB	6.27 ± 0.02

Table S1. pK_{Ca} values from functional experiments shown in Fig. 21.
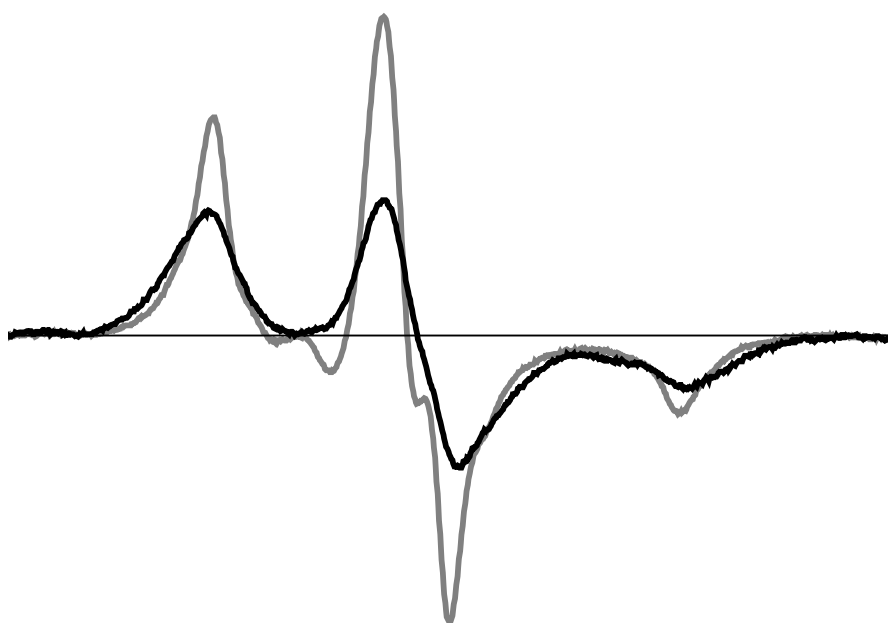
Fig. S26. Conventional EPR spectra of 36-TOAC PLB at 1000 L/P (gray, same conditions as in Fig. 22) and 20 L/P (black), showing greatly enhanced spin-spin interactions due to aggregation at 20 L/P.
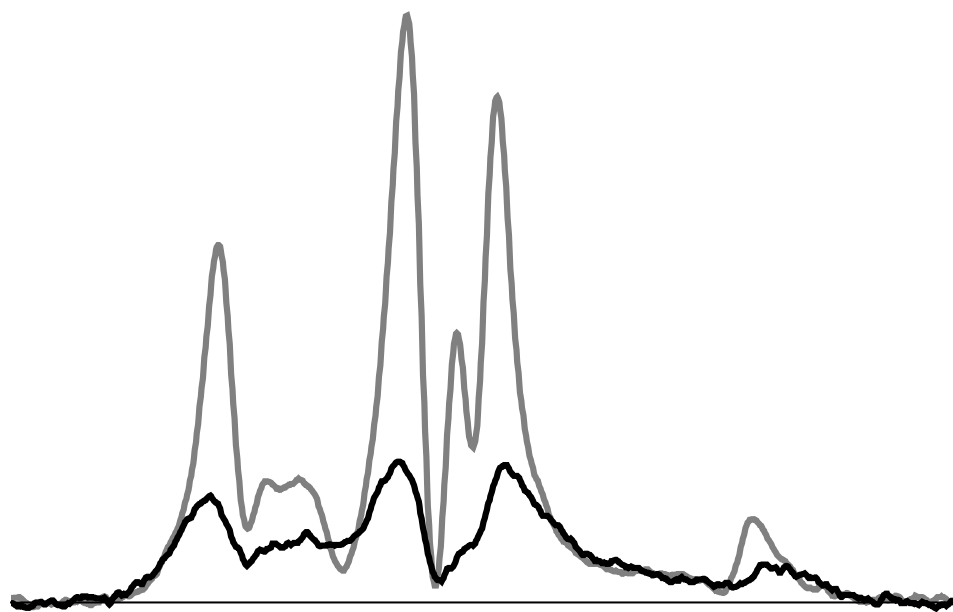
Fig. S27. STEPR spectra of 36-TOAC PLB at 1000 L/P (gray, same conditions as in Fig. 22) and 20 L/P (black). The black spectrum is strongly attenuated by spin-spin interactions [69], which are evident in the conventional EPR spectra of Fig. S26. Thus STEPR is quite sensitive to self-aggregation of this protein, which does not occur above 600 L/P.
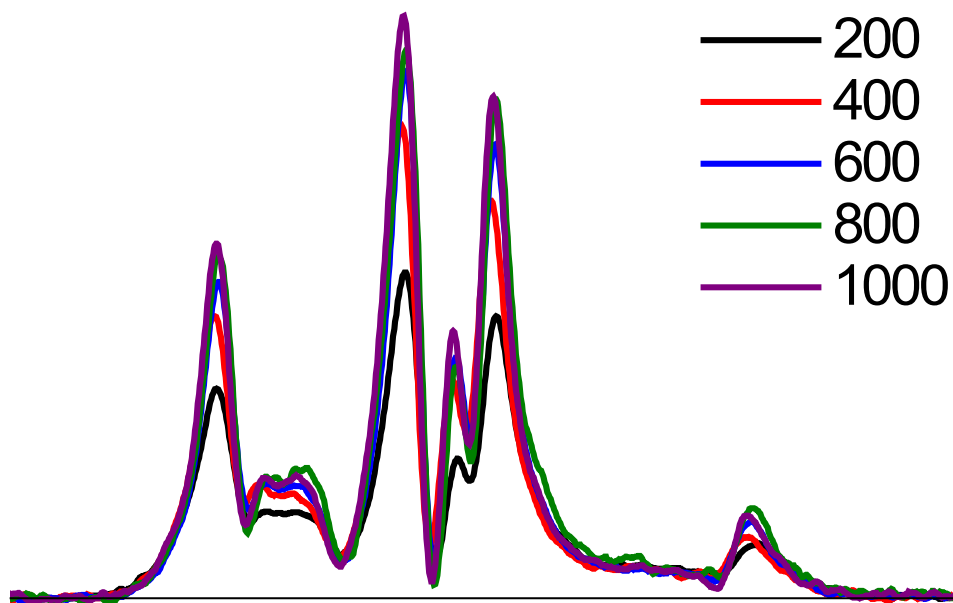
Fig. S28. STEPR spectra of 36-TOAC-PLB as a function of L/P (see figure legend), corresponding to the same samples as in Fig. 22. The increase in spectral intensity with increasing L/P (leveling off at high L/P) is consistent with decreasing spin-spin interactions [69], as documented in Fig. 22. STEPR lineshapes are essentially invariant above 600 L/P, supporting the conclusion that AFA-PLB is monomeric.
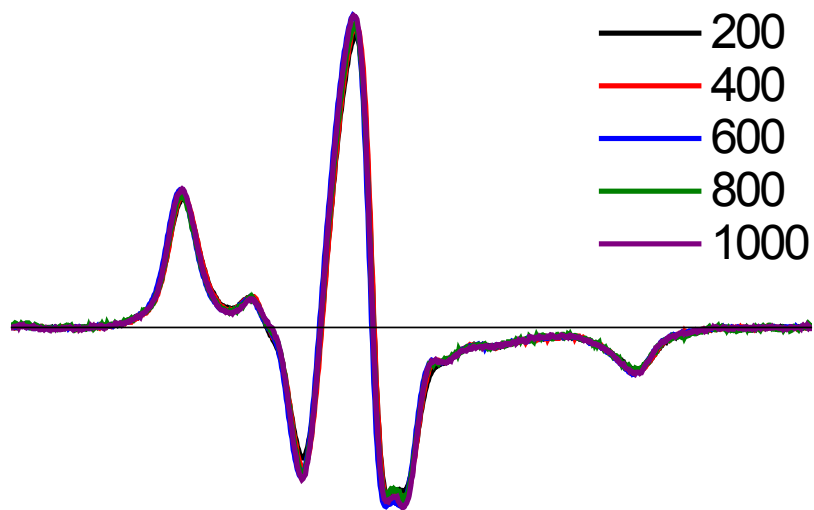
Fig. S29. Conventional EPR spectra of MSL-SERCA as a function of L/P, corresponding to the data shown in Fig. 23. The invariant spectra show that there are no significant changes in nanosecond rotational motion or spin-spin interactions due to variation of L/P, so all changes in STEPR spectra (Fig. 23) are due to µs rotational diffusion of SERCA. Average $2T_{||}' = 68.2$ G.

Fig. S30. Conventional EPR of MSL-SERCA reconstituted with unlabeled PLB, corresponding to the data shown in Fig. 25. The invariant spectra show that there are no significant changes in nanosecond rotational motion or spin-spin interactions due to PLB binding or phosphorylation, so STEPR spectra (Fig. 25) report microsecond rotational diffusion of SERCA.

Chapter 4 – Structural and Functional Dynamics of an Integral Membrane Protein Complex Modulated by Lipid Headgroup Charge

Ji Li, Zachary M. James[‡], Xiaoqiong Dong, Christine B. Karim, and David D. Thomas

Department of Biochemistry, Molecular Biology, and Biophysics, University of Minnesota

[‡]Z.M. James prepared all EPR samples, and acquired and analyzed all EPR data

4.1 Chapter Overview

We have used membrane surface charge to modulate the structural dynamics of an integral membrane protein, phospholamban (PLB), and thereby its functional inhibition of the sarcoplasmic reticulum Ca-ATPase (SERCA). It was previously shown by EPR, in vesicles of neutral lipids, that the PLB cytoplasmic domain is in equilibrium between an ordered *T* state and a dynamically disordered *R* state, and that phosphorylation of PLB increases the *R* state and relieves SERCA inhibition, suggesting that *R* is less inhibitory. Here we sought to control the *T*/*R* equilibrium by an alternative means – varying the lipid headgroup charge, thus perturbing the electrostatic interaction of PLB's cationic cytoplasmic domain with the membrane surface. We resolved the *T* and *R* states not only by EPR in the absence of SERCA, but also by time-resolved fluorescence resonance energy transfer (TR-FRET) from SERCA to PLB, thus probing directly the SERCA-PLB complex. Compared to neutral lipids, anionic lipids increased both the *T* population and SERCA inhibition, while cationic lipids had the opposite effects. In contrast to conventional models, decreased inhibition was not accompanied by decreased binding. We conclude that PLB binds to SERCA in two distinct structural states of the cytoplasmic domain, an inhibitory *T* state that interacts strongly with the membrane surface, and a less inhibitory *R* state that interacts more strongly with the anionic SERCA cytoplasmic domain. Modulating membrane surface charge provides an effective way of investigating the correlation between structural dynamics and function of integral membrane proteins.

4.2   Introduction

The functions of integral membrane proteins depend on the interplay of protein structure and dynamics with the lipid environment [114]. In the present study, we use the lipid environment as a tool to perturb the system, followed by measurement of structure, dynamics, and function, to elucidate mechanistic principles. We vary membrane surface electrostatics by manipulating lipid headgroup charge, which has been shown to be a powerful approach in the analysis of peripheral membrane proteins [115].

The sarcoplasmic reticulum Ca-ATPase (SERCA) actively transports Ca from the cytoplasm to the SR lumen and initiates muscle relaxation. In the cardiomyocyte, an integral membrane protein phospholamban (PLB) [116] regulates SERCA activity by decreasing SERCA's apparent Ca affinity [51]. This inhibition can be relieved by elevated Ca or by phosphorylation of PLB in response to β-adrenergic stimulation [4]. Decreasing this inhibitory regulation relieves cardiomyopathy, so elucidating the interaction mechanism between SERCA and PLB is essential for understanding cardiac pathology and for devising new cardiac therapies [117].

PLB exists in equilibrium between monomeric and pentameric forms, but the monomer is the principle species that binds to and inhibits SERCA [61], so we used the monomeric AFA-PLB mutant (C36A/C41F/C46A) [29, 50] throughout this study. The high-resolution structural dynamics of free PLB monomer in a lipid bilayer has been determined using nuclear magnetic resonance (NMR) and electron paramagnetic resonance (EPR) [19, 29, 32, 50]. PLB consists of an N-terminal cytoplasmic helix, a loop, and a transmembrane helix (Fig. 31). The top of the TM helix (domain Ib) is

hydrophilic, directly interacts with lipid headgroups, and is more dynamic than the rest of the TM helix (domain II) [18, 19, 29]. EPR of TOAC, a spin label attached rigidly to the peptide backbone, shows that the cytoplasmic domain of PLB (Ia and Ib) is in equilibrium between an ordered *T* state and a dynamically disordered (partially unfolded) *R* state (sometimes called "excited state"), while the transmembrane helix is quite stable [29]. The cytoplasmic domain is associated with the membrane surface in *T* but dissociated in *R* [29]. Phosphorylation of PLB induces a shift in the *T*/*R* equilibrium toward *R*, suggesting that *R* is less inhibitory than *T* [32, 118].

Numerous high-resolution structures of SERCA in its enzymatic cycle have been obtained from X-ray diffraction [15, 16], but there is no high-resolution structure of the SERCA-PLB complex. Based on crosslinking, mutagenesis and structures of free SERCA and free PLB, a docking model has been constructed, in which the cytoplasmic domain of PLB extends above the membrane surface and interacts with the cytoplasmic domain of SERCA [34]. Conventional models hypothesize that dissociation of this inhibitory SERCA-PLB complex is necessary for the relief of SERCA inhibition, either by high Ca, phosphorylation of PLB, mutagenesis of PLB, or addition of a PLB antibody [35, 119], but EPR and NMR studies suggest that PLB remains bound to SERCA in both *T* (inhibitory) and *R* (less-inhibitory) states [28, 32, 120]. However, none of these spectroscopic studies probed specifically the bound SERCA-PLB complex.

To help resolve this controversy, in the present study we have probed directly the structure of the SERCA-PLB complex, and we systematically tuned the structural dynamics of the cationic cytoplasmic domain of PLB by adjusting membrane surface charge using charged lipids. We first used EPR [32, 121] of TOAC-PLB in the absence

61

of SERCA, to show that we can control the T/R equilibrium using lipid headgroup charge. We then used time-resolved fluorescence resonance energy transfer (TR-FRET) [122] to directly measure SERCA-PLB binding and simultaneously resolve the T and R structural states of the SERCA-PLB complex (see Appendix A for a brief introduction to FRET). We performed ATPase assays to determine the correlation of these observations with PLB inhibitory function. With this combined approach we constructed a revised model for the structural and functional regulation of the SERCA-PLB complex. This approach has implications far beyond SERCA, demonstrating that variation of membrane surface electrostatics, in conjunction with high-resolution spectroscopy, is a potentially powerful approach to systematically tune the structural and functional dynamics of integral membrane proteins.

4.3 Results

We used lipid headgroup charge as a means of perturbing electrostatically the structural equilibria of the SERCA-PLB system. The advantage of this approach is that it does not alter the native chemical compositions of the proteins, compared with conventional modifications such as mutagenesis, phosphorylation, and crosslinking. All lipids used have the same unsaturated fatty acid chains, di(C18:1), but varying headgroups and charges: phosphatidyl choline (PC, 0), phosphatidyl ethanolamine (PE, 0), phosphatidyl glycerol (PG, −1), phosphatidyl serine (PS, −1), ethyl-phosphocholine (EPC, +1), and trimethyl-ammonium-propane (TAP, +1) (Fig. 31). We hypothesized that the principal effect of this variation of membrane surface charge would be to perturb the equilibrium between the T state (membrane bound and highly ordered) and the R state (dissociated
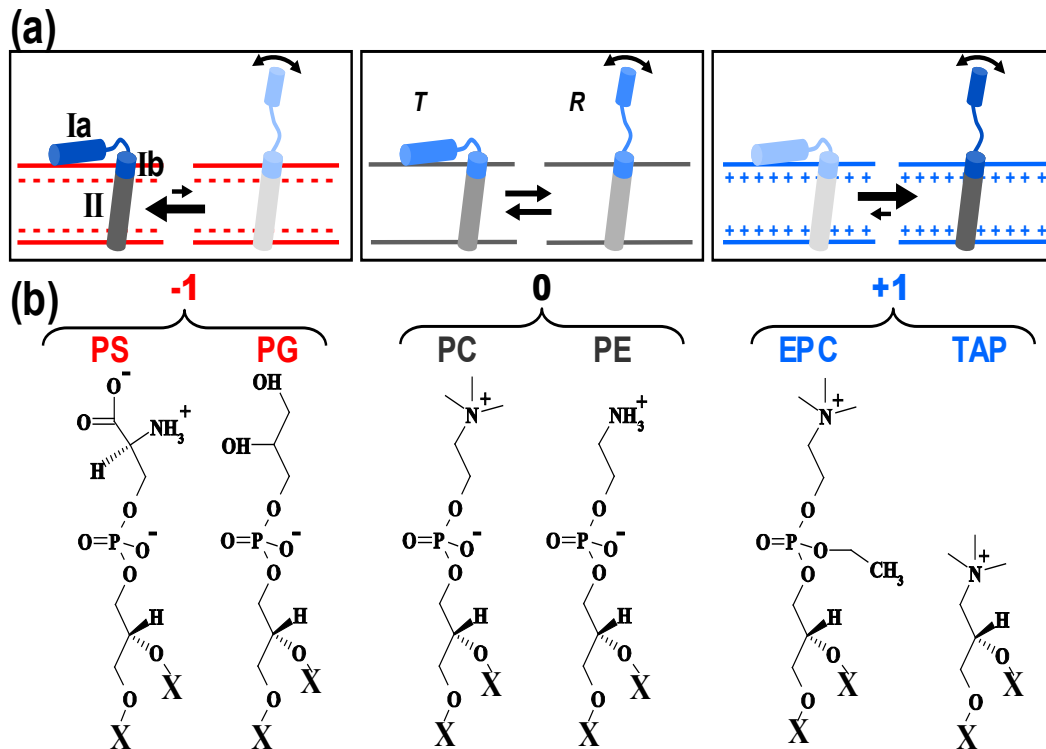
Fig. 31. Tuning the *T/R* equilibrium using lipid headgroup charge. Here and in subsequent figures, red indicates negative charge, blue positive. (a) The cationic cytoplasmic domain (Ia and Ib) of monomeric PLB is in equilibrium between an ordered *T* state and a dynamically disordered *R* state, while domain II is stable [29]. (b) Structures of lipid headgroups and their net charges. All lipids have the same fatty acid chain, X = $C_{18:1}$ (oleic acid).

from the membrane and highly disordered). If our hypothesis is true, negatively charged lipids should increase the *T* state population and SERCA inhibition (Fig. 31, top left), while positively charged lipids should have the opposite effects (Fig. 31, top right). In this work, membranes were composed of PC, PE, and L at molar ratios 4/1/1, where L is PS, PG, PC, EPC, or TAP (Fig. 31, bottom). PC and PE are in all samples, because they are the major constituent lipids in cardiac SR and are important for SERCA activity and PLB-dependent regulation in reconstituted membranes [81, 123]. The molar ratios of SERCA/PLB/lipid, when one or both proteins were present, were 1/10/700, which results in a functional regulation of SERCA by PLB that matches that in the native environment [36, 58].

EPR shows that the PLB structural distribution depends on lipid headgroup charge. We have previously shown that the TOAC spin label, rigidly coupled to the peptide backbone at position 11 on PLB, clearly resolves the T and R states [29, 32, 121]. Therefore, we used this EPR approach to determine the effect of lipid headgroup charge on the T/R equilibrium (Fig. 32). The T state is dynamically restricted, resulting in a broad peak at lower field, while the dynamically disordered R state results in a sharp peak at higher field (Fig. 32a). The positions and shapes of the two components did not change significantly with lipid headgroup charge, indicating that only the populations of the two states were affected. The mole fraction of PLB in the R state (X_R) was determined by digital analysis of EPR spectra as described previously [121] (Fig. 32b). X_R is about 0.20 in zwitterionic PC, while anionic PS and PG decrease X_R substantially and cationic EPC and TAP increase X_R (Fig. 32). These results strongly support the hypothesis in Fig. 31: the T/R equilibrium is influenced by the electrostatic interaction between the cationic cytoplasmic domain of PLB and the membrane surface charge; anionic lipid headgroups attract the cationic PLB cytoplasmic domain to the membrane surface, stabilizing the membrane-associated T state, while cationic lipid headgroups repel the cationic PLB cytoplasmic domain from the membrane surface, stabilizing the R state.

TR-FRET from SERCA to PLB resolves two structural states of the SERCA-PLB complex. To further resolve the structure of the SERCA-PLB complex, we performed TR-FRET to measure the distance between IAEDANS-labeled SERCA (AEDANS-SERCA, donor) and Dabcyl-labeled PLB (Dabcyl-PLB, acceptor). The Förster distance (R_0) between this pair is 3.2 nm [36]. IAEDANS labels SERCA specifically at Cys674, with the molar ratio of bound dye to SERCA = 1.02 ± 0.05 [124]. Synthetic AFA-PLB was labeled by attaching Fmoc-Lys(Dabcyl)-OH to the N-terminus at the last step of synthesis [58]. The time-resolved fluorescence of AEDANS-SERCA without (donor only, $F_D(t)$) or with Dabcyl-AFA-PLB (donor plus acceptor, $F_{D+A}(t)$) was measured by
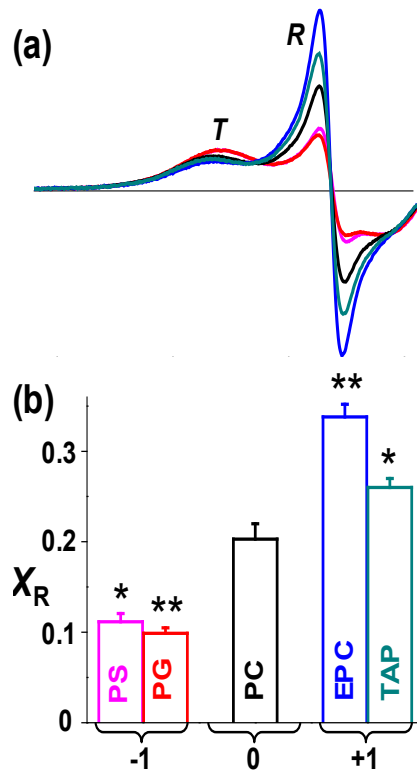
Fig. 32. Effect of lipid headgroup charge on EPR of 11-TOAC spin-labeled PLB in lipid bilayers, with lipid composition and abbreviations as defined in Fig. 31 (color scheme indicated in Fig. 31b). (a) Low-field portion (3305 to 3341 G) of the spectrum resolves two distinct dynamic states of the PLB cytoplasmic domain, an ordered *T* state and a dynamically disordered *R* state. (b) Mole fraction of *R* state (X_R). Mean $\pm$ SEM (n = 3). Students *t*-test, compared with PC: * $P < 0.05$, ** $P < 0.01$.

direct waveform recording using a high-performance time-resolved fluorescence instrument [125] (see section 4.5) (Fig. 33a), then analyzed (Eq. S9 - Eq. S15) using non-linear fitting software. Conventional steady-state FRET only measures the ensemble-averaged interprobe distance. The principal advantage of TR-FRET is that it resolves directly the fraction X_b of the donor that has acceptor bound, thus reporting directly the structure of the SERCA-PLB complex (Eq. S12 - Eq. S15). Within this bound complex, TR-FRET also resolves multiple structural states, as defined by Gaussian interprobe distance distributions, each characterized by the center (R_i), width ($FWHM_i$), and mole fraction (x_i) (Eq. S12 - Eq. S15) [122, 126]. For the bound complex in PC, two Gaussian components are necessary and sufficient to fit $F_{DA}(t)$ (Fig. 33b, Fig. S38). The shorter interprobe distance (R_1) is 1.75 ± 0.03 nm, with width $FWHM_1$ = 0.99 ± 0.07 nm and mole fraction x_1 = 0.77 ± 0.02. The longer interprobe distance (R_2) is 3.03 ± 0.02 nm, with $FWHM_2$ being 1.67 ± 0.24 nm, and x_2 = 1 - x_1 = 0.23 ± 0.02. The fraction of SERCA bound to PLB (Eq. S14), is X_b = 0.82 ± 0.01 in PC, indicating that 82% of SERCA is bound to PLB. These results support the model that the complex between SERCA and PLB is in equilibrium between two structural states (Fig. 33), as is PLB in the absence of SERCA (Fig. 32).
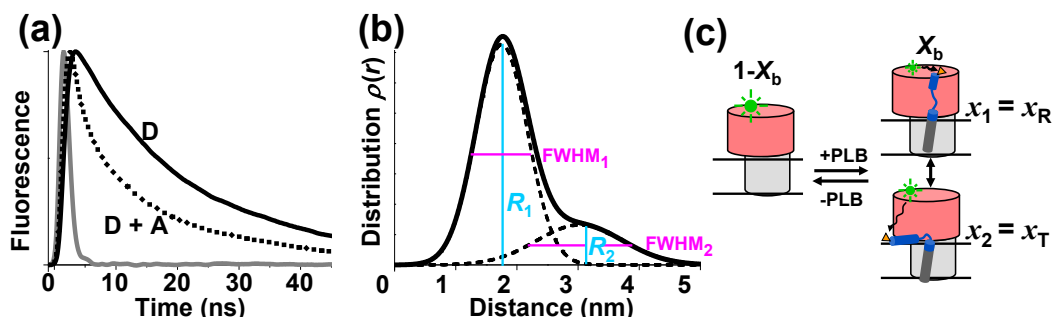
Fig. 33. TR-FRET from AEDANS-SERCA (donor) to Dabcyl-PLB (acceptor) in PC. (a) Example of TR fluorescence, measured by direct waveform recording in PC membranes. D = donor-only, D+A = donor plus acceptor. Gray = instrument response function (IRF). (b) SERCA-PLB interprobe distance distribution determined from data in a, containing two Gaussian components (solid curve = sum of two dashed curves), centered at R_1 and R_2. (c) TR-FRET data resolves free SERCA (left, mole fraction $1-X_b$) from PLB-bound SERCA-PLB (right, X_b). Two structural states of the bound SERCA-PLB complex are resolved (b), consistent with the model shown here. x_1 and x_2 are the mole fractions of the two states, corresponding to bound **T** and **R** states, as shown below.

Ensemble average FRET shows that the average interprobe distance between SERCA and PLB is affected by lipid headgroup charge. Ensemble-average FRET efficiency $\langle E_{D+A} \rangle$ (Fig. 34a) was calculated using the average lifetime (Eq. S11), which is equivalent to (but more precise than) FRET efficiency measured by fluorescence intensity under steady illumination [127]. Compared to zwitterionic PC, anionic PS and PG decreased FRET, suggesting an increase in the average interprobe distance, while cationic EPC and TAP increased the ensemble-average FRET, suggesting a decreased average interprobe distance (Fig. 34a). These results suggest that the proximity between SERCA and PLB is affected by the electrostatic interaction between the lipid headgroup and the PLB cytoplasmic domain. However, this ensemble average measurement has no structural resolution, so it can not distinguish a change in binding from a change in the structure of the complex. Only TR-FRET can resolve the ambiguity.
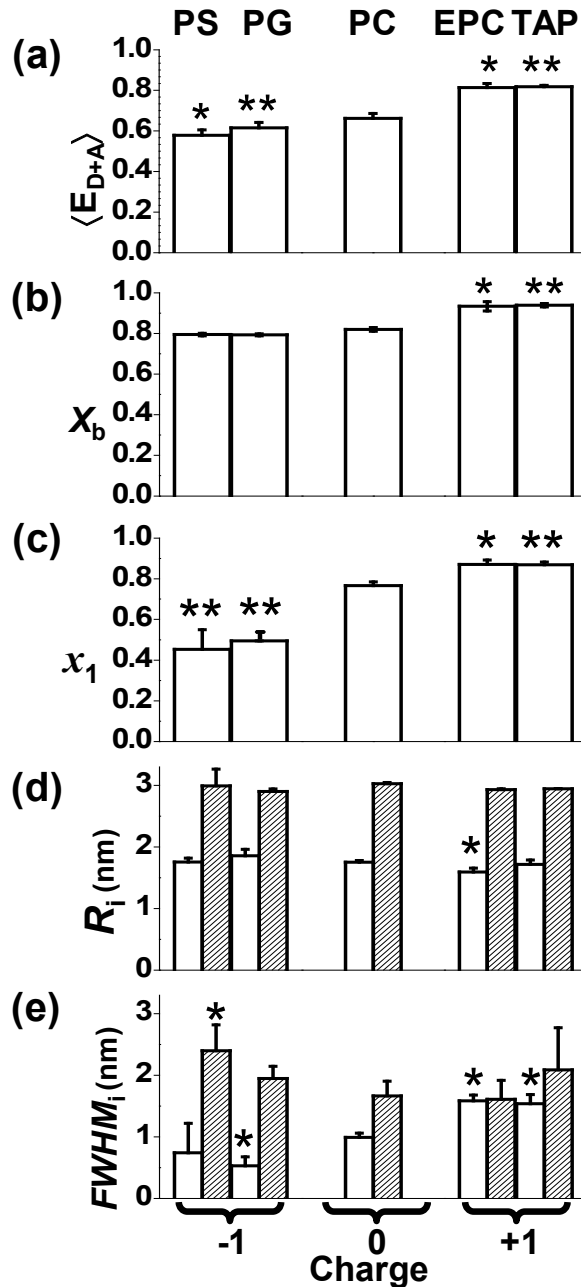
Fig. 34. Effects of lipid charge on SERCA-PLB structural distribution, determined from TR-FRET. Two-Gaussian components distance distributions were determined as in Fig. 33. Students t-test, compared with PC: $* P < 0.05$, $** P < 0.01$. (a) Ensemble average FRET. (b) Mole fraction of SERCA bound to PLB. (c) Mole fraction of the short distance state ($x_1 = x_R$). (d) Centers R_1 (open) and R_2 (shaded) of the two distance distributions. (e) Widths.

Lipid headgroup charge modulates the distribution of the two structural states of the SERCA-PLB complex. TR-FRET waveforms were fitted as described in Fig. 33. In all cases, across the five different lipid compositions, two structural states were found to

68

be necessary and sufficient to fit the data. The independently determined parameters (Fig. 34b-e) were the fraction of SERCA bound to PLB (X_b) and mole fractions of bound states (x_1 and x_2) (Fig. 33c), along with the structural characteristics of each bound state (R_1, $FWHM_1$, R_2, $FWHM_2$) (Eq. S9 - Eq. S15) (Fig. 33b). Membrane surface charge only slightly affects the binding (X_b) between SERCA and PLB (Fig. 34b). In PS, PG and PC, X_b is ~ 0.8, while in EPC and TAP, X_b is ~ 0.9. Thus, most SERCA has PLB bound, and these small effects cannot explain the substantial dependence of $\langle E_{D+A} \rangle$ on charge (Fig. 34a). The two structural states have consistent properties, justifying their being treated as 'states.' The central interprobe distances of the two SERCA-PLB structural states were found to be quite invariant, with a short distance R_1 ~ 1.8 nm, and a long distance R_2 ~ 3.0 nm (Fig. 34d). Some of the widths ($FWHM_i$, defining the structural heterogeneity) of the distance distributions are slightly dependent on lipid headgroup charge (Fig. 34e).

The most prominent effect of membrane surface charge is to shift the equilibrium between the two structural states (Fig. 34c). Compared to zwitterionic PC ($x_1 = 0.77 \pm 0.02$), anionic PS and PG decrease x_1 to 0.45 ± 0.10 and 0.49 ± 0.05 respectively. Cationic EPC and TAP increase x_1 to 0.87 ± 0.02 and 0.87 ± 0.01 respectively. Thus in both isolated PLB (EPR in Fig. 32) and in the SERCA-PLB complex (TR-FRET in Fig. 34), the electrostatic interaction between the cytoplasmic domain of PLB and the membrane surface charge shifts the structural equilibrium between two structural states.
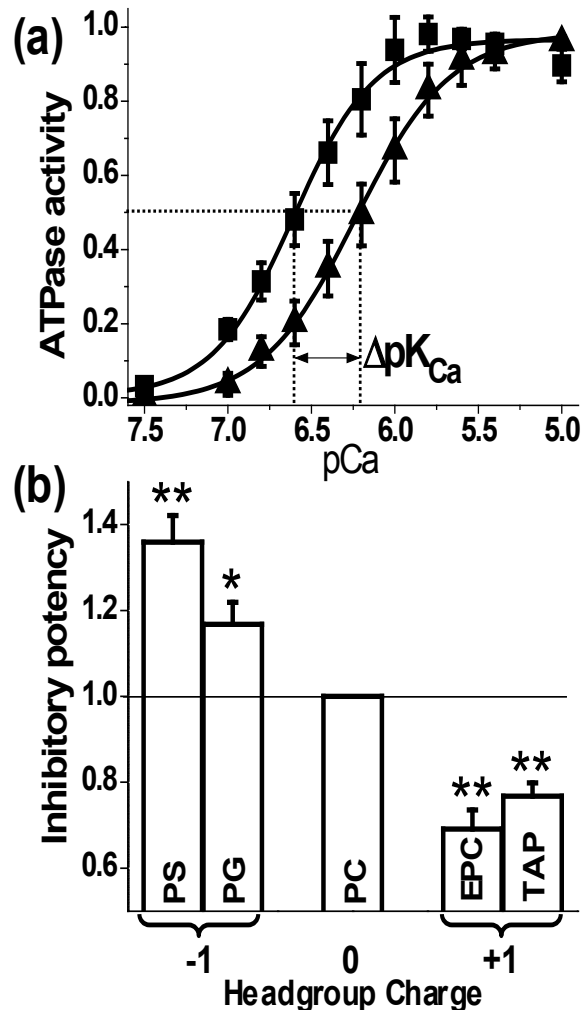
Fig. 35 Effects of lipid headgroup charge on SERCA inhibition. (a) Activity of SERCA in PC without (■) and with (▲) AFA-PLB. Solid curves are the best fit using Eq. 7. Error bars are SEM (n = 4). (b) Inhibitory potency, defined as ΔpK_{Ca} normalized to the value for PC (mean $\pm$ SEM. n = 4-6). Students t-test, compared with PC: * $P < 0.05$, ** $P < 0.01$.

Based on a comparison between EPR and TR-FRET data, it appears that population 1, the short distance state detected by TR-FRET, corresponds to the $\boldsymbol{R}$ state, while population 2 corresponds to the $\boldsymbol{T}$ state, as depicted in Fig. 33c. Negative surface charge attracts the positively charged PLB cytoplasmic domain and thus increases the fraction ($x_2 = x_T$) of the membrane-associated bound $\boldsymbol{T}$ state (long interprobe distance), while positively charged headgroups have the opposite effect and thus increase the bound $\boldsymbol{R}$ state fraction ($x_1 = x_R$).

SERCA activity in the absence of PLB depends on lipid headgroup charge. To establish control values, the ATPase activity of SERCA alone was measured at different pCa, and the pCa-dependence was fitted using Eq. 7. There were no significant effects on the V_{max} (activity at saturating Ca), but there were significant effects of headgroup charge on pK_{Ca}, defining the apparent Ca affinity (Table 2). Compared to PC (zwitterionic), PS and PG (anionic) increase pK_{Ca}, while EPC and TAP (cationic) decrease it.

Table 2. Lipid charge effects on SERCA activity (Eq. 7). (Mean $\pm$ SEM. n $\geq$ 4)

Lipid (charge)	pK_{Ca}	V_{max}
PS (-)	6.81 $\pm$ 0.01	1.65 $\pm$ 0.03
PG (-)	6.73 $\pm$ 0.02	1.55 $\pm$ 0.12
PC (0)	6.68 $\pm$ 0.02	1.65 $\pm$ 0.19
EPC (+)	6.53 $\pm$ 0.03	1.46 $\pm$ 0.10
TAP (+)	6.51 $\pm$ 0.02	1.66 $\pm$ 0.19

Lipid headgroup charge affects SERCA inhibition by PLB. The inhibitory function of

PLB is defined by its shift of the apparent SERCA Ca affinity, ΔpK_{Ca} (Fig. 35a, Eq. 8). In

order to compare the inhibitory potency of PLB in various lipid environments, ΔpK_{Ca} was

normalized to the value obtained with PC (Fig. 35b). The results show that PLB is more

inhibitory in the presence of anionic lipids PS and PG, and less inhibitory in the presence

of cationic lipids EPC and TAP. Previous results showed that PLB phosphorylation,

which decreases inhibition of SERCA, increases the population in the dynamically
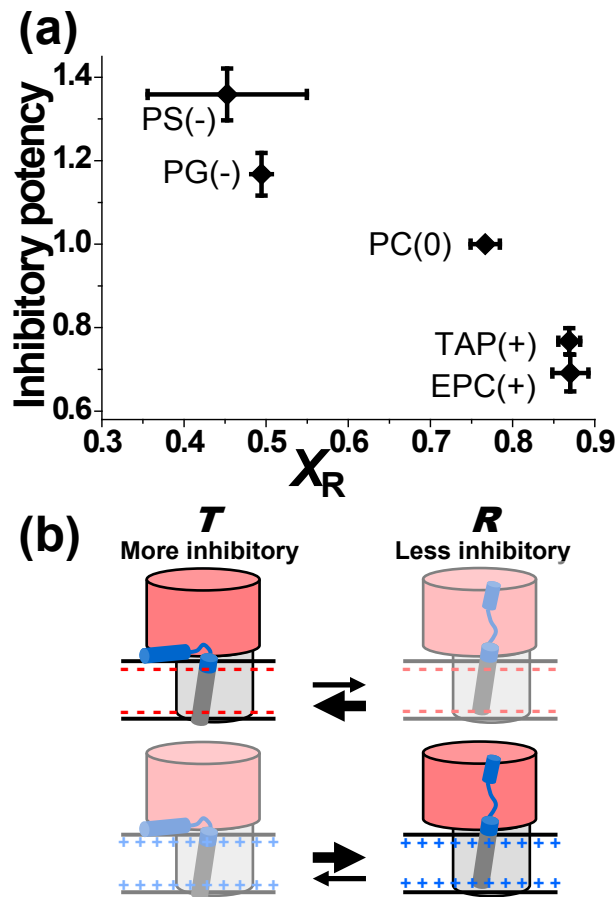
Fig. 36. Correlation of inhibitory potency with the *T/R* equilibrium. (a) As the fraction of SERCA-PLB complex in the *R* state (x_R) increases, in response to increasing membrane surface charge, the inhibitory potency of PLB (defined in Fig. 35) decreases. (b) Model consistent with the data. Both *T* and *R* states bind to SERCA. The membrane-associated *T* state is more inhibitory than the extended *R* state. Negative surface charge shifts the equilibrium toward *T*, increasing inhibition (top), while positive surface charge does the opposite (bottom).

disordered R state [32]. The results of Fig. 35b show that membrane surface charge modulates PLB's effect on SERCA by an analogous mechanism, confirming the conclusion above that the R state corresponds to the structural state having the shorter interprobe distance (population 1 in Fig. 33 and Fig. 34).

4.4 Discussion

Bimodal structure of the SERCA-PLB complex resolved by TR-FRET. Using EPR, we demonstrated that anionic lipids attract the cationic cytoplasmic domain of PLB to the membrane surface and thus increase the population of the membrane-associated T state, while cationic lipids do the opposite, increasing the R state population (Fig. 31). We then used TR-FRET to resolve two distinct structural states of the bound SERCA-PLB complex (Fig. 33) and observed a similar effect, with the R state assigned to the population having the shorter interprobe distance (Fig. 34). Membrane surface charge shifts the equilibrium between the T/R states with little or no effect on the two structural states themselves (Fig. 34d). This supports a model in which the cytoplasmic domain of the SERCA-bound T state is membrane associated, while that of the SERCA-bound R state loses contact with the membrane surface and contacts the SERCA cytoplasmic domain (Fig. 33c).

Mechanism of SERCA regulation. As we systematically varied the membrane surface charge, we observed a strong correlation between the population of the R state and PLB inhibitory function (Fig. 36a). This finding is consistent with previous results showing that phosphorylation of PLB, which decreases SERCA inhibition, also increases x_R [32], as do some loss-of-inhibition mutations in PLB [33]. In the current study, we show that

73

varying the membrane surface charge serves not only to relieve inhibition (positive charge increases x_R), but also to increase inhibition (negative charge decreases x_R). Thus we obtain convincing evidence that this correlation between structural dynamics and function holds even in the absence of PLB covalent modification (e.g., phosphorylation or mutation): it is primarily the T/R equilibrium that determines SERCA function (Fig. 36b).

Structural dynamics, not SERCA affinity, determines the inhibitory potency of PLB. TR-FRET clearly resolves free SERCA from the bound SERCA-PLB complex (Fig. 33c), and shows that relief of inhibition does not arise from a change in X_b, the fraction of SERCA bound to PLB (Fig. 34d). In both neutral (PC) or anionic lipids (PS, PG) (Fig. 34b), 80% of the SERCA is bound to PLB ($X_b \sim 0.8$), but PLB is more inhibitory in anionic lipids (Fig. 35b). Cationic lipids (EPC and TAP) actually increase slightly the fraction of SERCA bound to PLB ($X_b \sim 0.9$, Fig. 34b), but PLB inhibitory function decreases (Fig. 35b). This is opposite from the effect expected if relief of inhibition were due to dissociation of the complex. Therefore, the functional effects are due to structural changes within the bound SERCA-PLB complex (Fig. 36b), not to changes in SERCA-PLB affinity. It has been shown that the transmembrane helix of PLB without the cytoplasmic domain is sufficient to inhibit SERCA activity [77], so the role of the cytoplasmic domain is to relieve this inhibition when it is in the R state. Future studies must investigate how the dynamic disorder of the R state propagates allosterically to the transmembrane domain, interrupting the inhibitory interaction of the transmembrane domain with SERCA. This will have important implications for therapeutic engineering in this system, since it offers the hope of designing mutant

proteins or drugs that stabilize the non-inhibitory **R** state and thus relieve SERCA inhibition, without the need to dissociate PLB from SERCA [33, 58].

Relationship to previous work. The fraction x_R is much greater when PLB is bound to SERCA (Fig. 33, Fig. 34c) than when it is free (Fig. 32); this is consistent with previous studies by EPR [28, 32] and crosslinking [34], all of which suggest that SERCA decreases PLB's interaction with the membrane surface. This is presumably due in part to the negative charge of the SERCA cytoplasmic domain (indicated by red color in Fig. 33c and Fig. 36b), which attracts the positively charged PLB cytoplasmic domain. Thus a negatively charged membrane surface competes most effectively for PLB binding (Fig. 34c). Previous NMR results suggested that several residues around Lys3 on PLB are in contact with SERCA [120]. NMR also provides more detailed structural insight into the interactions between PLB and the membrane surface, involving both hydrophobic and hydrophilic side chains [30, 31]. Previous NMR results showed that the anionic PG increases the population of the restricted **T** state of PLB in the absence of SERCA [31], consistent with the EPR results here (Fig. 32).

Implications for SERCA regulation in native SR. The primary purpose of our manipulation of the lipid environment in this study was to perturb the structural and functional dynamics of SERCA-PLB through a mechanism distinct from PLB phosphorylation. However, it is also important to ask how these results relate to conditions in native cardiac SR. Our lipid headgroup composition is similar to that of cardiac SR, where PC is predominant (53%), followed by PE (27%) and PS (10%) [128]. However, most (76%) of the negatively charged PS headgroups face the lumen [128], so it is unlikely that they interact significantly with the cytosolic domain of PLB. Thus,

75

since virtually all of the lipids facing the cytosol are neutral, it is likely that the conditions in cardiac SR are best mimicked by our sample in which all lipids are neutral, where 77% of the SERCA-PLB complex is in the less inhibitory R state (Fig. 36a). These results suggest that in cardiac SR, a minor population of PLB in the T state is enough to inhibit SERCA substantially. At first glance, this seems surprising, but it means that phosphorylation of PLB need only shift about 23% of PLB to the R state to maximally activate SERCA. This is analogous to the poised equilibrium in the regulatory light chain of smooth muscle myosin, where phosphorylation causes just a 22% shift in the dynamic structural equilibrium but results in profound activation [122].

Lipid headgroup charge as a research tool to tune the structural and functional dynamics of integral membrane proteins. It has been an effective strategy to vary the physical properties of the hydrophobic core of the membrane, such as the hydrophobic thickness and fluidity [108, 129], to investigate the structural and functional dynamics of integral membrane proteins. The composition of lipid headgroups is also critical for the function of membrane proteins [115], including SERCA [123, 130]. Researchers have varied the zwitterionic and anionic lipid compositions to mimic native membrane environments [131, 132]. Cationic lipids, on the other hand, do not occur naturally and have been used primarily as tools in liposomal transfection [133] and lipid transfer [134]. The present study introduces them as agents to perturb the structure and function of membrane proteins. Using lipids with anionic, zwitterionic, and cationic headgroups, we controlled the surface electrostatics and tuned successfully the structural dynamics of an integral membrane protein complex. Compared to altering the protein structure through direct chemical modifications such as mutagenesis, phosphorylation, lipidation,

76

methylation, and crosslinking, this method preserves the chemical integrity of the proteins involved. Although the present study focuses on charge variation, it is clear from the data that charge is not the only headgroup property that affects structural dynamics and function in the SERCA-PLB system – the two anionic lipids do not cause identical effects; neither do the two cationic lipids. Nevertheless, despite substantial variation in headgroup size and shape, the correlations of structure and function with charge are clear (Fig. 36).

4.5   Materials and Methods

Sample preparation and assays. SERCA was purified from rabbit skeletal muscle using reactive red in 0.1% octaethylene glycol monododecyl ether ($C_{12}E_8$) [36]. Purified SERCA was labeled with AEDANS as previously described [36] and flash frozen in sucrose buffer (300 mM sucrose, 20 mM 3-(N-morpholino) propanesulfonic acid (MOPS), pH 7.0, 4 °C). The dye-to-protein ratio was determined by measuring the absorbance at 334 nm ($\varepsilon = 6100$ M^{-1} cm^{-1}) in a denaturing buffer (0.1 M NaOH, 1% sodium dodecyl sulfate). Solid-phase peptide synthesis and HPLC purification were used to prepare AFA-PLB, as previously reported [29, 32]. Fluorescence Labeling at the N-terminus was accomplished by incorporation of Fmoc-Lys(Dabcyl)-OH during peptide synthesis. Fmoc-TOAC-OH (2,2,6,6-tetramethylpiperidine-1oxyl-4-amino-4-carboxylic acid) was incorporated in the AFA-PLB sequence at position 11, as previously reported [78]. Characterization was accomplished by mass spectrometry (MALDI-TOF) and Edman protein sequencing. PLB concentrations were measured with the BCA assay (Pierce) and by amino acid analysis. Functional reconstitution of SERCA and/or PLB was performed as described previously [32, 135], adapted for systematic variation of lipid

77

composition. The final molar ratio of SERCA/PLB/lipid was 1/10/700, with either one or both proteins present. The molar lipid composition was PC/PE/L = 4/1/1, where L = PS (−), PG (−), PC (0), EPC (+) and TAP (+).

Ca-ATPase activity was measured at 25 °C as a function of pCa using an enzyme-linked ATPase assay in a microplate reader [36]. The data were fitted by

$$V = \frac{V_{max}}{1 + 10^{-n(pK_{Ca} - p_{Ca})}} \qquad \text{Eq. 7}$$

where V_{max} is the maximum ATPase rate, pK_{Ca} is the apparent Ca affinity, and n is the Hill coefficient. The inhibitory potency of PLB was defined as the decrease in the apparent Ca^{2+} affinity of SERCA:

$$\Delta pK_{Ca} = pK_{Ca}(-PLB) - pK_{Ca}(+PLB) \qquad \text{Eq. 8}$$

EPR spectroscopy. EPR spectra were acquired with a Bruker EleXsys E500 spectrometer equipped with a 4122 SHQ cavity. A quartz dewar and Bruker N_2 temperature controller were used to maintain the samples at 25 ± 0.1 °C. Spectra were acquired using 12.6 mW microwave power, 100 kHz modulation frequency with 1 G peak-to-peak amplitude, and a 120 G sweep width. Mole fractions of populations, resolved by rotational dynamics, were determined by fitting the spectra to numerical simulations [32].

FRET spectroscopy. Fluorescence waveforms were acquired using a high-performance time-resolved fluorescence (HPTRF) spectrometer constructed in this laboratory [125], which uses direct waveform recording (DWR) rather than the conventional method of time-correlated single-photon counting (TCSPC). As shown previously, when identical samples are studied, this DWR instrument offers 105 times higher throughput than

TCSPC, while providing at least comparable performance in signal/noise, accuracy, and resolution of distinct components [125]. AEDANS-SERCA was excited using a passively Q-switched microchip YAG laser (NanoUV-355; JDS Uniphase), at 355 nm with a pulse repetition frequency of 10 kHz. The high energy (1 mJ / pulse) narrow (~ 1 ns full width at half maximum) laser pulses are highly uniform in shape and intensity. Emitted photons pass through a polarizer set to the magic angle (54.7 °), followed by an interference bandpass filter (Semrock 470/22 nm), detection with a photomultiplier tube (PMT) module (H5773-20, Hamamatsu), and digitization (Acqiris DC252, time resolution 0.125 ns). TR-FRET waveforms were analyzed as described previously [122] and described in SI. For all FRET samples analyzed, two Gaussian distance distributions were necessary and sufficient to fit the data (Fig. S38).

4.6 Supplementary Information

TR-FRET data analysis. Fluorescence waveforms were analyzed using a non-linear least-squares fitting as described previously [122, 136]. The observed donor-only waveform $F_{Dobs}(t)$ was fitted by a simulation $F_{Dsim}(t)$, consisting of a multiexponential decay $F_D(t)$ convolved with the instrument response function $IRF(t)$ (Fig. 33a, acquired from light scattering).

$$F_D(t) = \sum_{i=1}^{n} A_i \exp(-t/\tau_{Di}) \, ,$$

Eq. S9

$$F_{Dsim}(t) = \int_{-\infty}^{+\infty} IRF(t\text{-}t') \, F_D(t') \, dt',$$

where τ_{Di} are the donor-only fluorescence lifetimes. The ensemble-average lifetime is given by:

$$\langle \tau_D \rangle = \sum_{i=1}^{n} A_i \, \tau_{Di} \Big/ \sum_{i=1}^{n} A_i \qquad\qquad \text{Eq. S10}$$

The observed donor + acceptor waveform $F_{D+Aobs}(t)$ was sometimes fitted to a multiexponential function using the same approach. The ensemble-average FRET efficiency, which is equivalent to the result of a steady-state fluorescence measurement [127], is given by:

$$\langle E_{D+A} \rangle = 1 - \langle \tau_{D+A} \rangle / \langle \tau_D \rangle . \qquad\qquad \text{Eq. S11}$$

To resolve structural states, a distribution of donor-acceptor distances $\rho(r)$ was assumed:

$$F_{DA}(t) = \int_{-\infty}^{+\infty} \rho(R) \cdot \sum_{i=1}^{n} A_i \exp[(-t/\tau_{Di})(1+[R_{0i}/R]^6)]dR, \qquad\qquad \text{Eq. S12}$$

where R_{0i} is the lifetime-weighted Förster distance [122] (in Å):

$$R_{0i}^6 = 9780^6 J \kappa^2 \, n^{-4} k_{rad} \tau_{Di} \qquad\qquad \text{Eq. S13}$$

where J is the overlap integral between the donor emission and acceptor absorption spectra, n is the refractive index (1.4), κ^2 is the orientation factor (2/3, assuming random orientation), and k_{rad} is the radiative decay rate for the donor. The value of k_{rad}, which is assumed to be invariant for each donor, is the ratio of the quantum yield Q_D over the average lifetime of the donor $\langle \tau_D \rangle$ (Eq. S10) and was measured previously to be 0.0257 ns^{-1} for AEDANS [122]. Eq. S13 follows directly from the Förster theory's assumption

[122, 137] that the energy transfer rate constant k_T (= $R_{0i}{}^6 R^{-6}/\tau_{Di}$) depends on the donor-acceptor distance R but not on the donor-only lifetime τ_{Di}. Here we also assume that the orientation factor κ^2 does not change from one structural state to another, but this is justified by low fluorescence anisotropy values that were observed. R_0 between AEDANS-SERCA and Dabcyl-PLB is 3.2 nm [36].

The distance distribution $\rho(r)$ (Eq. S12) was assumed to be a sum of n Gaussian components, each corresponding to a structural state of the SERCA-PLB complex, with its central distances R_j, widths $FWHM_j$, and mole fractions x_j

$$\rho(R) = \sum_{j=1}^{n} x_j \, \sigma_j^{-1} (2\pi)^{-1/2} \exp(-[(R-R_j)/(2\sigma_j)]^2, \; \sigma_j = FWHM_j/[2*(2 \ln 2)^{1/2}],$$

Eq. S14

$$\sum_{j=1}^{n} x_j = 1.$$

The observed waveform $F_{D+Aobs}(t)$ was fitted by $F_{D+Asim}(t)$:

$$F_{D+A}(t) = (1 - X_b)F_D(t) + X_b F_{DA}(t),$$

Eq. S15

$$F_{D+Asim}(t) = \int_{-\infty}^{+\infty} IRF(t - t') \cdot F_{D+A}(t')dt',$$

where X_b is the fraction of donor-labeled SERCA bound to and transferring energy to acceptor-labeled PLB. Thus binding (X_b) is determined independently of the mole fractions of resolved structural states (x_j in Eq. S14).

Donor-only fluorescence decays are best fit with 3 exponential components. The donor-only fluorescence decay $F_D(t)$ (Fig. S37a), was fitted with a multiexponential function (Eq. S9), with the result that three lifetime components are

necessary and sufficient to fit the data (Eq. S9, $n = 3$), based on the residual plots (data – fit, Fig. S37b) and the χ^2 values (sum of residuals at each data point, Fig. S37c). The results show clearly that the fit is improved by increasing n from 2 to 3, but not by increasing n from 3 to 4. The fitting results are summarized in Table S3. The donor-only fluorescence lifetime is not sensitive to the lipid environment (Table S4), presumably because the labeling site (Cys 674) is elevated far from the membrane surface. Therefore, to increase precision in the FRET analysis, the three donor lifetime values were globally linked. The corresponding R_{0i} (Eq. S13) values are listed in Table S4.
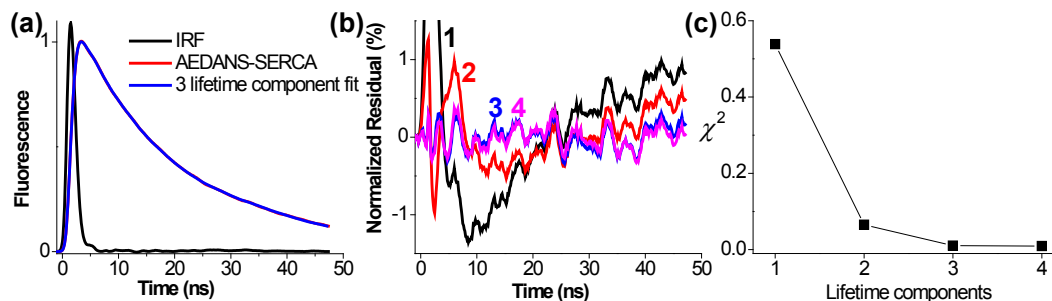
Fig. S37. Fluorescence lifetime fit of IAEDANS-labeled SERCA. (a) Fluorescence data, fit and instrument respond function. (b) normalized residual plots ((data – fit) / max fit value) of fits with increasing number of lifetime components (Eq. S9, *n* = 1-4).

Table S**3**. Fluorescence lifetime of AEDANS-SERCA in charged lipid vesicles, analyzed using Eq. S9 and Eq. S10 (mean ± SEM, N= 4).

Lipid (charge)	A_1	τ_1	A_2	τ_2	A_3	τ_3	$\langle \tau \rangle$
PS (-)	0.418 ± 0.016	0.112 ± 0.009	0.055 ± 0.004	4.96 ± 0.85	0.527 ± 0.018	18.9 ± 0.1	10.3 ± 0.3
PG (-)	0.412 ± 0.015	0.134 ± 0.017	0.055 ± 0.003	5.36 ± 0.46	0.532 ± 0.015	18.9 ± 0.1	10.4 ± 0.3
PC (0)	0.403 ± 0.009	0.13 ± 0.013	0.054 ± 0.001	5.27 ± 0.39	0.544 ± 0.009	18.9 ± 0.1	10.6 ± 0.2
EPC (+)	0.415 ± 0.01	0.124 ± 0.01	0.059 ± 0.002	4.88 ± 0.53	0.526 ± 0.011	18.8 ± 0.1	10.2 ± 0.2
TAP (+)	0.392 ± 0.013	0.134 ± 0.002	0.056 ± 0.003	4.37 ± 0.42	0.551 ± 0.01	18.8 ± 0.1	10.7 ± 0.2

Table S**4**. The three fluorescence lifetimes of AEDANS-SERCA were globally linked for all samples, and the three R_{0i} values were calculated using Eq. S14 (mean ± SEM, N= 4).

	A_i	τ_i	R_{0i}
1	0.407 ± 0.09	0.122 ± 0.012	15.2 ± 0.3
2	0.052 ± 0.001	4.32 ± 0.25	27.6 ± 0.2
3	0.541 ± 0.01	18.7 ± 0.1	35.3 ± 0.1

Two structural states are necessary and sufficient to fit the TR-FRET data. To resolve structural states within the SERCA-PLB complex, we used $F_D(t)$ as input (Table S4), to fit $F_{D+Aobs}(t)$ and determine the interprobe distance distribution (Eq. S12 – Eq. S15). We tested models with one, two, and three Gaussian components (Eq. S14, $n = 1, 2$, and 3). The goodness of fit was evaluated to minimize χ^2 (Fig. S38). The fit was consistently improved by increasing the distance components (n in Eq. S14) from 1 to 2, but not from 2 to 3 (Fig. S38). Thus two Gaussian distance distributions are necessary and sufficient to fit the TR-FRET data, and we conclude that the SERCA-PLB complex adopts two distinct structural states. The results are summarized in Fig. 33 and Fig. 34. We also fit the data with a model-independent multiexponential function as in Eq. S9, and found that a three-exponential function (Eq. S9, $n = 3$) gave as good a fit as the double-Gaussian (Eq. S14, $n = 2$). However, this fit did not allow us to quantitate binding from structural changes, nor did it provide a realistic physical view of this dynamic protein complex. This same two-Gaussian analysis was successfully applied previously to similar FRET data from smooth muscle myosin regulatory light chain [122] and the myosin relay helix [138], generating high-resolution structural information that was confirmed by independent molecular dynamics simulations [122] or by dipolar electron–electron resonance (DEER) EPR spectroscopy [138].
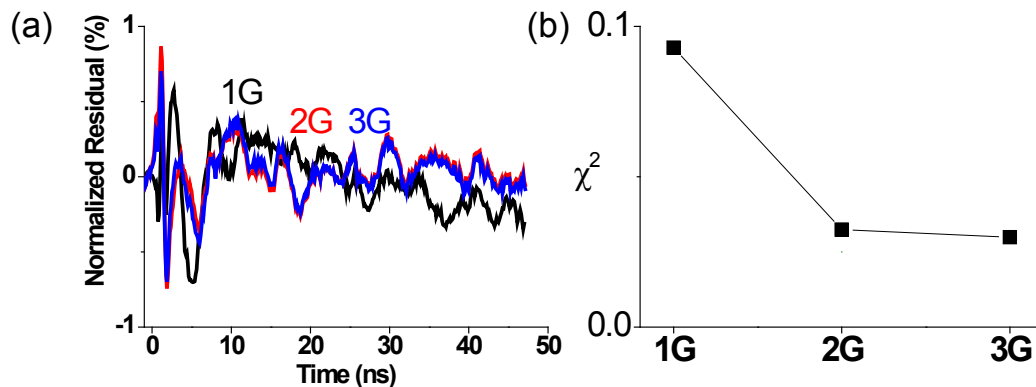
Fig. S38. Time-resolved FRET resolves two structural states of the SERCA-PLB complex in zwitterionic lipid vesicles. Examples of the fluorescence waveforms of AEDANS-SERCA only (D) or co-reconstituted with Dabcyl-AFA (D+A) are in (Fig. 3*A*). The instrument-response function (IRF in Fig. 33a) was convolved with simulated decays (Eq. S12 - Eq. S15), then fitted to the experimental waveforms. (a) normalized residual plots show that 2G (Eq. S14, n = 2) is better than 1G, while 3G doesn't improve the fit. (b) The χ^2 values confirm that the 2G model is necessary and sufficient to fit the data.

Support-Plane Analysis. We analyzed the χ^2 surface to estimate the uncertainty of the fitting parameters (Fig. S39). To generate the χ^2 surface, the parameter of interest is fixed (x-axis), and all other parameters are allowed to vary to minimize χ^2 (y-axis). The red bar represents 67% confidence level. Thus the uncertainties are ± 0.01 nm for R_1 and R_2, ± 0.015 nm for $FWHM_1$, and ± 0.075 nm for $FWHM_2$. These uncertainties were typically comparable to or less than those obtained from the standard deviations of multiple experiments (Fig. 34). Uncertainties in widths $FWHM_i$ are typically greater than those of the center distances R_i (Fig. S39), and the same trend is seen in the error bars (SEM values) from multiple experiments (Fig. 34).
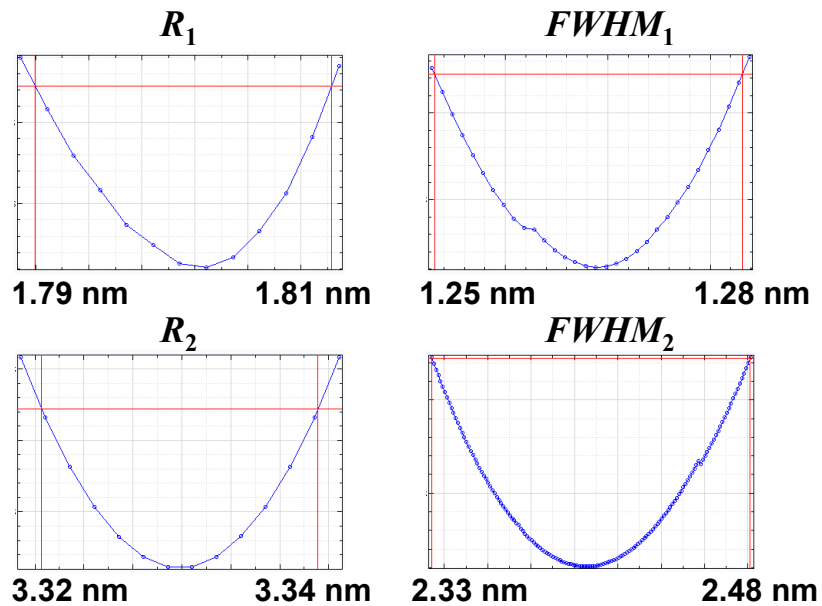
Fig. S39. Uncertainty of fitting parameters estimated by χ^2 surface ("support-plane") analysis. This example is in PS vesicles. The intersection between the horizontal red line and the blue χ^2 surface represents 67% confidence level.

Chapter 5 – Phosphorylation Alters the Transmembrane Binding Interface between SERCA and PLB

5.1 Introduction

Chapters 3 and 4 summarize spectroscopic data supporting an alternative model of SERCA-PLB regulation, where PLB acts as a SERCA subunit that transitions between an inhibitory *T* state and a non-inhibitory *R* state to modulate SERCA function. What remains unclear, however, is the structural basis for inhibition relief. Since the inhibitory transmembrane helix of PLB apparently remains associated with SERCA following Ser16 phosphorylation (and the consequent *T*-to-*R* transition), it seems plausible that the helix would undergo a conformational change (e.g., vertical shift, rotation) between the *T* and *R* states that disrupts its inhibitory interactions with SERCA (Fig. 40). To test this hypothesis, we separately spin-labeled PLB at two transmembrane sites (Fig. 41), and performed conventional and accessibility EPR measurements to elucidate the structural
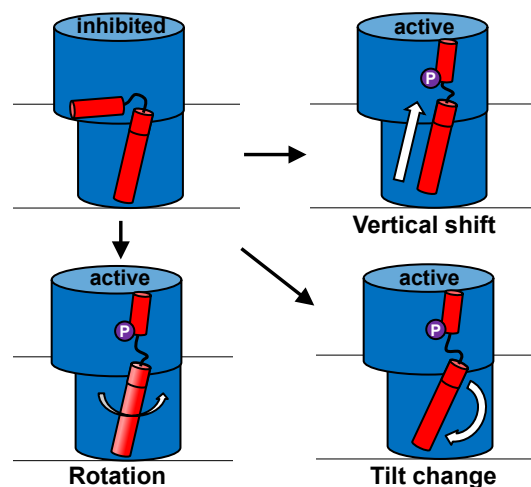
Fig. 40. Potential PLB conformational changes induced by Ser16 phosphorylation. The *T*-to-*R* transition, induced by Ser16 phosphorylation, may relieve inhibition by altering the conformation of PLB's transmembrane helix within the regulatory complex, breaking its inhibitory interactions with SERCA.

changes induced by phosphorylation. Accessibility EPR quantifies collisional exchange between excited labels and paramagnetic relaxation agents (PRAs, see section 2.6), which depends directly on the PRA's accessibility to the spin label. Accessibility measurements have proven exceptionally useful in detecting the structural transitions of membrane proteins [139, 140]. In particular, the collision gradient method developed by the Hubbell lab [46] compares the relative accessibilities of membrane-embedded spin labels to hydrophobic (O_2) and hydrophilic (NiEDDA) PRAs in order to estimate their position relative to the bilayer. Here, we chose to label sites Q29 and A36 (on the monomeric AFA-PLB background) by separately mutating each to a cysteine (Q29C and A36C) and reacting them with the maleimide spin label (Fig. 9). These sites were chosen to be maximally sensitive to changes in the membrane insertion depth or tilt of PLB's transmembrane helix (Fig. 41). Position 36 is predicted to reside near the center of the bilayer, and thus should be particularly sensitive to changes in O_2 accessibility upon SERCA binding and following any conformational changes induced by phosphorylation. In contrast, position 29 is expected to lie in the interfacial region of the bilayer prior to SERCA binding (i.e., have comparable O_2 and NiEDDA accessibilities), and transition to a more water-exposed position in the regulatory complex (Fig. 41), with phosphorylation-induced conformational changes possibly restoring it to the bilayer interior. For both sites, steric hindrance of spin label motion through interactions with SERCA (e.g., following rotation of the helix) should be evident from changes to the conventional EPR spectra.
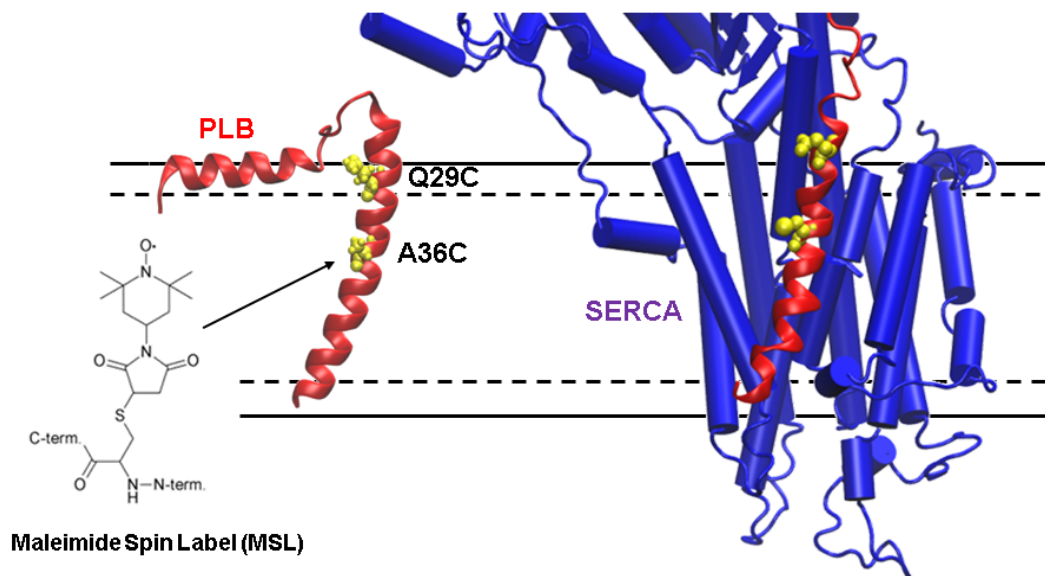
Fig. 41. Positions of labeling sites Q29C and A36C. (left) PLB shown with spin-labeling sites Q29C and A36C rendered in space-filling yellow, modeled from hybrid NMR structure of PLB published by Traaseth et al. [19]. (right) Model of the regulatory complex [34] with spin-labeling sites rendered as on the left.

5.2 Materials and Methods

Protein expression and purification. Phospholamban mutants were expressed as fusions to maltose binding protein [141, 142], with cysteines introduced by QuikChange mutagenesis using primers ordered from University of Minnesota Biomedical Genomics Center. BL21(DE3) cells (Lucigen) transformed with the constructs were grown at 37 °C in Terrific Broth containing 100 μg/mL carbenicillin until OD_{600} reached ~2, then moved to room-temperature and incubated until OD_{600} reached 2.5 – 3 before induction with 500 μM IPTG. Induced cultures were incubated 22 – 24 hr at room-temperature and harvested by centrifugation.

PLBs were purified by amylose resin chromatography (New England BioLabs) and high-performance liquid chromatography (HPLC) essentially as described by Veglia et

88

al. [143]. Purified, lyophilized proteins were dissolved to ~100 μM in PLB labeling buffer (50 mM MOPS, 5% (w/v) SDS, 200 μM TCEP, pH 7.0) and incubated 1 hr at room-temperature before addition of 1 mM 4-maleimido-2,2,6,6-tetramethylpiperidine-1-oxyl (maleimide spin label, or MSL) from a 50 mM stock in dimethylformamide. Samples were protected from light and gently mixed overnight at room-temperature before a second round of HPLC purification and lyophilization. Spin-labeling efficiency was determined by electrospray ionization mass spectrometry and comparison of the EPR signal intensity to a 100 μM TEMPO standard, and found to be ≥ 95% in all cases. Spin-labeled PLB powders were dissolved to ~2 mg/mL in trifluoroethanol, quantified using a bicinchoninic acid (BCA) assay (Thermo Fisher Scientific), and stored at -20 °C.

Sample preparation. For EPR measurements, spin-labeled PLBs and reactive-red purified SERCA [80] were co-reconstituted into 4:1 (mol/mol) DOPC/DOPE vesicles at 700:1:1 (mol/mol) lipids/PLB/SERCA as described previously [81]. Samples were prepared in duplicate, with one set receiving 50 mM NiEDDA from a 200 mM stock in 20 mM MOPS, pH 7.0 (NiEDDA prepared according to Oh et al. [47]), and the second set serving as a control.

EPR spectroscopy and data analysis. EPR experiments were performed on a Bruker EleXsys E500 spectrometer equipped with an ER 4123D resonator and a gas-flow temperature controller. Samples were loaded into gas-permeable, 0.6 mm inner-diameter TPX capillaries (Molecular Specialties) and incubated in the resonator at 295 K under a continuous flow of nitrogen gas (control and NiEDDA measurements) or zero-grade air (O_2 measurements) beginning at least 15 min prior to (and continuing throughout) the EPR measurement.

Conventional EPR spectra were acquired at non-saturating microwave power (0.5 mW) using a 120 G sweep width, 100 kHz modulation frequency, and 1 G modulation amplitude. Progressive saturation measurements were made by sweeping 20 G over the central peak, using the above modulation settings, while varying the microwave attenuation between 43 dB and 1 dB in 3-dB increments. Receiver gain and acquisition time (number of scans) were optimized at each attenuation level to give comparable signal/noise for each spectrum. Central peak amplitudes were measured from the progressive saturation spectra using WACY, an in-house program developed by Edmund Howard. Data were plotted and fit to Eq. 5 [47] in Origin 8.6 to extract $P_{1/2}$ values, then normalized and plotted on a logarithmic scale to emphasize $\Delta P_{1/2}$ (the $P_{1/2}$ difference between samples containing and lacking the PRA). Using the extracted $P_{1/2}$ values, the accessibility parameter φ was calculated according to Eq. 6.

$$A = I\left[1 + (2^{1/\varepsilon} - 1)\frac{P}{P_{1/2}}\right]^{-\varepsilon} \qquad \text{Eq. 5}$$

$$\varphi = ln\frac{\Delta P_{1/2}(O_2)}{\Delta P_{1/2}(NiEDDA)} \qquad \text{Eq. 6}$$

5.3 Results and Discussion

EPR measurements at position 36. AFA-PLB mutant A36C was reacted with MSL (hereafter called MSL-A36C-PLB) and reconstituted alone or with equimolar SERCA, both with and without Ser16 phosphorylation by protein kinase A (PKA). Conventional EPR measurements found no substantial change in ps – ns mobility of MSL-A36C-PLB

upon SERCA binding and/or phosphorylation, indicating that the label is not hindered upon PLB association with the ATPase. All four conventional EPR measurements (± SERCA, ± Ser16 phosphorylation) reported highly-immobilized spectra typical for spin labels attached to surface-exposed transmembrane helices (Fig. 42) [144].
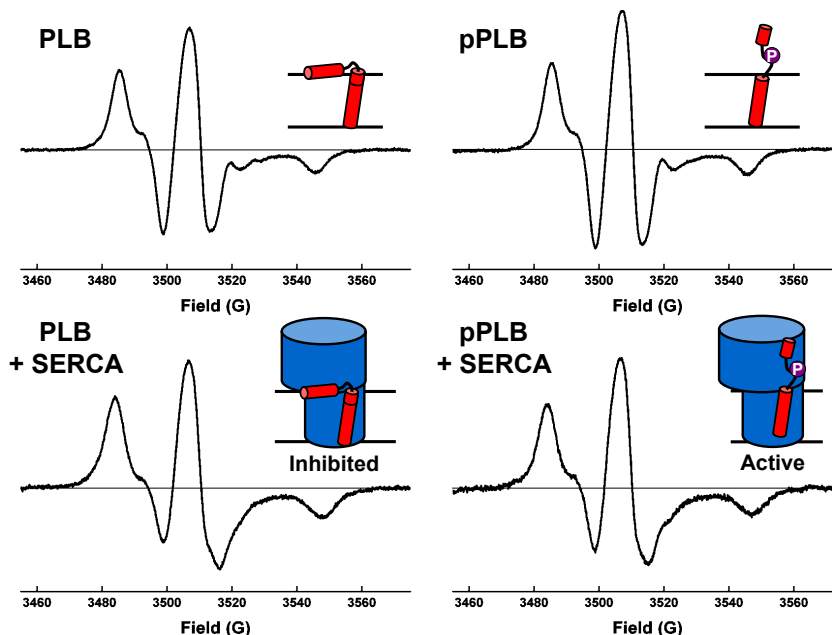
Fig. 42. Conventional EPR spectra of MSL-A36C-PLB. Conventional EPR detects negligible changes in MSL-A36C-PLB mobility upon phosphorylation (purple circle), as seen by comparing the upper left and upper right spectra. SERCA binding only slightly immobilizes both PLB (lower left) and phosphorylated PLB (lower right), in agreement with the outward-facing orientation of position 36 predicted by the accepted regulatory model (Fig. 41, right)

In contrast to the largely invariant conventional EPR spectra (Fig. 42), progressive saturation EPR (Fig. 43a) of MSL-A36C-PLB revealed significant changes in PRA accessibility upon SERCA binding. As predicted, position 36 was much more accessible to O_2 than to NiEDDA, as seen by comparing $\Delta P_{1/2}(O_2)$ versus $\Delta P_{1/2}(NiEDDA)$ for PLB in Fig. 43b, reflecting its position deep in the acyl region of the bilayer. While phosphorylation alone had no effect on PRA accessibility (Fig. 43b, pPLB), the addition of SERCA caused accessibility to both O_2 and NiEDDA to decrease significantly.

Together with the conventional EPR spectra in Fig. 42, our accessibility results for MSL-A36C-PLB suggest that position 36 becomes 'loosely occluded' within the regulatory complex, allowing for restricted probe motion while still protecting the label from collisional exchange. Notably, a concerted change in A36C accessibility was observed upon phosphorylation of SERCA-bound PLB (pPLB + SERCA, Fig. 43b), with O_2 accessibility increasing as NiEDDA accessibility decreased. These changes are reflected in φ, which returns to nearly the same level as in the absence of SERCA (Fig. 43b), though the low $\Delta P_{1/2}$ values for both O_2 and NiEDDA accessibility measurements indicate that phosphorylated MSL-A36C-PLB remains associated with SERCA and protected from collisional exchange.
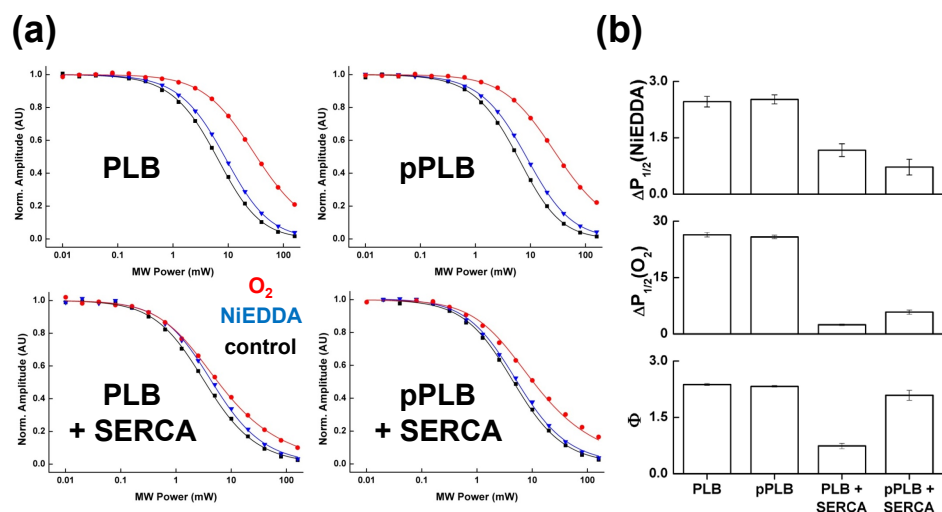
Fig. 43. Progressive saturation measurements of MSL-A36C-PLB. (a) Normalized progressive saturation EPR data for MSL-A36C-PLB samples reconstituted alone or with equimolar SERCA, and omitting (PLB, PLB + SERCA) or including (pPLB, pPLB + SERCA) PKA. (b) $\Delta P_{1/2}$ values determined by fitting data in (a) to Eq. 5, with φ calculated using Eq. 6.

EPR measurements from position 29. Based on the hybrid NMR structure of monomeric PLB [19], position Q29 is expected to lie within the interfacial region of the lipid bilayer for PLB alone (Fig. 41), while the current model of the regulatory complex
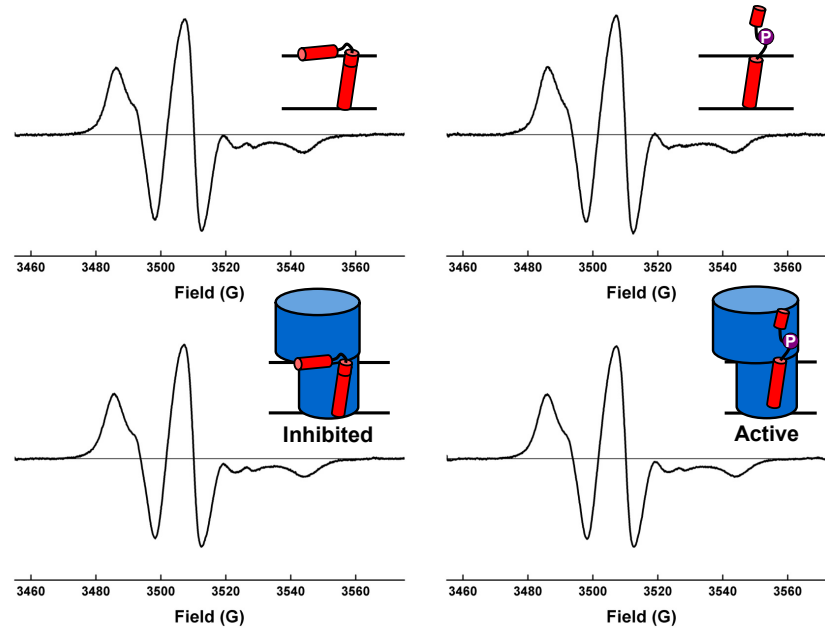
Fig. 44. Conventional EPR spectra of MSL-Q29C-PLB. Essentially no change in the mobility of MSL-Q29C-PLB is observed with phosphorylation and/or SERCA binding, indicating that this position remains quite exposed in the regulatory complex, also explaining the lack of accessibility changes observed in Fig. 45.

places residue 29 in the cytoplasm [34]. Thus spin-labeled Q29C (MSL-Q29C-PLB) should be particularly sensitive to changes in PLB bilayer immersion depth, as it is predicted to occupy different environments (i.e., lipid headgroup region versus the aqueous phase) depending on its association with SERCA. Compared to position 36, conventional EPR of reconstituted MSL-Q29C-PLB detected even less change to probe mobility upon SERCA binding and/or phosphorylation, with all samples yielding a moderately immobilized spectra (Fig. 44). Furthermore, in all cases (± SERCA, ± phosphorylation) MSL-Q29C-PLB shows comparable accessibilities to both O_2 and NiEDDA (Fig. 45a,b), placing it near the surface of the bilayer. Our accessibility results suggest that position 29 maintains a relatively static position within the membrane regardless of its phosphorylation state or association with SERCA.
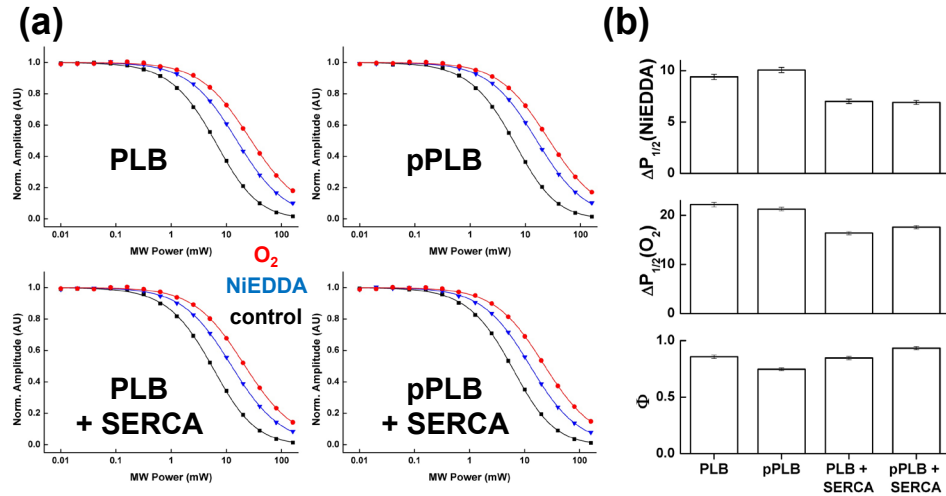
Fig. 45. Progressive saturation measurements for MSL-Q29C-PLB. (a) Normalized progressive saturation EPR data for MSL-Q29C-PLB samples reconstituted alone or with equimolar SERCA, and omitting (PLB, PLB + SERCA) or including (pPLB, pPLB + SERCA) PKA. (b) $\Delta P_{1/2}$ values determined by fitting data in (a) to Eq. 5, with φ calculated using Eq. 6.

Together, our accessibility measurements at PLB positions 29 and 36 indicate a subtle change in the conformation of SERCA-bound domain II upon Ser16 phosphorylation. The increased hydrophobicity observed for position 36, paired with the invariance of position 29, suggest a change in the tilt of domain II with respect to SERCA, where position 29 serves as a pivot point while position 36 is carried deeper into the lipid bilayer (Fig. 46, left). An alternative possibility is a rotation of PLB's transmembrane helix, about its long axis, that increases the exposure of position 36 to the bilayer while maintaining the same overall PRA accessibility for position 29 (Fig. 46, right). Additional accessibility measurements at other sites along PLB's transmembrane helix will be necessary to validate these findings and fully characterize the conformational change induced by phosphorylation.
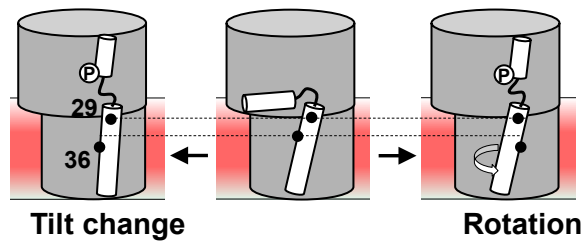
Fig. 46. Potential models for transmembrane helix conformational change induced by phosphorylation. The observed accessibility changes (or lack thereof) for MSL-Q29C-PLB and MSL-A36C-PLB may be explained in terms of a tilt change (left) or a helix rotation (right) that carries position 36 deeper into the bilayer while leaving position 29 unaffected.

Summary and Future Directions

Despite decades of study, the mechanism of SERCA regulation by PLB remains obscure, with different experimental approaches often leading to contradictory models. The results presented in this thesis help resolve some of these contradictions and offer a better understanding of phosphorylation-mediated inhibition relief. In Chapters $3 - 5$, we demonstrated that (1) the transmembrane domain of PLB remains bound to SERCA following Ser16 phosphorylation, (2) the T and R states of PLB correspond to different inhibitory conformations, with perturbation of the T/R equilibrium altering the functional state of SERCA, and (3) PLB's transmembrane helix likely undergoes a conformational change in response to Ser16 phosphorylation that disrupts its inhibitory interactions with SERCA. While these studies have resolved several questions regarding the mechanism of SERCA-PLB regulation, it leaves several questions unaddressed:

Coupling between domains Ia and II. The phosphorylation sites of PLB are located in domain Ia and are quite separated from domain II, the site of inhibitory interactions with SERCA. While the results presented here demonstrate that SERCA-PLB regulation likely follows the Subunit Model, they do not investigate the mechanism by which phosphorylation and the subsequent T-to-R transition are transmitted to domain II. Recent mutagenesis studies found that multiple glycine mutations to the loop region of PLB can effectively uncouple phosphorylation from inhibition relief [145], hinting at the importance of the loop and domain Ib in allosteric coupling between domains Ia and II.

The role of interactions between domain Ia and the N domain. Crosslinking studies have revealed interactions between PLB domain Ia and SERCA's N domain, with

mutations to either domain perturbing SERCA-PLB regulation. Lipid anchoring experiments have shown that domain Ia must be allowed to access the *R* state for phosphorylation to relieve inhibition, where the extended *R* state potentially reaches to the *N* domain for inhibition-relieving interactions. If this is the case, it is unclear why domain Ia must interact with the *N* domain to mediate inhibition relief, though the extended conformation of PLB necessary for these interactions may impart strain on the coupling between domain II and the SERCA's *TM* domain.

Bibliography

1.   Bers, D.M., *Cardiac excitation-contraction coupling.* Nature, 2002. **415**(6868): p. 198-205.

2.   Pieske, B., et al., *Ca2+ handling and sarcoplasmic reticulum Ca2+ content in isolated failing and nonfailing human myocardium.* Circ Res, 1999. **85**(1): p. 38-46.

3.   Arkin, I.T., et al., *Structural perspectives of phospholamban, a helical transmembrane pentamer.* Annu Rev Biophys Biomol Struct, 1997. **26**: p. 157-79.

4.   Simmerman, H.K. and L.R. Jones, *Phospholamban: protein structure, mechanism of action, and role in cardiac function.* Physiol Rev, 1998. **78**(4): p. 921-47.

5.   Wegener, A.D., et al., *Phospholamban phosphorylation in intact ventricles. Phosphorylation of serine 16 and threonine 17 in response to beta-adrenergic stimulation.* J Biol Chem, 1989. **264**(19): p. 11468-74.

6.   Kuhlbrandt, W., *Biology, structure and mechanism of P-type ATPases.* Nat Rev Mol Cell Biol, 2004. **5**(4): p. 282-95.

7.   Lytton, J., et al., *Functional comparisons between isoforms of the sarcoplasmic or endoplasmic reticulum family of calcium pumps.* J Biol Chem, 1992. **267**(20): p. 14483-9.

8.   Kimura, Y., et al., *Phospholamban regulates the Ca2+-ATPase through intramembrane interactions.* J Biol Chem, 1996. **271**(36): p. 21726-31.

9.   Ferrington, D.A., et al., *Comparable levels of Ca-ATPase inhibition by phospholamban in slow- twitch skeletal and cardiac sarcoplasmic reticulum.* Biochemistry, 2002. **41**(44): p. 13289-96.

10.   Ji, Y., et al., *SERCA1a can functionally substitute for SERCA2a in the heart.* Am J Physiol, 1999. **276**(1 Pt 2): p. H89-97.

11.   Lalli, M.J., et al., *Sarcoplasmic reticulum Ca(2+) atpase (SERCA) 1a structurally substitutes for SERCA2a in the cardiac sarcoplasmic reticulum and increases cardiac Ca(2+) handling capacity.* Circ Res, 2001. **89**(2): p. 160-7.

12.   Toyoshima, C. and H. Nomura, *Structural changes in the calcium pump accompanying the dissociation of calcium.* Nature, 2002. **418**(6898): p. 605-11.

13.   Humphrey, W., A. Dalke, and K. Schulten, *VMD: visual molecular dynamics.* J Mol Graph, 1996. **14**(1): p. 33-8, 27-8.

14.   Toyoshima, C. and G. Inesi, *Structural basis of ion pumping by Ca2+-ATPase of the sarcoplasmic reticulum.* Annu Rev Biochem, 2004. **73**: p. 269-92.

15.   Moller, J.V., et al., *The sarcoplasmic Ca2+-ATPase: design of a perfect chemi-osmotic pump.* Q Rev Biophys, 2010. **43**(4): p. 501-66.

16.   Toyoshima, C., et al., *Crystal structure of the calcium pump of sarcoplasmic reticulum at 2.6 A resolution.* Nature, 2000. **405**(6787): p. 647-55.

17.   Winters, D.L., et al., *Interdomain fluorescence resonance energy transfer in SERCA probed by cyan-fluorescent protein fused to the actuator domain.* Biochemistry, 2008. **47**(14): p. 4246-56.

18.   Metcalfe, E.E., et al., *1H/15N Heteronuclear NMR spectroscopy shows four dynamic domains for phospholamban reconstituted in dodecylphosphocholine micelles.* Biophys J, 2004. **87**(2): p. 1205-14.

19.   Traaseth, N.J., et al., *Structure and topology of monomeric phospholamban in lipid membranes determined by a hybrid solution and solid-state NMR approach.* Proc Natl Acad Sci U S A, 2009. **106**(25): p. 10165-70.

20.   Wegener, A.D. and L.R. Jones, *Phosphorylation-induced mobility shift in phospholamban in sodium dodecyl sulfate-polyacrylamide gels. Evidence for a protein structure consisting of multiple identical phosphorylatable subunits.* J Biol Chem, 1984. **259**(3): p. 1834-41.

21.   Verardi, R., et al., *Structural topology of phospholamban pentamer in lipid bilayers by a hybrid solution and solid-state NMR method.* Proc Natl Acad Sci U S A, 2011. **108**(22): p. 9101-6.

22.   Simmerman, H.K.B., et al., *A Leucine Zipper Stabilizes the Pentameric Membrane Domain of Phospholamban and Forms a Coiled-coil Pore Structure.* J. Biol. Chem., 1996. **271**(10): p. 5941-5946.

23.   Ha, K.N., et al., *Lethal Arg9Cys phospholamban mutation hinders Ca2+-ATPase regulation and phosphorylation by protein kinase A.* Proc Natl Acad Sci U S A, 2011. **108**(7): p. 2735-40.

24.   Cornea, R.L., et al., *Reexamination of the role of the leucine/isoleucine zipper residues of phospholamban in inhibition of the Ca2+ pump of cardiac sarcoplasmic reticulum.* J Biol Chem, 2000. **275**(52): p. 41487-94.

25.   Kimura, Y., et al., *Phospholamban inhibitory function is activated by depolymerization.* J Biol Chem, 1997. **272**(24): p. 15061-4.

26.   Stokes, D.L., et al., *Interactions between Ca2+-ATPase and the pentameric form of phospholamban in two-dimensional co-crystals.* Biophys J, 2006. **90**(11): p. 4213-23.

27.   Mascioni, A., et al., *Structure and orientation of sarcolipin in lipid environments.* Biochemistry, 2002. **41**(2): p. 475-82.

28.   Kirby, T.L., C.B. Karim, and D.D. Thomas, *Electron paramagnetic resonance reveals a large-scale conformational change in the cytoplasmic domain of phospholamban upon binding to the sarcoplasmic reticulum Ca-ATPase.* Biochemistry, 2004. **43**(19): p. 5842-52.

29.   Karim, C.B., et al., *Phospholamban structural dynamics in lipid bilayers probed by a spin label rigidly coupled to the peptide backbone.* Proc Natl Acad Sci U S A, 2004. **101**(40): p. 14437-42.

30.   Gustavsson, M., et al., *Lipid-mediated folding/unfolding of phospholamban as a regulatory mechanism for the sarcoplasmic reticulum Ca2+-ATPase.* J Mol Biol, 2011. **408**(4): p. 755-65.

31.   Gustavsson, M., N.J. Traaseth, and G. Veglia, *Probing ground and excited states of phospholamban in model and native lipid membranes by magic angle spinning NMR spectroscopy.* Biochim Biophys Acta, 2012. **1818**(2): p. 146-53.

32.   Karim, C.B., et al., *Phosphorylation-dependent conformational switch in spin-labeled phospholamban bound to SERCA.* J Mol Biol, 2006. **358**(4): p. 1032-40.

33.   Ha, K.N., et al., *Controlling the inhibition of the sarcoplasmic Ca2+-ATPase by tuning phospholamban structural dynamics.* J Biol Chem, 2007. **282**(51): p. 37205-14.

34.   Toyoshima, C., et al., *Modeling of the inhibitory interaction of phospholamban with the Ca2+ ATPase.* Proc Natl Acad Sci U S A, 2003. **100**(2): p. 467-72.

35.   Chen, Z., B.L. Akin, and L.R. Jones, *Mechanism of reversal of phospholamban inhibition of the cardiac Ca2+-ATPase by protein kinase A and by anti-phospholamban monoclonal antibody 2D12.* J Biol Chem, 2007. **282**(29): p. 20968-76.

36.   Mueller, B., et al., *Direct detection of phospholamban and sarcoplasmic reticulum Ca-ATPase interaction in membranes using fluorescence resonance energy transfer.* Biochemistry, 2004. **43**(27): p. 8754-65.

37.   Negash, S., et al., *Phospholamban remains associated with the Ca2+- and Mg2+-dependent ATPase following phosphorylation by cAMP-dependent protein kinase.* Biochem J, 2000. **351**(Pt 1): p. 195-205.

38.   Li, J., D.J. Bigelow, and T.C. Squier, *Conformational changes within the cytosolic portion of phospholamban upon release of Ca-ATPase inhibition.* Biochemistry, 2004. **43**(13): p. 3870-9.

39.   Chen, L.T., et al., *Phospholamban modulates the functional coupling between nucleotide domains in Ca-ATPase oligomeric complexes in cardiac sarcoplasmic reticulum.* Biochemistry, 2009. **48**(11): p. 2411-21.

40.   Fanucci, G.E. and D.S. Cafiso, *Recent advances and applications of site-directed spin labeling.* Curr Opin Struct Biol, 2006. **16**(5): p. 644-53.

41.   Altenbach, C., et al., *Structural studies on transmembrane proteins. 2. Spin labeling of bacteriorhodopsin mutants at unique cysteines.* Biochemistry, 1989. **28**(19): p. 7806-12.

42.   Toniolo, C., et al., *Synthesis and conformational studies of peptides containing TOAC, a spin-labelled C alpha, alpha-disubstituted glycine.* J Pept Sci, 1995. **1**(1): p. 45-57.

43.   Carrington, A. and A.D. McLachlan, *Introduction to magnetic resonance : with applications to chemistry and chemical physics*. A Science paperback. 1979, London
New York: Chapman and Hall ;
Wiley. xix, 266 p.

44.   Poole, C.P., *Electron spin resonance : a comprehensive treatise on experimental techniques*. 2nd ed. 1983, New York: Wiley. xxvii, 780 p.

45.   Squier, T.C. and D.D. Thomas, *Methodology for increased precision in saturation transfer electron paramagnetic resonance studies of rotational dynamics.* Biophys J, 1986. **49**(4): p. 921-35.

46.   Altenbach, C., et al., *A collision gradient method to determine the immersion depth of nitroxides in lipid bilayers: application to spin-labeled mutants of bacteriorhodopsin.* Proc Natl Acad Sci U S A, 1994. **91**(5): p. 1667-71.

47.   Oh, K.J., et al., *Site-directed spin labeling of proteins. Applications to diphtheria toxin.* Methods Mol Biol, 2000. **145**: p. 147-69.

48. Bigelow, D.J. and G. Inesi, *Frequency-domain fluorescence spectroscopy resolves the location of maleimide-directed spectroscopic probes within the tertiary structure of the Ca-ATPase of sarcoplasmic reticulum.* Biochemistry, 1991. **30**(8): p. 2113-25.

49. MacLennan, D.H. and E.G. Kranias, *Phospholamban: a crucial regulator of cardiac contractility.* Nat Rev Mol Cell Biol, 2003. **4**(7): p. 566-77.

50. Zamoon, J., et al., *NMR solution structure and topological orientation of monomeric phospholamban in dodecylphosphocholine micelles.* Biophys J, 2003. **85**(4): p. 2589-98.

51. Cantilina, T., et al., *Comparative studies of cardiac and skeletal sarcoplasmic reticulum ATPases. Effect of a phospholamban antibody on enzyme activation by Ca2+.* J Biol Chem, 1993. **268**(23): p. 17018-25.

52. Tada, M. and M. Kadoma, *Regulation of the Ca2+ pump ATPase by cAMP-dependent phosphorylation of phospholamban.* Bioessays, 1989. **10**(5): p. 157-63.

53. MacLennan, D.H., Y. Kimura, and T. Toyofuku, *Sites of regulatory interaction between calcium ATPases and phospholamban.* Ann N Y Acad Sci, 1998. **853**: p. 31-42.

54. Hasenfuss, G. and B. Pieske, *Calcium cycling in congestive heart failure.* J Mol Cell Cardiol, 2002. **34**(8): p. 951-69.

55. Lipskaia, L., et al., *Sarcoplasmic reticulum Ca(2+) ATPase as a therapeutic target for heart failure.* Expert Opin Biol Ther, 2010. **10**(1): p. 29-41.

56. Cornea, R.L., S.J. Gruber, E.L. Lockamy, J.M. Muretta, D. Jin, J. Chen, R. Dahl, T. Bartfai, K.M. Zsebo, G.D. Gillespie, and D.D. Thomas, *High-throughput FRET assay yields allosteric SERCA activators.* J Biomol Screen, 2012. **Accepted July 8, 2012**.

57. Kaye, D.M., et al., *Percutaneous cardiac recirculation-mediated gene transfer of an inhibitory phospholamban peptide reverses advanced heart failure in large animals.* J Am Coll Cardiol, 2007. **50**(3): p. 253-60.

58. Lockamy, E.L., et al., *Functional and physical competition between phospholamban and its mutants provides insight into the molecular mechanism of gene therapy for heart failure.* Biochem Biophys Res Commun, 2011. **408**(3): p. 388-92.

59. Gruber, S.J., S. Haydon, and D.D. Thomas, *Phospholamban mutants compete with wild type for SERCA binding in living cells.* Biochem Biophys Res Commun, 2012: p. epublished.

60. Li, J., et al., *Structural and Functional Dynamics of an Integral Membrane Protein Complex Modulated by Lipid Headgroup Charge.* J Mol Biol, 2012.

61. Cornea, R.L., et al., *Mutation and phosphorylation change the oligomeric structure of phospholamban in lipid bilayers.* Biochemistry, 1997. **36**(10): p. 2960-7.

62. MacLennan, D.H., T. Toyofuku, and Y. Kimura, *Sites of regulatory interaction between calcium ATPases and phospholamban.* Basic Res Cardiol, 1997. **92 Suppl 1**: p. 11-5.

63. Mersol, J.V., et al., *Self-association accompanies inhibition of Ca-ATPase by thapsigargin.* Biophys J, 1995. **68**(1): p. 208-15.

64. Mahaney, J.E., et al., *Intermolecular interactions in the mechanism of skeletal muscle sarcoplasmic reticulum Ca(2+)-ATPase (SERCA1): evidence for a triprotomer.* Biochemistry, 2008. **47**(51): p. 13711-25.

65. Hidalgo, C., D.D. Thomas, and N. Ikemoto, *Effect of the lipid environment on protein motion and enzymatic activity of sarcoplasmic reticulum calcium ATPase.* J Biol Chem, 1978. **253**(19): p. 6879-87.

66. Squier, T.C. and D.D. Thomas, *Relationship between protein rotational dynamics and phosphoenzyme decomposition in the sarcoplasmic reticulum Ca-ATPase.* J Biol Chem, 1988. **263**(19): p. 9171-7.

67. Thomas, D.D., and C. Hidalgo, *Rotational motion of the sarcoplasmic reticulum Ca2+-ATPase.* Proc Natl Acad Sci U S A, 1978. **75**: p. 5488-5492.

68. Birmachu, W. and D.D. Thomas, *Rotational dynamics of the Ca-ATPase in sarcoplasmic reticulum studied by time-resolved phosphorescence anisotropy.* Biochemistry, 1990. **29**(16): p. 3904-14.

69. Horvath, L.I., et al., *Saturation transfer electron spin resonance of Ca2(+)-ATPase covalently spin-labeled with beta-substituted vinyl ketone- and maleimide-nitroxide derivatives. Effects of segmental motion and labeling levels.* Biophys J, 1990. **58**(1): p. 231-41.

70. Thomas, D.D., et al., *Rotational dynamics of protein and boundary lipid in sarcoplasmic reticulum membrane.* Biophys J, 1982. **37**(1): p. 217-25.

71. Napier, R.M., J.M. East, and A.G. Lee, *State of aggregation of the (Ca2+ + Mg2+)-ATPase studied using saturation-transfer electron spin resonance.* Biochim Biophys Acta, 1987. **903**(2): p. 365-73.

72. Saffman, P.G. and M. Delbruck, *Brownian motion in biological membranes.* Proc Natl Acad Sci U S A, 1975. **72**(8): p. 3111-3.

73. Voss, J., L.R. Jones, and D.D. Thomas, *The physical mechanism of calcium pump regulation in the heart.* Biophys J, 1994. **67**(1): p. 190-6.

74. Mascioni, A., et al., *Solid-state NMR and rigid body molecular dynamics to determine domain orientations of monomeric phospholamban.* J Am Chem Soc, 2002. **124**(32): p. 9392-3.

75. Thomas, D.D., L.R. Dalton, and J.S. Hyde, *Rotational diffusion studied by passage saturation transfer electron paramagnetic resonance.* J Chem Phys, 1976. **65**: p. 3006-3024.

76. Thomas, D.D., *Rotational Diffusion of Membrane Proteins*, in *Techniques for the Analysis of Membrane Proteins*, R.J.C. C.I. Ragan, Editor. 1986, Chapman and Hall: London.

77. Karim, C.B., et al., *Synthetic null-cysteine phospholamban analogue and the corresponding transmembrane domain inhibit the Ca-ATPase.* Biochemistry, 2000. **39**(35): p. 10892-7.

78. Karim, C.B., Z. Zhang, and D.D. Thomas, *Synthesis of TOAC spin-labeled proteins and reconstitution in lipid membranes.* Nat Protoc, 2007. **2**(1): p. 42-9.

79. Eletr, S. and G. Inesi, *Phospholipid orientation in sarcoplasmic membranes: spin-label ESR and proton NMR studies.* Biochim Biophys Acta, 1972. **282**(1): p. 174-9.

80.   Coll, R.J. and A.J. Murphy, *Purification of the CaATPase of sarcoplasmic reticulum by affinity chromatography.* J Biol Chem, 1984. **259**(22): p. 14249-54.

81.   Reddy, L.G., et al., *Defining the molecular components of calcium transport regulation in a reconstituted membrane system.* Biochemistry, 2003. **42**(15): p. 4585-92.

82.   Levy, D., et al., *Reconstitution of the sarcoplasmic reticulum Ca(2+)-ATPase: mechanisms of membrane protein insertion into liposomes during reconstitution procedures involving the use of detergents.* Biochim Biophys Acta, 1992. **1107**(2): p. 283-98.

83.   Thomas, D.D. and C. Hidalgo, *Rotational motion of the sarcoplasmic reticulum Ca2+-ATPase.* Proc Natl Acad Sci U S A, 1978. **75**(11): p. 5488-92.

84.   Baroin, A., A. Bienvenue, and P.F. Devaux, *Spin-label studies of protein-protein interactions in retinal rod outer segment membranes. Saturation transfer electron paramagnetic resonance spectroscopy.* Biochemistry, 1979. **18**(7): p. 1151-5.

85.   Karim, C.B., et al., *Role of cysteine residues in structural stability and function of a transmembrane helix bundle.* J Biol Chem, 2001. **276**(42): p. 38814-9.

86.   Ablorh, N.A., et al., *Accurate quantitation of phospholamban phosphorylation by immunoblot.* Anal Biochem, 2012.

87.   Goldman, S.A., Bruno, G.V., and Freed, J.H., *Estimating Slow-Motional Rotational Correlation Times for Nitroxides by Electron Spin Resonance.* J Phys Chem, 1972. **76**(13): p. 1858-1860.

88.   Mason, R.P. and J.H. Freed, *Estimating Microsecond Rotational Correlation Times from Lifetime Broadening of Nitroxide Electron Spin Resonance Spectra Near the Rigid Limit.* J Phys Chem, 1974. **78**(13): p. 1321-1323.

89.   Scarpelli, F., et al., *Aggregation of transmembrane peptides studied by spin-label EPR.* J Phys Chem B, 2009. **113**(36): p. 12257-64.

90.   Uhrikova, D., et al., *Small-angle neutron scattering study of the n-decane effect on the bilayer thickness in extruded unilamellar dioleoylphosphatidylcholine liposomes.* Biophys Chem, 2000. **88**(1-3): p. 165-70.

91.   Cherry, R.J. and R.E. Godfrey, *Anisotropic rotation of bacteriorhodopsin in lipid membranes. Comparison of theory with experiment.* Biophys J, 1981. **36**(1): p. 257-76.

92.   Howard, E.C., et al., *Simulation of saturation transfer electron paramagnetic resonance spectra for rotational motion with restricted angular amplitude.* Biophys J, 1993. **64**(3): p. 581-93.

93.   Beth, A.H. and E.J. Hustedt, *Saturation Transfer EPR: Rotational Dynamics of Membrane Proteins.* Biomedical EPR-Part B: Methodology, Instrumentation, and Dynamics, ed. S.S. Eaton, G.R. Eaton, and L.J. Berliner. 2005, New York: Springer. 369-408.

94.   Marsh, D., et al., *TOAC spin labels in the backbone of alamethicin: EPR studies in lipid membranes.* Biophys J, 2007. **92**(2): p. 473-81.

95.   Marsh, D., *Saturation transfer EPR studies of slow rotational motion in membranes.* Appl Magn Reson, 2007. **31**: p. 387 - 410.

96.   Hustedt, E.J. and A.H. Beth, *The sensitivity of saturation transfer electron paramagnetic resonance spectra to restricted amplitude uniaxial rotational diffusion.* Biophys J, 2001. **81**(6): p. 3156-65.

97.   Fujii, J., et al., *Expression and site-specific mutagenesis of phospholamban. Studies of residues involved in phosphorylation and pentamer formation.* J Biol Chem, 1989. **264**(22): p. 12950-5.

98.   Hughes, E., J.C. Clayton, and D.A. Middleton, *Probing the oligomeric state of phospholamban variants in phospholipid bilayers from solid-state NMR measurements of rotational diffusion rates.* Biochemistry, 2005. **44**(10): p. 4055-66.

99.   Reddy, L.G., L.R. Jones, and D.D. Thomas, *Depolymerization of phospholamban in the presence of calcium pump: a fluorescence energy transfer study.* Biochemistry, 1999. **38**(13): p. 3954-62.

100.   Yao, Q., et al., *Oligomeric interactions between phospholamban molecules regulate Ca-ATPase activity in functionally reconstituted membranes.* Biochemistry, 2001. **40**(21): p. 6406-13.

101.   Mahaney, J.E., J.P. Froehlich, and D.D. Thomas, *Conformational transitions of the sarcoplasmic reticulum Ca-ATPase studied by time-resolved EPR and quenched-flow kinetics.* Biochemistry, 1995. **34**(14): p. 4864-79.

102.   Mahaney, J.E., et al., *Phospholamban inhibits Ca2+ pump oligomerization and intersubunit free energy exchange leading to activation of cardiac muscle SERCA2a.* Ann N Y Acad Sci, 2003. **986**: p. 338-40.

103.   Froehlich, J.P., et al., *Complex kinetic behavior in the Na,K- and Ca-ATPases. Evidence for subunit-subunit interactions and energy conservation during catalysis.* Ann N Y Acad Sci, 1997. **834**: p. 280-96.

104.   Squier, T.C., S.E. Hughes, and D.D. Thomas, *Rotational dynamics and protein-protein interactions in the Ca-ATPase mechanism.* J Biol Chem, 1988. **263**(19): p. 9162-70.

105.   Voss, J., et al., *Effects of melittin on molecular dynamics and Ca-ATPase activity in sarcoplasmic reticulum membranes: time-resolved optical anisotropy.* Biochemistry, 1991. **30**(30): p. 7498-506.

106.   Mahaney, J.E., et al., *Effects of melittin on lipid-protein interactions in sarcoplasmic reticulum membranes.* Biophys J, 1992. **63**(6): p. 1513-22.

107.   Karon, B.S., et al., *Anesthetics alter the physical and functional properties of the Ca-ATPase in cardiac sarcoplasmic reticulum.* Biophys J, 1995. **68**(3): p. 936-45.

108.   Cornea, R.L. and D.D. Thomas, *Effects of membrane thickness on the molecular dynamics and enzymatic activity of reconstituted Ca-ATPase.* Biochemistry, 1994. **33**(10): p. 2912-20.

109.   Karon, B.S., J.E. Mahaney, and D.D. Thomas, *Halothane and cyclopiazonic acid modulate Ca-ATPase oligomeric state and function in sarcoplasmic reticulum.* Biochemistry, 1994. **33**(46): p. 13928-37.

110.   Birmachu, W., et al., *Protein and lipid rotational dynamics in cardiac and skeletal sarcoplasmic reticulum detected by EPR and phosphorescence anisotropy.* Biochemistry, 1993. **32**(36): p. 9445-53.

111. Robia, S.L., et al., *Forster transfer recovery reveals that phospholamban exchanges slowly from pentamers but rapidly from the SERCA regulatory complex.* Circ Res, 2007. **101**(11): p. 1123-9.

112. Fujii, J., et al., *Co-expression of slow-twitch/cardiac muscle Ca2(+)-ATPase (SERCA2) and phospholamban.* FEBS Lett, 1990. **273**(1-2): p. 232-4.

113. Toyofuku, T., et al., *Identification of regions in the Ca(2+)-ATPase of sarcoplasmic reticulum that affect functional association with phospholamban.* J Biol Chem, 1993. **268**(4): p. 2809-15.

114. Sachs, J.N. and D.M. Engelman, *Introduction to the membrane protein reviews: the interplay of structure, dynamics, and environment in membrane protein function.* Annu Rev Biochem, 2006. **75**: p. 707-12.

115. McLaughlin, S. and D. Murray, *Plasma membrane phosphoinositide organization by protein electrostatics.* Nature, 2005. **438**(7068): p. 605-11.

116. Tada, M. and M. Inui, *Regulation of calcium transport by the ATPase-phospholamban system.* J Mol Cell Cardiol, 1983. **15**(9): p. 565-75.

117. MacLennan, D.H., and Kranias, E. G., *Phospholamban: a crucial regulator of cardiac contractility.* Nature Reviews, 2003. **4**: p. 666-678.

118. Metcalfe, E.E., N.J. Traaseth, and G. Veglia, *Serine 16 phosphorylation induces an order-to-disorder transition in monomeric phospholamban.* Biochemistry, 2005. **44**(11): p. 4386-96.

119. Asahi, M., et al., *Physical interactions between phospholamban and sarco(endo)plasmic reticulum Ca2+-ATPases are dissociated by elevated Ca2+, but not by phospholamban phosphorylation, vanadate, or thapsigargin, and are enhanced by ATP.* J Biol Chem, 2000. **275**(20): p. 15034-8.

120. Zamoon, J., et al., *Mapping the interaction surface of a membrane protein: Unveiling the conformational switch of phospholamban in calcium pump regulation.* Proc Natl Acad Sci U S A, 2005. **102**(13): p. 4747-52.

121. Nesmelov, Y.E., et al., *Rotational dynamics of phospholamban determined by multifrequency electron paramagnetic resonance.* Biophys J, 2007. **93**(8): p. 2805-12.

122. Kast, D., et al., *Phosphorylation-induced structural changes in smooth muscle myosin regulatory light chain.* Proc Natl Acad Sci U S A, 2010. **107**(18): p. 8207-12.

123. Hunter, G.W., S. Negash, and T.C. Squier, *Phosphatidylethanolamine modulates Ca-ATPase function and dynamics.* Biochemistry, 1999. **38**(4): p. 1356-64.

124. Birmachu, W., F.L. Nisswandt, and D.D. Thomas, *Conformational transitions in the calcium adenosinetriphosphatase studied by time-resolved fluorescence resonance energy transfer.* Biochemistry, 1989. **28**(9): p. 3940-7.

125. Muretta, J.M., et al., *High -performance time-resolved fluorescence by direct waveform recording.* Rev Sci Instrum, 2010. **81**: p. 103101-1 - 103101-8.

126. Agafonov, R.V., et al., *Structural dynamics of the myosin relay helix by time-resolved EPR and FRET.* Proc Natl Acad Sci U S A, 2009.

127. Lakowicz, J.R., *Principles of Fluorescence Spectroscopy.* Second ed. 1999, New York: Kluwer Academic/Plenum Press.

128. Bick, R.J., et al., *Membrane asymmetry in isolated canine cardiac sarcoplasmic reticulum: comparison with skeletal muscle sarcoplasmic reticulum.* J Membr Biol, 1998. **164**(2): p. 169-75.

129. Sonntag, Y., et al., *Mutual adaptation of a membrane protein and its lipid bilayer during conformational changes.* Nat Commun, 2011. **2**: p. 304.

130. Hughes, E., J.C. Clayton, and D.A. Middleton, *Cytoplasmic residues of phospholamban interact with membrane surfaces in the presence of SERCA: a new role for phospholipids in the regulation of cardiac calcium cycling?* Biochim Biophys Acta, 2009. **1788**(2): p. 559-66.

131. Lee, A.G., *Lipid-protein interactions in biological membranes: a structural perspective.* Biochim Biophys Acta, 2003. **1612**(1): p. 1-40.

132. Gustavsson, M., N.J. Traaseth, and G. Veglia, *Activating and deactivating roles of lipid bilayers on the Ca(2+)-ATPase/phospholamban complex.* Biochemistry, 2011. **50**(47): p. 10367-74.

133. Guo, X. and L. Huang, *Recent advances in nonviral vectors for gene delivery.* Acc Chem Res, 2012. **45**(7): p. 971-9.

134. Kunze, A., S. Svedhem, and B. Kasemo, *Lipid transfer between charged supported lipid bilayers and oppositely charged vesicles.* Langmuir, 2009. **25**(9): p. 5146-58.

135. Reddy, L.G., et al., *Co-reconstitution of phospholamban mutants with the Ca-ATPase reveals dependence of inhibitory function on phospholamban structure.* J Biol Chem, 1999. **274**(12): p. 7649-55.

136. Muretta, J.M., et al., *High-performance time-resolved fluorescence by direct waveform recording.* Rev Sci Instrum, 2010. **81**(10): p. 103101.

137. Foerster, T., *Zwischenmolekulare energiewanderung und fluoreszenz.* Ann. Physik., 1948. **437**: p. 55-75.

138. Agafonov, R.V., et al., *Structural dynamics of the myosin relay helix by time-resolved EPR and FRET.* Proc Natl Acad Sci U S A, 2009. **106**(51): p. 21625-30.

139. Dong, J., G. Yang, and H.S. McHaourab, *Structural basis of energy transduction in the transport cycle of MsbA.* Science, 2005. **308**(5724): p. 1023-8.

140. Perozo, E., et al., *Open channel structure of MscL and the gating mechanism of mechanosensitive channels.* Nature, 2002. **418**(6901): p. 942-8.

141. Buck, B., et al., *Overexpression, purification, and characterization of recombinant Ca-ATPase regulators for high-resolution solution and solid-state NMR studies.* Protein Expr Purif, 2003. **30**(2): p. 253-61.

142. Douglas, J.L., et al., *Rapid, high-yield expression and purification of Ca2+-ATPase regulatory proteins for high-resolution structural studies.* Protein Expr Purif, 2005. **40**(1): p. 118-25.

143. Veglia, G., et al., *What can we learn from a small regulatory membrane protein?* Methods Mol Biol, 2010. **654**: p. 303-19.

144. Kroncke, B.M., P.S. Horanyi, and L. Columbus, *Structural origins of nitroxide side chain dynamics on membrane protein alpha-helical sites.* Biochemistry, 2010. **49**(47): p. 10045-60.

145. Ha, K.N., M. Gustavsson, and G. Veglia, *Tuning the structural coupling between the transmembrane and cytoplasmic domains of phospholamban to control*

sarcoplasmic reticulum Ca(2+)-ATPase (SERCA) function. J Muscle Res Cell Motil, 2012. **33**(6): p. 485-92.

Appendix A – Brief Introduction to Fluorescence Resonance Energy Transfer Spectroscopy

Fluorescence is a fast (10^{-8} s) process that occurs when a molecule emits a photon while transitioning from an excited singlet state (e.g., S_1) to its ground singlet state (S_0) [127]. For most fluorescent molecules (fluorophores), the energy difference between S_0 and S_1 is large enough so that only S_0 is significantly populated by ambient thermal energy, but fluorophores can be promoted to S_1 (or even higher singlet states) by absorbing photons. Absorption can excite ground-state fluorophores to many vibrational levels within S_1, yielding a distribution of excitation energies (the excitation spectrum). After absorption, excited fluorophores undergo rapid ($\sim 10^{-12}$ s) vibrational relaxation to the lowest-energy S_1 level prior to fluorescence. Vibrational relaxation consumes energy, and consequently
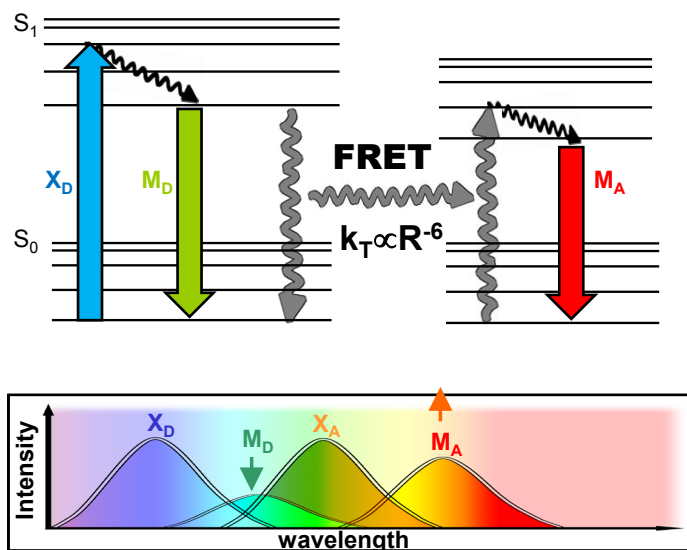

Fig. 47. Jablonski diagram depicting fluorescence and FRET. Excitation of a fluorophore by photon absorption (XD) promotes it from the singlet ground state (S_0) to the first singlet excited state (S_1). After vibrational relaxation to the lowest S_1 vibrational level, the fluorophore can relax by releasing a photon (fluorescence, M_D), or can donate its energy non-radiatively to a nearby acceptor fluorophore (R^{-6} dependence) with an excitation spectrum (X_A) that overlaps the donor emission spectrum (M_D). The excited acceptor also vibrationally relaxes and then fluoresces (M_A). Adapted from David D. Thomas spectroscopy lectures.

fluoresced photons are of lower energy than those used to excite the fluorophore (i.e., the emitted photons are 'red-shifted'). Relaxation may bring the excited fluorophore to many different S_0 vibrational levels, yielding a distribution of emitted photon energies (the emission spectrum) that often mirrors the excitation spectrum (Fig. 47).

Besides radiative (i.e., photon emission) processes, fluorophores may also relax through non-radiative pathways, including collisional quenching and internal conversion of the excited-state energy to thermal energy. One particularly useful relaxation process is fluorescence resonance energy transfer (FRET), where an excited 'donor' fluorophore transfers its energy *non-radiatively* to an acceptor fluorophore. The energy transfer efficiency (E) of FRET is given by Eq. 16:

$$E = \frac{R_0{}^6}{R_0{}^6 + R^6}$$
Eq. 16

Where R represents the distance between the donor and acceptor fluorophores and R_0 is the Förster distance of that particular donor-acceptor pair (i.e., the inter-probe distance where FRET efficiency is 50%). The Förster distance, in turn, is given by Eq. 17:

$$R_0 = 9790(J\kappa^2\eta^{-4}\phi_D)^{1/6}$$
Eq. 17

where J is the integrated overlap of the donor emission and acceptor excitation spectra, κ^2 is an orientation factor (assumed to be 2/3 for randomly-oriented samples), η is the refractive index of the medium (usually ~1.4), and ϕ_D is the quantum yield of the donor.

Clearly, FRET efficiency is strongly distance-dependent (Eq. 16, R^{-6} dependence) and thus can be used to make nanometer-scale measurements by quantifying the extent of FRET between donor and acceptor fluorophores. Conventional 'steady-state' FRET measures the decrease of the donor emission intensity in the presence an acceptor,

relative to the donor-only emission intensity, to determine the donor-acceptor distance. While straightforward, steady-state FRET measurements suffer from limited resolution as they can detect a *net* change in emission intensity, and thus can only report the mean distance between the donor and acceptor fluorophores. For proteins in equilibrium between multiple conformations, each with their own inter-probe distance distribution, conventional FRET will only detect their average. Time-resolved FRET (TR-FRET) offers substantially better resolution by measuring the fluorescence decay after an excitation pulse and extracting lifetimes corresponding to the various donor-acceptor distances in the sample.